ADVANCED MULTIMODAL IMAGING IN EPILEPTOGENIC MALFORMATIONS OF CORTICAL DEVELOPMENT

Suk-Jun Hong
Department of Neurology and Neurosurgery
McGill University, Montreal, Canada

May 2016

A thesis submitted to McGill University
in partial fulfillment of the requirement of the degree of Doctor of Philosophy

To
Jieun, Celine, and my parents and family

ACKNOWLEDGEMENT

Above all, I would like to express enormous gratitude to the patients and control subjects who were willing to participate in this research, showing a great patience for sometimes lengthy and multiple MRI scanning sessions. Without their valuable contributions, research experiments that will be introduced in this thesis would have not been able to even be initiated. I hope that scientific endeavors taken to yield a series of following studies are not limited as results of one PhD thesis but rather will become an important basis for more advanced and promising clinical researches that could truly help to treat neurodevelopmental diseases and thus relieve the suffering of patients.

Second but equally grateful contributors of this thesis are my supervisors, Dr. Andrea Bernasconi and Neda Bernasconi, an excellent researcher couple who have spared no pains to guide me who was just a little, naïve student having only excessive zeal. They have strived to teach me, although still incomplete, everything needed to become an independent junior researcher such as a writing skill, critical thinking, and how to conduct meaningful research design. For every moment I have been with them, it was a joyful and sincere experience that I could learn the essence how to make a 'real' scientific research.

Although we both met as students at the initial moment, Dr. Boris Bernhardt has been always as a great mentor of mine along my whole PhD period and therefore should receive my another big gratitude for his significant contributions. It was my great luck to have been able to co-work with him. I learned from him a plenty of timely and invaluable tips related to make an actual publication, writing skills and also a model how to develop my career as an young investigator.

I also appreciate to Dr. Hosung Kim, who provided me a great care initially when I started my degree, which could otherwise have been much struggled in stabilizing myself for PhD research. The period in which we were together was a true moment that I could enjoy and also learn many important research and engineering knowledge, which built altogether the current my neuroimaging skills.

I would like to give many thanks to my colleagues and friends from the laboratory: Jessie Kulaga-Yoskovitz, Dewi Schrader, Pierre Besson, Min Liu, Benoit Caldairou, Anton Plavski, Ravnoor Gill, Seun Jeon, Britta Wandschneider, Sophie Adler, Sidney Krystal, Maged Goubran, Jiwook Hwang, Kevin Liang, Essie Bae and Denis Rivière. Among them, especially thanks to my lab mates, Jessie, Min and Benoit who have been with me for most of times, trying to listen all my grumbling and also helping the research both directly and indirectly. I appreciate to Sidney Krystal for helping me to translate the abstract of this thesis into French. I send my deep admiration to all the people who have developed the BIC and MNI into such a world-class brain research institute and provide a fantastic working place for neuroimaging study: Alan Evans, Bruce Pike, Sylvain Baillet, Louis Collins, Paul Gravel, Pierrick Coupe, Vladimir Fonov, Kevine Larcher, Jean-Francois Malouin, Sylvain Milot, Anna Stabile.

I greatly appreciate to my committee members Dr. Bruce Pike, and all examiners for my PhD candidacy exam and defence Dr. Edward Hogan, Dr. Sylvain Baillet, Dr. Jeffery Hall, Dr. Kenneth Hastings, Dr. Jamie Near for providing wise and generous advice to improve the quality of this work. Numerous thanks to Integrated Program in Neuroscience team Monique Lederman, Katherine Vanka, Tom Hein, Jessie Kulaga-Yoskovitz, and Vivian Omune.

I was lucky enough to be selected as a recipient for following awards and fellowships which made my research life much smoother and easier, and thus would like to express my deep appreciation: Jeanne Timmins Costello Studentship (MNI), Publication award for graduate student (Canadian League Against Epilepsy), Grass Young Investigator Award (American Epilepsy Society), Desjardins Outstanding Student Award (MNI) and Simon Groom Travel Award (MNI).

Finally, I send my baggiest thanks to my beloved family for their constant supports: Jieun, Celine, my parents Soonae Kim, Kihyung Hong, Yoonmi Park and Jongkyun Lee, my sister Sukyoung, Jeongeun. Among them, especially my wife Jieun had to come to Montreal only for supporting me, having left her family, and was nevertheless always a big inspiration whenever I encountered a tough PhD obstacle. My PhD degree would definitely have not been possible without her supports positive mind.

CONTRIBUTIONS OF AUTHORS

All presented manuscripts in this thesis are the result of a close collaboration between myself and my supervisors **Andrea Bernasconi, MD** and **Neda Bernasconi, MD PhD**. We jointly designed the experiments, conducted the image processing and statistical analysis, and wrote the manuscripts. The following list summarizes the contributions of the co-authors at the Montreal Neurological Institute, in alphabetical order.

1. **Boris Bernhardt, PhD**. Advised in study design, statistical analyses, and medical writing for Project 1-4
2. **Benoit Caldairou, PhD**. Assisted in the cross-validation of Project 3
3. **Marie C. Guiot, MD.** Provided histopathological diagnosis for Project 1-4
4. **Jeffery A. Hall, MD MSc.** Provided histopathological data for Project 1-4
5. **Hosung Kim, PhD**. Assisted in study design and image processing of Project 1-3.
6. **Liu Min, PhD.** Assisted in general writing for thesis.
7. **Dewi Schrader, MD**. Performed manual labeling of MCD lesions in Project 1-3

PUBLICATIONS

Peer-reviewed Articles

a. Published

1. **Hong SJ**, Bernhardt BC, Schrader D, Bernasconi N, and Bernasconi A. *Whole-brain MRI phenotyping in dysplasia-related frontal lobe epilepsy*. Neurology. 2016, 86(7):643-50.
2. **Hong SJ**, Bernhardt BC, Schrader D, Caldairou B, Bernasconi N, and Bernasconi A. *MRI-based lesion profiling of epileptogenic cortical malformations*. 18th International Conference on Medical Image Computing and Computer Assisted Interventions. 2015, *LNCS* 9350:501-510
3. **Hong SJ**, Kim H, Schrader D, Bernasconi N, Bernhardt BC, and Bernasconi A, *Automated detection of cortical dysplasia type II in MRI-negative epilepsy.* Neurology. 2014, 83(1): 48-55
4. **Hong SJ**, Liu M, Bernhardt BC and Bernasconi A. *Computational neuroanatomy of epilepsy.* In Imaging biomarkers in epilepsy, Cambridge University Press (Bernasconi A, Bernasconi N, Koepp M Eds), 2016 (in press)
5. Liu M, Bernhardt BC, **Hong SJ**, Caldairou B, Bernasconi A, Bernasconi N. *The superficial white matter in temporal lobe epilepsy: a key link between structural and functional*

network disruptions. Brain, 2016 (in press)

6. Bernhardt BC, Bernasconi A, Liu M, **Hong SJ**, Caldairou B; Goubran M, Marie G, Hall J, Bernasconi N. *The spectrum of structural and functional imaging abnormalities in temporal lobe epilepsy*. Annals of Neurology, 2016 (in press)
7. Bernhardt BC, **Hong SJ**, Bernasconi A, Bernasconi N. *MRI pattern learning in temporal lobe epilepsy: Classification and prognostics*. Annals of Neurology. 2015, 77(3):436-46.
8. Kulaga-Yoskovitz J, Bernhardt BC, **Hong SJ**, Mansi T, Liang K, Kouwe A, Smallwood J, Bernasconi A, Bernasconi B. *Multi-contrast and submillimetric 3-Tesla hippocampal subregional segmentation protocol and data repository.* Scientific data. 2015, 10; 2:150059
9. Bernhardt BC, Bernasconi N, **Hong SJ**, Dery S, *Bernasconi A. Subregional mesiotemporal network topology is altered in temporal lobe epilepsy.* Cerebral Cortex. 2015, 1-12
10. Kim HS, Caldairou B, Hwang JW, Mansi T, **Hong SJ**, Bernasconi N, Bernasconi A. *Accurate cortical tissue classification on MRI by modeling cortical folding patterns*. Human Brain Mapping. 2015, 36(9):3563-74.
11. Caciagli L, Bernhardt BC, **Hong SJ**, Bernasconi A, Bernasconi N. Functional network alterations and their structural substrate in drug-resistant epilepsy. Frontiers in Neuroscience. 2014, 8:411
12. Bernhardt BC, **Hong SJ**, Bernasconi A, Bernasconi N, *Imaging structural and functional brain networks in temporal lobe epilepsy.* Frontier in Human Neuroscience. 2013, 7:624
13. Voets NL, Beckmann CF, Cole DM, **Hong SJ**, Bernasconi A, Bernasconi N, *Structural substrates for resting network disruption in temporal lobe epilepsy.* Brain. 2012, 135:2350

b. Submitted and work in preparation

1. **Hong SJ**, Bernhardt BC, Caldairou B, Hall JA, Guiot MC, Schrader D, Bernasconi N and

Bernasconi A. *Multimodal MRI profiling of cortical dysplasia type-II.* (Minor revision).

2. **Hong SJ**, Bernhardt BC, Bernasconi N and Bernasconi A. *The spectrum of cortical malformations is associated to gradual structural-functional network alterations.*

Meeting presentation

1. **Hong SJ**, Bernhardt BC, Bernasconi N and Bernasconi A. *Topological spectrum of structural network alterations in malformations of cortical development*. The 22th Annual Meeting of the Organization for Human Brain Mapping 2016, Geneva, Switzerland
2. **Hong SJ**, Bernhardt BC, Schrader D, Bernasconi N and Bernasconi A. *Focal cortical dysplasia type-II: MRI-based profiling and subtype prediction.* The 69th Annual Meeting of the American Epilepsy Society 2015, Philadelphia, USA
3. **Hong SJ**, Bernhardt BC, Schrader D, Bernasconi N, and Bernasconi A. *Multicontrast MRI profiling of focal cortical dysplasia Type-II*. The 31th International epilepsy congress 2015, Istanbul, Turkey
4. **Hong SJ**, Kim H, Schrader D, Bernasconi N, Bernhardt BC and Bernasconi A. *Automated detection of cortical dysplasia type II in MRI-negative epilepsy*. The 68th Annual Meeting of the American Epilepsy Society 2014, Seattle, USA
5. **Hong SJ**, Bernhardt BC, Bernasconi N and Bernasconi A. *Topological alterations of structural networks in drug-resistant extra-temporal lobe epilepsy*. The 20th Annual Meeting of the Organization for Human Brain Mapping 2014, Hamburg, Germany
6. **Hong SJ**, Bernasconi N and Bernasconi A. *Diffuse cortical atrophy in MRI-negative extra-temporal epilepsy.* The 30th International epilepsy congress 2013, Montreal, Canada
7. **Hong SJ**, Bernhardt BC, Kim H, Bernasconi N and Bernasconi A. *Patterns of large-scale*

brain networks organization in lesional and MRI-negative epilepsy. The 30th International epilepsy congress 2013, Montreal, Canada

8. **Hong SJ**, Kim H, Schrader D, Bernasconi N and Bernasconi A. *Cryptogenic (MRI-negative) epilepsy: automated seizure focus lateralization.* The 66th Annual Meeting of the American Epilepsy Society 2012, San Diego, USA
9. Schrader D, **Hong SJ** and Bernasconi A. *Cortical complexity is increased in patients with cryptogenic epilepsy.* The 66th Annual Meeting of the American Epilepsy Society 2012, San Diego, USA
10. **Hong SJ**, Bernhardt BC, Schrader D, Kim H, Bernasconi N and Bernasconi A. *MRI-based cortical thickness Analysis in drug-resistant extra-temporal focal epilepsy.* The 18th Annual Meeting of the Organization for Human Brain Mapping 2012, Beijing, China.
11. **Hong SJ**, Bernhardt BC, Kim H, Bernasconi N, Bernasconi A. *MRI-based cortical thickness Analysis in drug-resistant cryptogenic epilepsy.* The 17th Annual Meeting of the Organization for Human Brain Mapping 2011, Quebec City, Canada.
12. Bernhardt BC, **Hong SJ**, Chen Z, He Y, Evans AC, Bernasconi A, Bernasconi A. *Disrupted large-scale network organization in temporal lobe epilepsy: insights from graph-theoretical analysis of inter-regional cortical thickness correlations.* The 17th Annual Meeting of the Organization for Human Brain Mapping 2011, Quebec City, Canada.
13. Bernhardt BC, **Hong SJ**, Kim H, Bernasconi A, Bernasconi N. *Diffusion abnormalities of fiber tracts underlying cortical regions in temporal lobe epilepsy.* The 17th Annual Meeting of the Organization for Human Brain Mapping 2011, Quebec City, Canada.
14. Bernhardt BC, **Hong SJ**, Kim H, Bernasconi N, Bernasconi A. *MRI-based cortical thickness analysis in drug-resistant cryptogenic epilepsy.* The 17th Annual Meeting of the Organization for Human Brain Mapping 2011, Quebec City, Canada.

15. Riviere D, Bernhardt BC, Kim H, **Hong SJ**, Perrot M, Mangin JF, Regis J, Bernasconi N, Bernasconi A. *Diffuse sulcal anomalies associated with focal epileptogenic malformations of cortical development.* The 17th Annual Meeting of the Organization for Human Brain Mapping 2011, Quebec City, Canada.
16. Bernhardt BC, Kim H, **Hong SJ**, Dery S, Bernasconi A, Bernasconi N. *Subregional mesiotemporal network regularization and fragmentation in temporal lobe epilepsy.* Organization Human Brain Mapping (OHBM), Proceedings of the 20th Annual Meeting, Hamburg, Germany, 2014
17. Bernhardt BC, Kulaga-Yoskovitz J, Caldairou B**, Hong SJ**, Liu M, Bernasconi N, Bernasconi A. *MRI phenotyping of hippocampal subfield pathology in temporal lobe epilepsy.* Organization Human Brain Mapping (OHBM), Proceedings of the 21th Annual Meeting, Honolulu, Hawaii (USA) 2015
18. Liu M, Bernhardt BC, **Hong SJ**, Caldairou B, Bernasconi N, Bernasconi A. *Multicontrast MRI analysis of grey and white matter in temporal lobe epilepsy.* Proceedings of the 21th Annual Meeting, Honolulu, Hawaii (USA) 2015
19. Liu M, Bernhardt BC, **Hong SJ**, Caldairou B, Bernasconi N, Bernasconi A. *Differential distribution of cortical thinning and subcortical white matter diffusion anomalies in temporal lobe epilepsy.* Proceedings of the 31st International Epilepsy Congress, Istanbul, Turkey, 2015. Epilepsia 2015
20. Bernhardt BC, Kulaga-Yoskovitz J, Caldairou B, **Hong SJ**, Liu M, Bernasconi N, Bernasconi A. *MRI-based hippocampal subfield analysis accurately predicts post-surgical outcome.* Proceedings of the 31st International Epilepsy Congress, Turkey, 2015. Epilepsia

ABSTRACT

Background. Malformations of cortical development (MCD) are a group of congenital anomalies characterized by variable brain deformations and high epileptogenicity. Magnetic resonance imaging (MRI) has revolutionized the clinical management of this disorder because of its unmatched ability to visualize pathological substrates. Yet, the current sensitivity to identify the primary lesion has a limit in covering the full spectrum of MCD, especially those with mild anomalies, substantially challenging a reliable clinical diagnosis. Notably, sporadic histological and MRI studies have indicated that structural anomalies in the primary lesion may extend to remote cortical areas. While these findings, together with functional evidence of widespread epileptogenic networks, suggest distributed pathological substrates, the anatomical patterns and topological principles underlying MCD remain poorly understood.

Purpose. To develop advanced multimodal imaging and computational frameworks for the characterization and identification of MCD, and phenotype their whole-brain structure and network organization.

Methods. We carried out following projects: 1) Implementation of an automated machine-learning classifier relying on surface-based MRI features to detect subtle malformations; 2) Evaluation of whole-brain morphology using cortical thickness and folding complexity; 3) Development of a novel framework to characterize morphology, intensity, diffusion, and function of the primary lesion; 4) Statistical and graph-theoretical analysis of structural-functional brain network across the MCD spectrum. In projects 1-3, we targeted patients with focal cortical dysplasia (FCD), while project 4 included multiple representative MCD subtypes.

Results. In project 1, our classifier accurately identified subtle FCD initially overlooked on routine radiological assessment. The algorithm showed an excellent sensitivity (74%), while achieving a perfect specificity (100%; no false positive) in controls. The performance revealed generalizability

across different cohorts, scanners, and field strengths. In project 2, we demonstrated that anomalies extend beyond the primary lesion to remote cortical areas, showing distinctive patterns relative to pathological subtypes. Specifically, FCD Type-I (characterized only by cortical dyslamination on histology) displayed widespread cortical thinning, while Type-II (dyslamination together with dysmorphic neurons) was associated with bilateral cortical thickening. Cortical folding complexity also diverged, with increases in Type-I and decreases in Type-II. Distinctive MRI signatures were also demonstrated in project 3, where we were able to dissociate within-subtype entities, namely FCD Type-IIA (characterized by isolated dysmorphic neurons) and IIB (dyslamination together with balloon cells). Indeed, by using advanced intra- and subcortical lesion profiling, we found marked patterns of abnormal morphology, intensity, diffusivity and function in Type-IIB, compared to IIA which presented with only mild intensity and diffusion changes close to the grey-white matter interface. These group-level findings were validated in single patients by machine-learning, which predicted with >90% accuracy FCD histological subtypes *in vivo* based on MRI features. Finally, project 4 demonstrated large-scale network reorganization in MCD. The extent of anomalies followed a gradient relative to the putative timing of the underlying malformative process. Indeed, subtle changes were associated with FCD Type-II due to atypical neuronal proliferation occurring at the earliest stages of cortical development, intermediate effects were found in migration-related heterotopias, and markedly impacted cortical network architecture was seen in polymicrogyrias, malformations likely due to late-stage cortical disorganization.

Significance. The proposed computational models enable the detection of the most-subtle malformative lesion with unprecedented accuracy, paving the way to surgical treatment for patients in whom conventional means are non-diagnostic. Furthermore, our studies unveiling whole-brain and large-scale organizational properties provide novel insights into the underlying anatomical and developmental principles of the most common epileptogenic cortical malformations.

RÉSUMÉ

Contexte. Les malformations du développement cortical (MDC) sont un groupe d'anomalies congénitales caractérisées par diverses déformations cérébrales et une importante épileptogénicité. L'imagerie par résonance magnétique (IRM) a révolutionné la prise en charge clinique de ces pathologies en raison de sa capacité incomparable à mettre en évidence des caractéristiques pathologiques. Cependant, sa sensibilité actuelle ne permet pas d'identifier la lésion focale dans l'ensemble du spectre des MDC, notamment dans le cas de discrètes anomalies, rendant difficile un diagnostic clinique fiable. Différentes études basées sur des données histologiques et d'IRM ont indiqué que des anomalies structurelles au niveau de la lésion focale pourraient s'étendre à des régions corticales éloignées. Alors que ces découvertes, associées à la preuve de réseaux fonctionnels épileptogènes, suggèrent des substrats pathologiques distribués, les modèles anatomiques et principes topologiques sous-jacents aux MDC demeurent peu clairs.

Objectif. Développer des méthodes computationnelles et d'imagerie multimodale avancée pour identifier et caractériser les MDC, ainsi que phénotyper la structure de l'ensemble du cerveau et son organisation en réseau**.**

Méthodes. Nous avons effectué les projets suivants : 1) Implémentation d'une méthode de classification par apprentissage automatique reposant sur des paramètres IRM, afin de détecter de discrètes malformations; 2) Evaluation d'altérations structurelles du cerveau entier en utilisant l'épaisseur corticale et la complexité des circonvolutions corticales; 3) Développement d'un nouveau cadre pour caractériser la morphologie, l'intensité, la diffusion et la fonction de la lésion coupable; 4) Analyse statistique et selon la théorie des graphes du réseau cérébral structurel et fonctionnel chez les patients atteints de MDC. Dans les projets 1 à 3, nous avons ciblé des patients avec des dysplasies corticales focales (DCF), tandis que le pour le projet 4 ont été inclus les différents sous-types représentatifs des MDC**.**

Résultats. Dans le projet 1, notre classificateur a identifié avec précision de subtiles DCF initialement négligées par une évaluation radiologique de routine. L'algorithme a montré une excellente sensibilité (74%) et une spécificité parfaite (100%, aucun faux positif). La performance a révélé une bonne généralisation des résultats à travers différentes cohortes, IRM et intensités de champs. Dans le projet 2, nous avons démontré que les anomalies s'étendent à partir de la lésion primaire vers des aires corticales éloignées, selon des modèles dépendant de différents sous-types pathologiques. Spécifiquement, les DCF de type I (uniquement caractérisées par une dyslamination à l'histologie) présentaient un amincissement cortical étendu, tandis que les DCF de type II (dyslamination et neurones dysmorphiques) étaient associées à un épaississement cortical bilatéral. La complexité des circonvolutions corticales divergeait également, augmentée dans les DCF de type I et diminuée dans celles de type II. Le projet 3 nous a permis de distinguer par IRM, au sein des sous-types de DCF sus-décrits, différentes entités : les DFC de type IIA, caractérisées par des neurones dysmorphiques isolés, et celles de type IIB, où une dyslamination est associée à la présence de cellules en ballons. En effet, en utilisant un profilage avancé intralésionnel et sous-cortical, nous avons retrouvé des marqueurs d'altération de morphologie, d'intensité, de diffusion et de fonction dans le type II-B, tandis que les DCF de type II-A se présentaient uniquement avec des changements modérés d'intensité et de diffusion près de la jonction substance blanche – substance grise. Ces découvertes à l'échelle des groupes étaient validées à l'échelle individuelle par l'algorithme d'apprentissage machine, qui prédisait à partir des critères IRM les sous-types histologiques de FCD in vivo avec une efficacité supérieure à 90%. Enfin, le projet 4 a montré une réogranisation du réseau à large échelle dans les MDC. L'importance des anomalies suit un gradient possiblement en rapport avec l'évolution chronologique du processus malformatif sous-jacent. En effet, les FCD de type II, liées à des anomalies de la prolifération neuronale se déroulant aux premiers stades du développement

cortical, présentent de discrets changements. Les hétérotopies de substance grise, liées à des anomalies de la migration neuronale, montrent quant à elles des changements intermédiaires. Enfin, les polymicrogyries liées à une désorganisation corticale tardive présentent une altération marquée de l'architecture du réseau cortical.

Conclusion. Les modèles computationnels proposés permettent la détection des lésions malformatives les plus discrètes avec une précision jamais atteinte, ouvrant la voie à un traitement chirurgical pour les patients chez qui les méthodes conventionnelles ne permettaient pas d'établir un diagnostic. De plus, nos études dévoilant des propriétés organisationnelles de l'ensemble du cerveau, offrent un nouveau regard sur les principes sous-jacents anatomiques et développementaux des malformations corticales épileptogènes les plus fréquentes.

ORIGINAL CONTRIBUTIONS

Project 1. Automated detection of focal cortical dysplasia in MRI-negative epilepsy

We developed pattern-learning techniques that yield >70% sensitivity in patients with cortical dysplasia reported as MRI-negative by standard radiological evaluation, providing the highest level of case-control diagnostic evidence (Class II). The performance of our computerized image analysis algorithm demonstrated high specificity and was generalizable across different patient cohorts, scanners, and field strengths.

Project 2. Whole-brain phenotyping of dysplasia-related frontal lobe epilepsy

Performing whole-brain morphometry in patients with focal cortical dysplasia, we demonstrated extensive structural damage beyond the visible lesion. Notably, changes showed distinctive patterns between pathological subtypes, namely Type-I and Type-II. By successfully guiding automated subtype classification, seizure lateralization and outcome prediction, our group-level findings demonstrated high translational value for individualized diagnostics.

Project 3. Multimodal MRI profiling and histological prediction

Our lesional profiling framework combined morphometry with metrics interrogating tissue intensity, microstructure, and function in histologically-verified focal cortical dysplasia Type-II. Assessing intra- and subcortical features, we provided the first evidence of distinctive imaging signatures between Type-IIA (characterized by isolated dysmorphic neurons) and IIB (dysmorphic neurons together with balloon cells). Machine-learning validated group differences at individual level by automatically predicting subtypes with excellent accuracy. Our ability to dissociate subtypes of cortical dysplasia at a mesoscopic level emphasizes the power of image processing applied to widely available MRI contrasts.

Project 4. Mapping brain network alterations across the spectrum of cortical malformations

We demonstrated that the degree of large-scale structural and functional network reorganization relates to distinct mechanisms and timing underlying the anomalous cortical development. Indeed, subtle network anomalies were associated with a malformation group related to abnormal neuronal proliferation (focal cortical dysplasia Type-II), intermediate effects were found in a group due to aberrant migration (heterotopias), while the most marked changes were associated to a group due to abnormal cortical organization (focal cortical dysplasia Type-I with mild dyslamination and polymicrogyrias).

TABLE OF CONTENTS

LIST OF FIGURES

4.5. **Machine-learning framework applied to cortical dysplasia subtype prediction.**

5.1. **Image processing**

5.2. **Multi-surface lesion profiling**

5.3. **Morphological profiling**

5.4. **Distance-based profiling of the lesion perimeter**

5.5. **Histological correlation**

5.6. **Automated subtype prediction of focal cortical dysplasia based on supervised pattern-learning**

6.1. **Inter-regional covariance and group differences across malformations of cortical development**

6.2. **Small-world parameters**

6.3. **Rich-club organization**

6.4. **Resting-state functional organization and its relation to structural network**

6.5. **Reliability test for different scales of parcellation**

6.6. **Reliability test for different datasets**

LIST OF TABLES

ABBREVIATIONS

AAL	Automated anatomical labeling
ALFF	Amplitude of local functional fluctuation
CI	Confidence interval
CLASP	Constrained Laplacian anatomic segmentation using proximity algorithm
CP	Cortical plate
Cp	Clustering coefficient
CSF	Cerebrospinal fluid
d-MRI	Diffusion tensor imaging
DPARSF	Data processing assistant for resting-state fMRI
EEG	Electroencephalography
FA	Fractional anisotropy
FCD	Focal cortical dysplasia

FDG	Fluorodeoxyglucose
FDR	False discovery rate
FLAIR	Fluid attenuation inversion recovery
FN	False negative
FP	False positives
FWE	Family-wise error
GABA	Gamma-Aminobutyric acid
GM	Gray matter
GTCS	Generalized tonic-clonic seizures
GW	Gestational week
HET	Heterotopia
ICBM	International consortium of brain mapping
Lp	Characteristic shortest path length
MCD	Malformation of cortical development
MD	Mean diffusivity
MPRAGE	Magnetization-prepared rapid-acquisition gradient echo
MRI	Magnetic resonance imaging
PET	Positron emission tomography
PMG	Polymicrogyria
ReHo	Regional homogeneity

RI	Relative intensity
rs-fMRI	Resting-state functional MRI
SD	Standard deviation
SEEG	Stereoelectroencephalography
SPECT	Single-photon emission computed tomography
SVZ	Subventricular zone
SVM	Support vector machine
TE	Time echo
TLE	Temporal lobe epilepsy
TN	True negatives
TP	True positives
TR	Repetition time
VBM	Voxel-based morphometry
VZ	Ventricular zone
WM	White matter

PART I

INTRODUCTION

CHAPTER 1

OVERVIEW

Corticogenesis entails a series of complex developmental processes characterized by multiple interacting genetic, epigenetic, and environmental factors [1]. Any disturbance during these processes may cause malformations of cortical development that are often related to neurological and neuropsychiatric disorders. Specifically, focal cortical dysplasia, a malformation due to abnormal neuronal proliferation and cortical organization [2], has been increasingly recognized as a cause of drug-resistant extratemporal lobe epilepsy, affecting 25-40% of cases [3]. It is now widely accepted that complete surgical resection of the dysplastic lesion is the most effective treatment in these patients [4, 5].

Recent advances in MRI have revolutionized the clinical diagnosis of malformation-related epilepsy by allowing an accurate *in-vivo* identification of the primary lesions in increasing number of patients [6]. Although the lesion generally presents with distinctive radiological features, the degree and patterns of these signatures vary significantly across patients, possibly due to different underlying histopathological anomalies [7]. Notably, lesions with a mild degree of anomalies are often unremarkable on standard clinical MRI (referred to as "MRI-negative"), substantially

challenging clinical management because of the difficulty in defining the surgical target [8]. Importantly, retrospective analysis of histopathological data in approximately 30-50% of MRI-negative patients reveals the presence of epileptogenic lesions - mainly dysplasias [9, 10]. While mild cyto- and myeloarchitectural anomalies may not be directly visible on conventional imaging, they have measurable effects on high-resolution MRI, especially when combined with advanced computational modeling [11, 12].

Because of the key role of MRI in identifying the surgical target, imaging studies in cortical malformations have been primarily dedicated to lesion characterization and identification in single patients. Nevertheless, growing evidence from animal models [13], histology [14, 15], and quantitative MRI [16, 17] indicate that brain abnormalities extend beyond the primary lesion. Functional studies also suggest that cortical malformations are associated with widespread epileptogenesis [18] and cognitive dysfunction in multiple domains [19, 20]. These separate lines of evidence suggest widespread pathological substrate in malformations of cortical development. Yet, whole-brain anomalies and their organizational principles remain largely unexplored.

The overall goal of this thesis is to perform comprehensive *in-vivo* assessment of neocortical morphology, subcortical white matter integrity and network-level organizational properties of various malformations of cortical development, both in lesional and extra-lesional areas. Our approach rests on the integration of multiple image modalities through a surface-based sampling that respects cortical topology and provides accurate inter-subject correspondence.

We carried out the following specific experiments:

1. Developing a fully-automated machine-learning algorithm to detect lesions initially overlooked by radiological diagnosis. A surface-based classifier aggregated morphometric and texture features, modeling typical characteristics of focal cortical dysplasia (**page 48**).
2. Mapping whole-brain morphology in dysplasia-related drug-resistant epilepsy. Assessing the histopathological spectrum of dysplasia, we evaluated group-level alterations of cortical thickness and folding complexity, and examined their clinical utility (**page 68**).
3. Mapping intra- and subcortical tissue integrity of the primary malformative lesion. Our profiling evaluated lesional and peri-lesional characteristics across various cortical and subcortical levels, and incorporated both structural and functional features. The *in-vivo* framework automatically predicted histopathological subtypes (**page 87**).
4. Graph theoretical analysis of structural-functional networks in malformations of cortical development. Connectivity and topological parameters were systematically assessed across the most common subtypes of malformations, both at global and nodal levels. We also evaluated group-level differences in structure-function coupling. (**page 109**).

The thesis is organized as follows: Chapter 2 (**page 28**) reviews the background literature. Chapters 3 to 6 are a series of manuscripts that describe the performed experiments. The final Chapter (**page 139**) summarizes the key findings and highlights the significance of this work.

CHAPTER 2

BACKGROUND

Normal brain development

Brain development is highly complex, yet precisely orchestrated molecular events involving a vast number of genes. The whole process is largely divided into three main stages, namely, neuronal proliferation, migration, and post-migratory cortical organization [21]. An overall snapshot of these stages is shown in **Figure 2.1**.

Neuronal proliferation: the formation of the ventricular and subventricular zones (**Figure 2.1A)**
Upon completion of embryogenesis (4th gestational week, GW), the human forebrain forms a smooth sheet entirely occupied by neuroepithelial cells. During the early period of this stage, these cells divide symmetrically at the margin of the ventricle [22], gradually increasing the number of progenitor cells, resulting in both increased surface area and thickness of the ventricular zone (VZ) [23]. From approximately the 5th GW, progenitor cells (also called radial glia cells) in the VZ begin to switch from symmetric to asymmetric cell division [24]. In turn, one daughter cell becomes another radial glial cell, while the other develops into either a post-mitotic neuron or an intermediate

progenitor cell [25]. Notably, an accumulation of intermediate progenitor cells creates a new distinct compartment above the VZ, namely the subventricular zone (SVZ) [26, 27]. While the neuronal proliferation in the VZ starts to attenuate after the 18th GW [28], the SVZ maintains its original proliferative role, actively producing more pyramidal neurons throughout the whole developmental period [29].

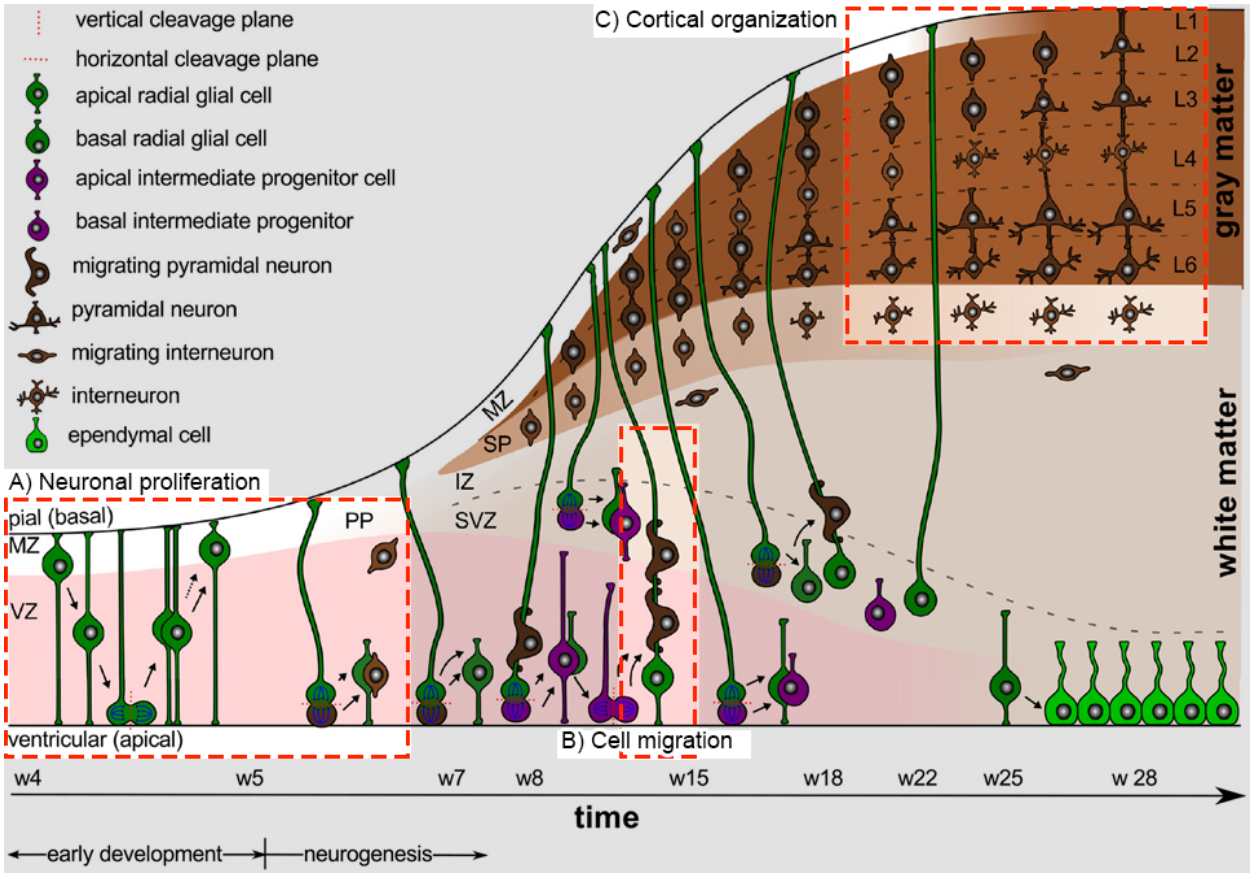

Figure 2.1. An overall snapshot of corticogenesis. The figure was reproduced from Budday et al. *Front Cell Neurosci. 8;9:257* [30].

Neuronal migration: radial and tangential mode (**Figure 2.1B)**

After the 7th GW, the cortical plate (CP) - a primitive structure of neocortical gray matter (GM) in the mature brain [22] - starts to develop, as newborn neurons initiate a translocation of cell bodies from the proliferative zone to their target layers in the CP. This elaborate cell movement, the so-called neuronal migration, has two different modes: 1) the radial migration, in which post-mitotic cells migrate vertically upwards from the VZ along a radial glial scaffold, and 2) the tangential migration, in which cells migrate parallel to the pial surface while being directed by surrounding molecular cues [31]. In general, neurons in the VZ take the radial mode of migration and accumulate in the CP in an inside-out and early-late fashion [32]. In other words, early-born neurons form a layer at the most basal level of the CP and subsequently the younger neurons travel through layers of older neurons to accumulate above them, gradually expanding the layers in outward direction. Notably, 80% of radially migrating neurons develop into excitatory glutamatergic neurons in the CP [32]. Conversely, neurons that develop into GABAergic inhibitory interneurons migrate tangentially by traveling several hundred micrometers in parallel to the pial surface [32]. These cells were largely produced in the subpallium, a ventral forebrain area that contains the lateral and medial ganglionic eminences [31]. These two structures eventually give rise to the basal ganglia and amygdala in the adult brain [33].

Post-migratory cortical organization

The period after the 22nd GW is the most significant time for post-migratory cortical differentiation. The process occurs along two orthogonal, horizontal (areal) and vertical (laminar) directions. After areal differentiation, rostral regions of neocortex are generally responsible for executive and motor functions, while caudal regions are engaged with somatosensory, auditory, and visual inputs [34].

Two distinct hypotheses have been proposed for this functional specialization: 1) the *proto-cortex* and 2) the *proto-map* hypothesis [34, 35]. The first postulates that early-formed uniform cortical areas selectively receive different somatosensory and high-order neuronal information from the thalamus [36]. The constant input from the thalamus signals the premature cortical areas to progressively identify and consolidate their final functions. On the other hand, the proto-map hypothesis [37] suggests that during a period of neuronal proliferation, differential gene expression in newborn neurons in VZ guide them to attract appropriate inputs from thalamus.

Cortical differentiation also occurs along the vertical direction (**Figure 2.1C**). Indeed, a laminar development that begins already at a migration phase continues until the late period of corticogenesis. While many theoretical and empirical studies tried to address the principles related to this process, evidence is currently converging to the resultant effects of substantial interactions between layer-specific genes such as *Cux1-2* or *Foxp2* and a set of proteins diffused in extracellular matrix such as *Reelin* [38, 39], which collectively regulate the layer positioning of migrating neurons. The cortex starts to show areas fully developed into six layers around GW 18 [21]. In parallel, it also undergoes several processes of cellular differentiation, including development of cell body [40], selective cell death [41] and extensive axonal and dendritic expansion [30]. At GW 28, layer 1 is already filled with arborization of apical dendrites and tangential axons from early-generated neurons, and radial glial cells in subcortical layers disappear or become astrocytes. In GW 24–34, axons undergo myelination process, gradually transforming the original intermediate zone into mature white matter (WM) tissue [21].

Malformations of cortical development

Any disturbance during corticogenesis could lead to malformations of cortical development, a frequent causes of chronic epilepsy. Indeed, an estimated 75% of epilepsy cases are associated with various types of cortical malformations [42], a considerable portion (~40%) of whom develops into drug-resistant forms [43]. Uncontrolled epilepsy is harmful to the brain [44], and has devastating cognitive consequences [45, 46]. Given that a timely and precise clinical diagnosis is critical for optimizing a drug treatment and surgical planning, developing effective biomarkers to accurately identify and characterize malformative lesions is a clinical priority.

Cortical malformations subtypes

The updated taxonomy proposes a sub-grouping system based on the putative onset timing of malformative process [2]: secondary to 1) early abnormal neuronal and glial proliferation or apoptosis; 2) abnormal neuronal migration; 3) abnormal late post-migrational organization (see **Table 2.1** and **Figure 2.2** for clinical details and MRI of each group). Group 1 includes focal cortical dysplasia (an isolated lesion associated with dysmorphic neurons and balloon cells). Group 2 includes periventricular or subcortical heterotopia (abnormally arrested neuronal clusters along the ventricular wall or between cortex and lateral ventricles) and classic lissencephaly (smooth brain). Group 3 includes polymicrogyria (excessive number of small gyri and shallow sulci) and mild cortical dysplasia (subtle cortical dyslamination, ectopic WM neurons). While this classification is generally very useful and readily applicable in practical clinical diagnosis, actual genetic involvements and behavioral outcomes across patients are often far more heterogeneous than what the given system presents [47]. In following paragraphs, we will review few representative subtypes of cortical malformations in depth, mainly focusing on focal cortical dysplasia, the primary research interest of the current thesis.

TABLE 2.1. Classification and clinical/genetic features of malformations of cortical development

Developmental stage	Cortical malformation	Genetic cause †	Clinical Features †	Incidence †
Neuroglial proliferation	Microcephaly	ASPM, CDKRAP5, MCPH1	Mental retardation, not generally associated with epilepsy	<1%
	Megalencephaly	PI3K-AKT	Mental retardation, early onset seizures	2%
	Focal cortical dysplasia Tuberous sclerosis	TSC1, 2	Normal-to-severe cognitive dysfunction	20-40%
Neuronal migration	Periventricular heterotopia	ARGGEF2, FLNA, LIS1	Neurodevelopmental delay, adolescent onset seizures	2-20%
	Subcortical band heterotopia	DCX, LIS1	Mental retardation, epilepsy	9%
	Lissencephaly	DCX, LIS1	Severe language deficit and social interaction, epilepsy	<1%
Post-migratory development	Polymicrogyria	GPR56	Intellectual disability, movement disorder, seizures	5-16%
	A mild cortical dysplasia (without dysmorphic neurons)	Unknown	Cognitive decline, early onset epilepsy	13%

† Genetic cause and incidence information based on [47-53]

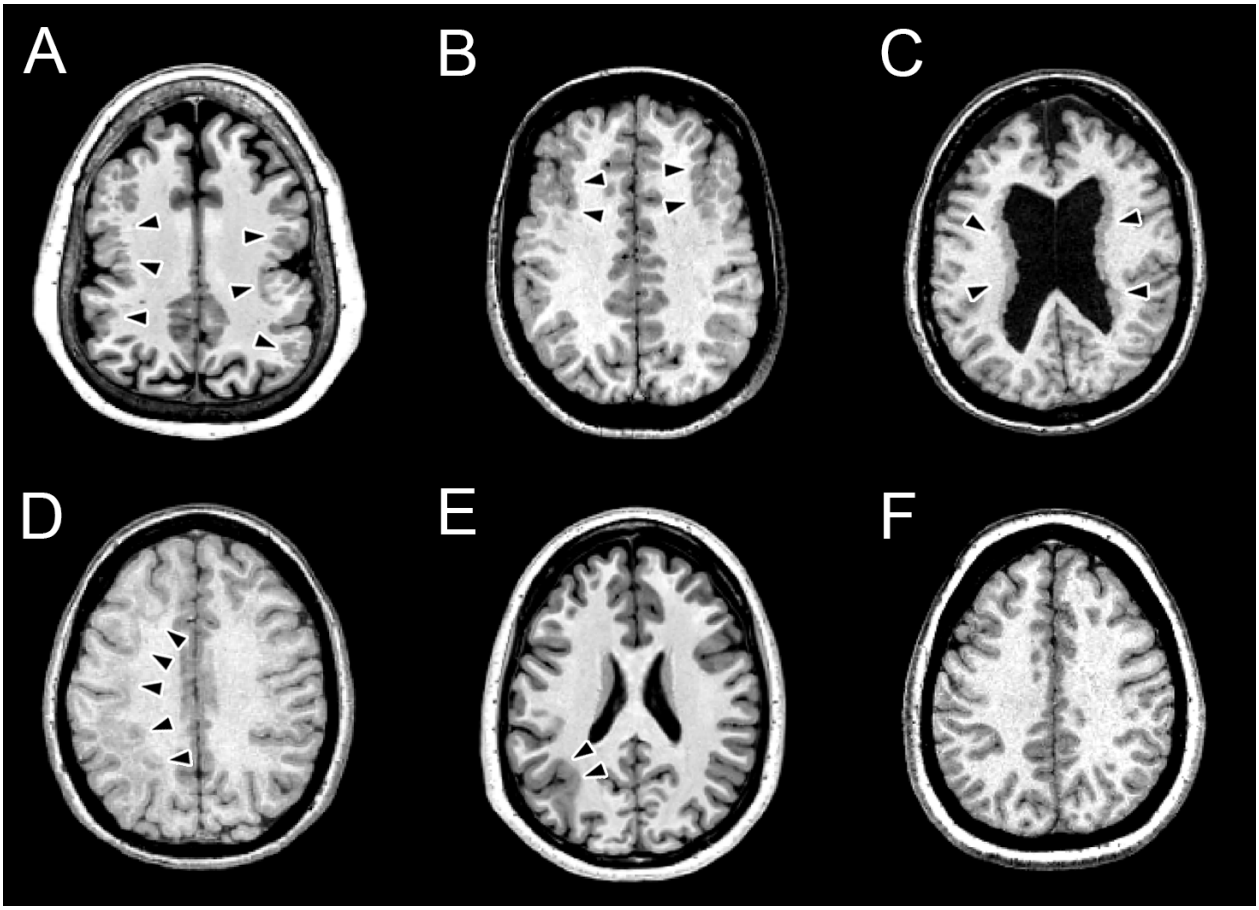

Figure 2.2. MRI of cortical malformations. A) Bilateral perisylvian polymicrogyria, B) Bilateral fronto-parietal polymicrogyria, C) Bilateral periventricular heterotopia, D) Subcortical band heterotopia ("double cortex"), E) focal cortical dysplasia Type-II and F) focal cortical dysplasia Type-I (MRI-negative). Lesions are indicated by the arrow heads.

1) Polymicrogyria (**Figure 2.2A-B**)

This epileptogenic lesion accounts for 5-16% of malformations of cortical development [49, 54] and has characteristics of an overly folded brain surface – resulting in excessive small gyri – and

abnormal patterns in deep cortical layers [50]. About 75% of lesions are bilateral, often located around the sylvian fissure (80%) and in the frontal lobes (70%) [55]. The most frequently associated gene is ADGRG1 (ADhesion G protein-coupled Receptor G1), specifically for bilateral fronto-parietal polymicrogyria, and its normal function during development is involved in regulation of brain cortical patterning (*e.g.*, lamination and maintenance of membrane) or neuronal migration [53]. Patients with this malformation may present with cognitive and motor delay [47].

2) Heterotopia (**Figure 2.2C-D**)

This malformation is characterized by a mass of neuronal cells ("nodules") that has been abnormally arrested during migration [2]. It is generally divided into three subtypes according nodule location: subependymal (periventricular nodular), subcortical and band heterotopia [2, 56, 57]. Epilepsy is the main clinical symptom, observed in 90% of patients [50]. Invasive electrographic studies suggested that nodules play a role in the generation of epileptic discharges [58]. Surgical resection of nodules is rarely considered as they tend to be located in deep WM and are often widespread [59]. Frequently associated genes include ARGGEF2, FLNA1, and DCX, which control soma translocation and microtubule skeletonization [47]. Although behavioral outcomes vary across patients, several reports have shown neurodevelopmental delays, particularly in cases with classical periventricular heterotopia [42].

3) Focal cortical dysplasia (**Figure 2.2E-F**)

Focal cortical dysplasia is one of the most frequently observed pathologies in drug-resistant extra-temporal lobe focal epilepsy (up to 50%) [3]. This malformation encompasses a broad spectrum of histopathological abnormalities including cortical disorganization as a cardinal characteristic. Associated features include cytopathology (large dysmorphic neurons and balloon cells) and gliosis caused by proliferation and hypertrophy of astrocytes [7]. Based on these anomalies, a recent

new classification proposed a three-tiered categorization system (**Table 2.2**) [60]: 1) *Focal Cortical Dysplasia Type-I* is characterized by an isolated malformation with abnormal cortical layering, either showing persistence of vertical developmental microcolumns (I A) or loss of the horizontal hexalaminar structure (I B), or both (I C); 2) *Type-II* presents with completely disorganized cortical layering and specific cytopathology including dysmorphic neurons, either isolated (II A) or together with balloon cells (II B); 3) *Type III* comprises architectural abnormalities associated with either hippocampal sclerosis (III A), tumors (III B), vascular malformations (III C) or other lesions acquired during early life (III D).

Compromised microcolumns in Type-IA dysplasia is characterized by more than 8 neurons (=2×SD from the mean of controls) aligned in a vertical direction along the cortex, predominantly in layer 3-4 [61]. The tissue harboring such microcolumns presents with a reduced cell size and increased neuronal densities, as well as a tendency of decreased cortical thickness, compared to healthy cortices [61, 62]. On the other hand, dysmorphic neurons, a main component of Type-II lesion, have either a pyramidal or interneuronal phenotype and are characterized by significantly enlarged soma and nucleus compared to normal cortex [62]. While sharing some commonalities with dysmorphic neurons (including a gigantic cell body and accumulated intermediate filaments [63],) balloon cells have multiple displaced nuclei and are electrically silent[64]. So far only Type-II lesion has been systematically associated with specific genetic etiology (*e.g.*, TSC1, 2) [50]. Abnormal expression of these genes disrupts normal signaling of mammalian target of rapamycin, a core developmental pathway which governs initial cell growth and proliferation, resulting in immature balloon cells and dysmorphic neurons [65].

TABLE 2.2. Three-tiered classification system of focal cortical dysplasia [60]

Cortical dysplasia Type-I (isolated)	Cortical dysplasia with abnormal radial lamination (Type-IA)	Cortical dysplasia with abnormal tangential cortical lamination (Type-IB)	Cortical dysplasia with abnormal radial and tangential cortical lamination (Type-IC)	
Type-II (isolated)	Cortical dysplasia with dysmorphic neurons (Type-IIA)		Cortical dysplasia with dysmorphic neurons and balloon cells (Type-IIB)	
Type- III (associated with a principal lesion)	Cortical lamination abnormalities in the temporal lobe with hippocampal sclerosis (Type-IIIA)	Cortical lamination abnormalities adjacent to a glial or glioneuronal tumor (Type IIIB)	Cortical lamination abnormalities adjacent to vascular malformation (Type-IIIC)	Cortical lamination abnormalities adjacent to any other lesion acquired during early life (Type-IIID)

The role of MRI in characterizing cortical malformations

Magnetic resonance imaging (MRI) has revolutionized the management of malformation-related drug-resistant epilepsy because of its unparalleled ability to visualize epileptogenic lesions *in vivo* [6]. For instances, megalencephaly, classically characterized by partial or complete enlargement of a given hemisphere, is often associated with poor differentiation of the interface between the GM and WM as well as subcortical intensity changes on T2-weighted images. In lissencephaly, the brain surface consists of areas of absent or abnormally wide gyri, which often show markedly increased cortical thickness (8-15mm). The heterotopic nodules and the polymicrogyric cortex also show hypo- or hyperintensity of signals, atypical sulcal patterns and severe asymmetry of brain structures [50]. Recent advents in MRI acquisition technology, specifically high-field imaging (*e.g.,* 3 or 7 Tesla) combined with multiple phased-array head coils, have allowed for an increasingly

precise characterization of the primary lesion, facilitating the description and classification of malformations of cortical development [47]. Indeed, a recent high-field MR imaging study of perisylvian polymicrogyrias reported that compared to the conventional MRI which only reveals thick GM and a coarse level of sulcogyral pattern, a susceptibility-weighted imaging acquired at 7T provides a higher definition of the irregular thickness and folding pattern of the polymicrogyric cortex [66].

Compared to other malformations, however, lesions of focal cortical dysplasia may go unrecognized by standard radiological analysis [8]. This is due to the fact that identification of these malformations on visual inspection of conventional MRI is difficult due to their subtlety, their variable imaging signature and the complexity of the brain's convolution.

Imaging characteristics of focal cortical dysplasias (see **Figure 2.2E**)

Main features of cortical dysplasia on structural MRI include abnormally thick GM (50–92% of cases) and blurring of the GM-WM interface (60–80% of cases) [3, 14]. Analysis of T2-weighted images reveals GM hyperintensity in 46–92% of lesions and sensitivity of FLAIR images is even higher (71–100%). The typical transmantle sign, a footprint of disrupted cell migration along radial glial processes, presents as a funnel-shaped hyperintensity extending from the ventricle to the lesion and is seen in the majority of Type II cases [14, 67, 68].

The *in-vivo* visibility of dysplastic changes on MRI generally parallels the degree of histopathological derangement [3]. Even in patients with a Type II dysplasia, however, as the radiological spectrum on MRI encompasses variable degrees and patterns of GM and WM changes, visual identification can be challenging, particularly when inspecting the convoluted neocortex in two dimensional images. Indeed, recent surgical series indicate that up to 33% of Type II and 87% of Type I dysplasia [14, 67, 69] present with unremarkable routine MRI. Notably, it is becoming

increasingly clear that neocortical dysplasias constitute a spectrum of histopathology, clinical, and radiological presentations broader than originally suspected [3, 60, 67, 69-72]. Indeed, epilepsies initially considered MRI-negative are not necessarily non-lesional since in 30%-50% of those patients who undergo surgery, histological examination of the resected specimens reveals dysplasias [3, 9]. Nevertheless, the imaging signature of Type-I dysplasia, characterized by subtle cortical thinning and dyslamination [60], remains elusive. This clinical difficulty has motivated the development of computer-aided methods aimed at analyzing brain morphology and signal intensities. Such procedures provide distinct information through quantitative assessment without the cost of additional scanning time or exposure to ionizing radiation.

Voxel-based lesion detection frameworks

Voxel-based morphometry (VBM) is a widely applied imaging post-processing technique, originally developed in order to evaluate whole-brain tissue morphology [73]. It relies on an automated tissue classification (*i.e.,* GM, WM and CSF) followed by Gaussian image smoothing to generate voxel-wise brain tissue density map, on which statistical analyses are performed. Several groups have applied VBM to detect structural abnormalities related to MRI-visible dysplasia in single patients [74]. This fully automated image processing method, which identifies differences in tissue density at a voxel level, detects increases in GM concentration co-localizing with the lesion in 63-86% of cases. Histopathological confirmation of lesions that eluded visual inspection (despite their relatively large size) [75] suggests that VBM may be applied to investigate patients with MRI negative epilepsy. Importantly, however, a threshold of 2SDs above the mean GM concentration in healthy controls does not guarantee specificity of findings since, at this threshold, false positives may occur in control subjects. Voxel-based comparison has also been used to analyze intensities derived from quantitative MRI contrasts such as T2 relaxometry, double

inversion recovery, and magnetization transfer imaging. These approaches have shown high sensitivity (87%-100%) in detecting obvious malformations of cortical development [76-78]. Nevertheless, these techniques may identify areas concordant with clinical and EEG findings in less than a third of MRI-negative cases and have low specificity [77, 79].

The relatively unspecific nature of VBM with respect to pathological characteristics of cortical dysplasia has motivated the search for computer-based models of morphological imaging features distinctive to the lesion. In the early 2000's, *Bernasconi, et al*. introduced a novel approach to integrate voxel-wise texture and morphological modeling of three main features in the lesion (*i.e.*, cortical thickening, blurred GM-WM junction and relative intensity alterations) into a single composite map (**Figure 2.3A**) [80]. This semi-automated algorithm demonstrated that computational models could assist in the detection of focal cortical dysplasia (sensitivity: 87.5%, specificity: 95%), substantially increasing the detection rate of visual identification. Moreover, blending these models with the quantification of high-order image texture features that cannot be discriminated by the human eye, they were able to detect automatically about 80% of dysplastic anomalies [81, 82].

Subsequently, *Huppertz et al* introduced a semi-automated pipeline called Morphometric Analysis Programme for enhanced visualization of lesions. This technique uniquely creates a so-called "junction" image, a map which identifies voxels that are not definitively GM or WM, to signify high likelihood of tissue blurring [83]. By combining this map with other conventional features (*i.e.*, cortical thickness and intensity maps), this approach demonstrated a comparable sensitivity (84%). Beyond the lesion detection, in order to better cover the full extent of the lesion, the previous study by *Colliot* [84] proposed an automated lesion segmentation algorithm based on level-set-based deformable models (**Figure 2.3B**) .

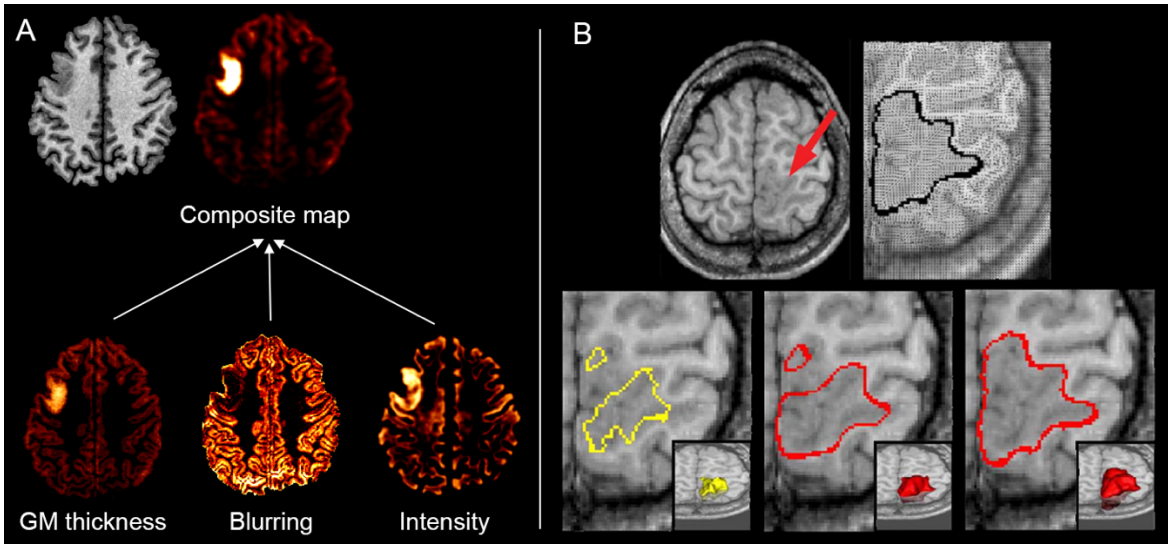

Figure 2.3. Voxel-wise post-processing for lesion detection and segmentation. A) Upper panel: A cortical dysplasia located at the left frontal lobe is highlighted in a composite map. Bottom: Individual features present with increased GM thickness, altered intensity and reduced gradient of the lesion. The composite map is computed as follows [(GM thickness×relative intensity)/intensity gradient]. B) Lesion segmentation. Upper: A red arrow indicates the lesion. Final result shown together with gradient vector flow. Bottom: After initializing with the lesion detection result of the classifier (yellow), a deformable model gradually expands the lesional boundary (red) following gradient vector flow.

Although these voxel-based approaches offer an automated and exploratory analytic framework of whole brain structural changes, one of their limitations is that they do not fully take into account the complex topology and are prone to volume averaging of non-adjacent cortical regions across sulci, potentially increasing the false positive rates. Moreover, high anatomical variability in gyrification and sulcation across individuals may reduce the specificity and sensitivity to detect significant effects, even after a non-linear image registration step that is used to normalize brains [85-87]. These drawbacks dramatically limited the clinical utility of voxel-based approaches, and motivated the field to adopt alternative frameworks.

Surface-based analytic framework

Compared to VBM-type approaches, surface-based measurements offer a more direct and biologically meaningful way to quantify cortical structural integrity as they respect the anatomy of the folded cortical surface. Since early 2000s, several image processing methods have been developed to enable the automatic measurement of cortical surfaces that have corresponding points between the GM and WM interface across the entire cortical mantle [88, 89]. The "CIVET" developed at the Montreal Neurological Institute is one of the widely used automated image processing pipelines that includes the algorithm of Constrained Laplacian Anatomical Segmentations using Proximity algorithm (CLASP) for cortical surface extraction [90].

All projects in this thesis were carried out based on the CIVET/CLASP pipeline (**Figure 2.4**). This pipeline first takes the native-space T1-weighted MRI images as input and perform a non-uniformity intensity correction [91] and linear registration to standardized template based on the Talairach atlas [92]. Registered images are classified into GM, WM, and CSF using an automated classifier that takes into account intensity information as well as spatial anatomical priors that were derived from a large training set [93]. Recently, in order to address challenges during segmentation such as regional intensity variation due to local radiofrequency artifacts or disparities in tissue composition, a novel anatomy-driven algorithm has been proposed [94]. This approach carries out tissue segmentation by the unit of a local parcel which conforms the cortical anatomy, therefore, maximizing a regional tissue contrast and significantly improving the GM-WM border definition compared to conventional methods. A subsequent partial volume classification step is invoked that improves the detection of buried sulci as well as the discrimination between insular cortex and subcortical GM structures [95]. To generate the model of the cortical surface, the CLASP algorithm iteratively warps a surface mesh to fit the boundary between WM and GM in the classified image. It then expands the WM/GM boundary along a Laplacian map to generate a second outer surface

that runs along the GM/CSF boundary [90]. To improve anatomical correspondence of vertices in all subjects, surfaces are then non-linearly aligned to an iteratively generated surface template [96] using a 2D registration procedure that minimizes differences in cortical folding [97]. By achieving a better alignment of sulco-gyral patterns across subjects, this procedure indeed demonstrated higher sensitivity to detect group-level findings compared to conventional voxel-based methods [98]. After completing whole pre-processing steps, the surface-based analysis allows to quantify a battery of morphometric features such as cortical thickness, folding complexity and sulcal depth, and also to model MRI intensities and gradients along the cortical ribbon, which collectively provide an integrative description of whole-brain cortical integrity.

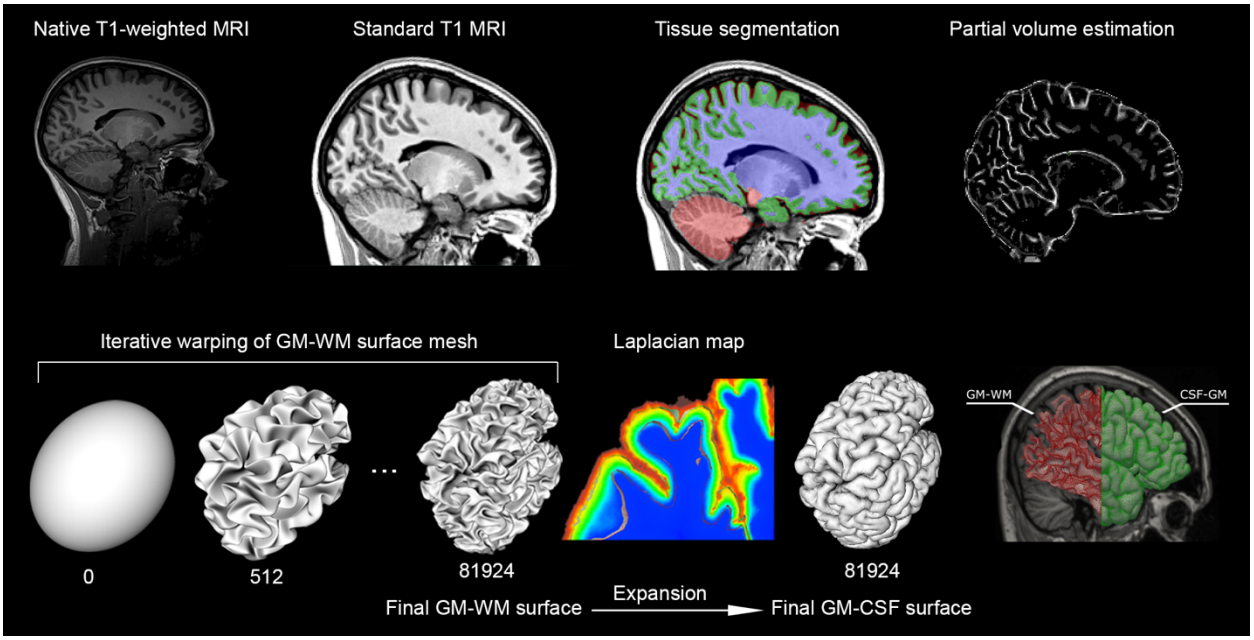

Figure 2.4. Cortical surface extraction. Please see the text (page 41-42) for methodological details.

MRI-based characterization of sulco-gyral abnormalities in cortical malformations

Radiological evidence indicates that focal cortical dysplasia can be associated with various degrees of sulcal anomalies, including broadening, increased depth and altered orientation [6, 63]. Surface-based techniques enriched the ways to capture such sulco-gyral anomalies in dysplastic lesions. For instance, *Besson, et al.* employed an automated sulcus labeling technique to elucidate the spatial relationship between cortical dysplasia and sulci, from which 85% of small lesions were found to be located at the bottom of an unusually deep sulcus [99]. Another recent study assessing patients with a lesion in central cortex (35% MRI-negative) found that a sulcus related to the lesion has a greater number of side branches and an unusual shape in 62% of cases [100]. To evaluate the clinical yield of these findings, *Roca* and *Régis* independently proposed an automated sulcus-based method to analyze abnormal folding patterns in individual patients with cortical dysplasia [101, 102]. By quantifying the degree of unusualness of each sulcus with respect to control database, these algorithms captured a significant association between sulcal abnormalities and the site of dysplastic lesions that is subtle on MRI.

Beyond the primary lesion: a large-scale pathology in cortical malformations

Because of the crucial role in defining the surgical target, MRI studies of cortical malformations have been primarily dedicated to lesion detection in single patients. Sporadic case reports and radiological studies, however, have suggested that structural anomalies may extend beyond the primary lesion [14, 16]. A recent study quantitatively assessing the GM-WM interface in patients with cortical dysplasia also found that a blurred tissue transition is not a localized anomaly only at the lesional side but, in fact, a widespread phenomenon spanning across the whole brain, although the histology only partially supported the findings because of tissue availability limited to the resected lesion areas [103]. These findings collectively suggest that cortical malformations may not be a pure focal disease with a single lesion, but rather a systemic disorder related to distributed pathological

substrates [104].

While this hypothesis has been so far tested mainly by univariate approaches (in which each brain area is probed separately), emerging mathematical frameworks, so called connectome and graph-theoretical analyses, enable to assess interregional relations between different cortical areas, taking advantage of their multivariate powers to model more complex pathological effects related to brain network. Particularly, *structural covariance analysis* is a method that allows to infer developmental organization [105-109]; it estimates either the co-varying patterns of morphometric features (*e.g.,* thickness, volume) across cases based on the cross-sectional data or maturational coupling of GM growth rate using individual longitudinal data [110]. The underlying assumption is that cortical regions belonging to the same structural network show a high degree of correlated growth during development, due to their high propensity to exchange trophic factors and their participation in common molecular signaling pathways [111-113]. Such highly organized patterns of structural network are indeed increasingly demonstrated in the human brain with several typical topological characteristics, including a small-world topology, a rich-club architecture for an integrative neuronal communication, and a marked tolerance against network perturbations [107, 114, 115]. In the context of cortical malformations, such topological organizations may develop abnormally. Indeed, it is plausible that the malformative process has an impact on brain areas within the same developmental network as the primary lesion are influenced by the malformative process, resulting in extra-lesional dysplastic cortices.

Compared to the covariance assessment that targets the developmental footprint of maturational GM growth coupling, functional network analysis probes more closely the "current" status of brain organization at mature patients' brain. So far only few studies have assessed the integrity of functional networks in malformations of cortical development. For example, fMRI studies evaluating a language function in this condition have shown that disruptions may not be limited to

the lesional cortex, providing evidence for intra- and inter-hemispheric redistribution of function [20, 116, 117]. On the other hand, sporadic reports based on resting-state functional imaging found that polymicrogyria and periventricular nodular heterotopia have abnormal brain topology [118, 119] or disrupted connectivity patterns [120-123].

Although these studies already provide preliminary evidence for distributed pathological substrates related to cortical malformations, they were either targeting specific cognitive networks (*e.g.*, language or reading) or based on small sample sizes. More importantly, a comprehensive evaluation including whole spectrum of disease and a multimodal assessment combined with structural covariance network has not been carried out; therefore, main principles regarding to a large-scale organization in malformations of cortical development remain poorly understood.

* * *

PART II

PROJECTS

CHAPTER 3

AUTOMATED DETECTION OF MRI-NEGATIVE CORTICAL DYSPLASIA

Preface

While previous voxel-based computational approaches improved the visibility of the lesion, they have primarily focused on large- or medium-size visible FCD. When obvious features of GM thickening and blurring are absent, abnormal sulco-gyral patterns may be an alternative marker of cortical dysgenesis. Indeed, a previous case study reported subtle cortical gyral abnormalities in patients whose MRI were previously deemed as normal and that resection of these areas resulted in favorable surgical outcome [10]. Sulco-gyral anomalies are, however, difficult to discriminate visually when images are inspected on orthogonal planes. Together with the intrinsic limitations of voxel-based approaches (*e.g.*, suboptimal image registration and a smoothing step neglecting true cortical geometry), this preliminary evidence motivated the development of a surface-based approach allowing for a sensitive modeling of subtle lesions of cortical dysplasia while respecting highly folded geometry.

Appropriate clinical translation of new image processing algorithms relies on comparable

performance against variable environments. Different image acquisition setup across sites, however, often leads to over-fitting on a single dataset, resulting in low reproducibility. Thus, to make novel imaging biomarkers effective and generalizable, analysis of their performance on clinical data should be evaluated through independent cross-validations across different scanners and cohorts.

The purpose of this study was to implement a surface-based automatic framework to detect the subtle lesion of cortical dysplasia based on machine-learning algorithms, and to evaluate the generalizability of its performance across different cohorts, scanners and field-strengths.

* * *

Abstracts

Our purpose was to detect automatically focal cortical dysplasia (FCD) type II in patients with extra-temporal epilepsy initially diagnosed as MRI-negative on routine inspection of 1.5 and 3.0 Tesla scans. We implemented an automated classifier relying on surface-based features of FCD morphology and intensity, taking advantage of their covariance. The method was tested on 19 patients (15 with histologically-confirmed FCD) scanned at 3.0 Tesla, and cross-validated using a leave-one-out strategy. We assessed specificity in 24 healthy controls and 11 disease controls with temporal lobe epilepsy. Cross-dataset classification performance was evaluated in 20 healthy controls and 14 patients with histologically-verified FCD examined at 1.5 Tesla. Sensitivity was 74%, with 100% specificity (*i.e.*, no lesions detected in healthy nor disease controls). In 50% of cases, a single cluster co-localized with the FCD lesion, while in the remaining a median of one extra-lesional cluster was found. Applying the classifier (trained on 3.0 Tesla data) to the 1.5 Tesla dataset yielded comparable performance (sensitivity: 71%, specificity: 95%).

In patients initially diagnosed as MRI-negative, our fully automated multivariate approach offered a substantial gain in sensitivity over standard radiological assessment. The proposed method showed generalizability across cohorts, scanners, and field strengths. Machine-learning may assist pre-surgical decision-making, by facilitating hypothesis formulation about the epileptogenic zone. This study provides Class II evidence that automated machine learning of MRI patterns accurately identifies FCD among patients with extra-temporal epilepsy initially diagnosed as MRI-negative.

This work was published in:
Hong SJ, Kim HS, Schrader D, Bernasconi N, Bernhardt BC, Bernasconi A. *Automated detection of cortical dysplasia Type II in MRI-negative epilepsy*. Neurology 2014. 83 (1), 48-55

3.2 Introduction

Focal cortical dysplasia (FCD) type II, an epileptogenic developmental malformation [72], is characterized by cortical dyslamination, hypertrophic and dysmorphic neurons, and balloon cells [60]; it is the most common histopathology in surgical series of extra-temporal lobe epilepsy [7]. Reliable detection of this lesion is critical for successful surgery [3].

On MRI, FCD type II is characterized by cortical thickening, blurring of the grey-white matter junction, and hyperintense signal [124]. Many lesions, however, elude best-practice neuroimaging protocols. To enhance visibility, previous studies have modeled its main features using voxel-based methods, such as texture and morphometric analysis [74]. The evaluation of multiple maps generated through these quantitative techniques is done visually, so that the yield and diagnostic confidence depend on the reader's familiarity with the algorithm. Limited generalizability also stems from the fact that these approaches have been validated mainly with lesions recognized on routine radiological evaluation [75, 125-128].

Here, we address the pressing issue of lesion detection in MRI-negative FCD. We combined machine learning with surface-based analysis in patients with FCD type II initially diagnosed as MRI-negative on routine radiological inspection. Compared to voxel-based techniques, a surface-based approach preserves cortical topology and quantifies sulco-gyral anomalies, at times the only sign of dysgenesis [129].

3.3 Methods

We present an automated algorithm trained on MRI-negative patients with histologically-confirmed FCD. We ruled out sources of spectrum bias [130] by evaluating the specificity of our

algorithm against healthy individuals and clinically well-characterized disease controls. To minimize incorporation bias, our classifier trained on 3.0 Tesla data was tested on an independent cohort of patients and controls examined at 1.5 Tesla. Our method provides Class II evidence for diagnostic accuracy [131].

Subjects

From a database of 45 consecutive patients with FCD admitted to the Montreal Neurological Institute (MNI) between 2009 and 2012 for the treatment of drug-resistant extra-temporal lobe epilepsy, we selected 19 subjects (9 males; mean ± SD age 29 ± 8 years) in whom the initial routine radiological assessment was unremarkable at both 1.5 and 3 Tesla, and thus diagnosed as MRI-negative. The dysplastic lesion was subsequently recognized through expert evaluation (A.B.) of texture maps [80, 82]. In the majority of patients (14/19 = 74%), the lesion had been overlooked likely because of its small size (mean ± SD volume = 877 ± 832 mm^3; range = 45-2,679 mm^3). In the remaining 5, although the lesion was relatively large (6,333±2,164 mm^3), it was not seen because of the mild degree of morphological and signal anomalies blending into the adjacent cortex. Lesions were located in the frontal (14), cingulate (2), parietal (2), and insular (1) cortices.

The pre-surgical workup included seizure history, neurological examination, neuroimaging, and video-EEG telemetry. Inter-ictal spikes had lateralizing value in 8 patients (42%); ictal discharges were localized in 10 (53%). The 15 patients (79%) who had surgery underwent invasive monitoring using stereotactic implanted depth electrodes (SEEG), with positioning of the leads guided by the putative lesion seen on texture maps. In all, SEEG demonstrated a very active inter-ictal activity and focal changes at seizure onset in the electrodes targeted at the lesion. According to the histopathological grading [60], 7 had FCD type IIa and 8 FCD type IIb. Mean post-operative follow-up was 21.1 ± 8.0 months. Ten patients (67%) became seizure free (Engel's class Ia) [132],

three had rare disabling seizures (class II), and two with lesions encroaching eloquent areas had worthwhile improvement (class III) as lesionectomy was incomplete. Three patients await surgery and one postponed it. Demographic and clinical data of patients are detailed in the **TABLE 3.1;** the flow diagram **(Figure 3.1)** outlines the study design and results.

Table 3.1. Demographics and results of automatic classification in MRI-negative patients examined at 3.0 Tesla.

Nr	Age/ sex	Duration (yrs)	EEG inter-ictal/ictal	PET (FDG)	Automatic detection lesion/extra-lesional clusters	FCD histology	Engel (months)
1	26/F	24	R FCT/none	-	Yes / 1	-	-
2	33/F	25	Bil. F/none	-	-	IIa	Ia (33)
3	21/M	21	L CP/L FC	Normal	Yes / 3	IIa	Ia (15)
4	25/M	4	L FC/none	-	Yes / 0	-	-
5	24/F	20	Bil. FC/Bil. F	R F	Yes / 0	IIb	II (32)
6	26/F	18	L FCT/L FCT	-	Yes / 1	IIb	Ia (26)
7	22/F	5	Bil. F/none	L FT	Yes / 0	IIa	II (26)
8	29/F	27	L F/L FC	Normal	Yes / 0	IIb	Ia (24)
9	24/M	24	none/L FCT	Normal	Yes / 1	IIb	II (24)
10	48/M	18	none/Bil. F	R FP	-	IIa	Ia (25)
11	37/M	18	R F/R F	R F	-	IIb	Ia (31)
12	31/F	15	L T/L TP	LT	Yes / 0	-	-
13	34/M	18	Bil. FC/R FC	R T	Yes / 1	IIa	Ia (12)
14	25/F	13	R FCT/R F	R FT	Yes / 2	-	-
15	19/F	7	CzPz/CzPz	Normal	Yes / 0	IIa	Ia (10)
16	30/M	13	Bil. FT/R F	L T	Yes / 0	IIb	Ia (19)
17	34/M	27	Bil. F/Bil. F	L F	-	IIa	Ia (12)
18	28/M	25	Bil. CP/Bil. CP	-	-	IIb	III (18)
19	22/F	4	Bil. FT/L FCT	Normal	Yes / 3	IIb	III (10)

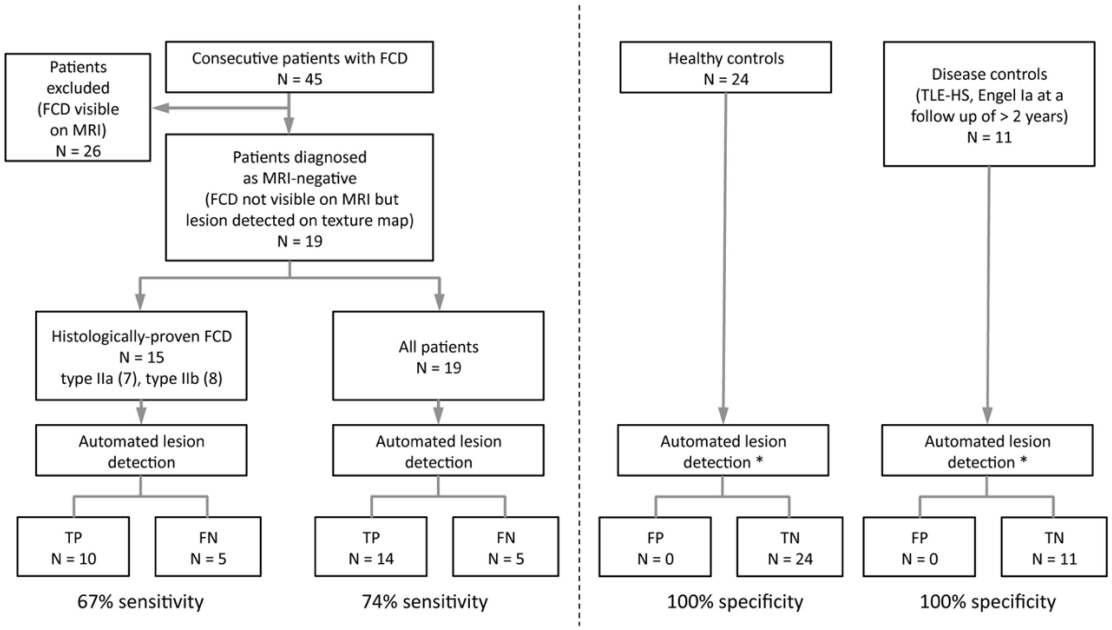

Figure 3.1. Flow diagram of study design and results. Abbreviations – FCD: focal cortical dysplasia; TLE-HS: temporal lobe epilepsy with histologically proven hippocampal sclerosis; Engel Ia: completely seizure-free in Engel's classification; FN: false negatives; FP: false positives; TN: true negatives; TP: true positives. *: classifier trained on 3.0 Tesla MRI of patients with histologically-proven FCD.

To assess the specificity of our algorithm, we examined 24 healthy controls (13 males; mean ± SD age 27 ± 4 years), and disease controls consisting of 11 patients with temporal lobe epilepsy (TLE) and hippocampal sclerosis (6 males; mean ± SD age 35 ± 11 years) who had undergone a selective amygdala-hippocampectomy and were completely seizure-free (*i.e.*, Engel Ia, mean ± SD follow up of 45 ± 8.4 months). Age and gender did not differ among groups ($t<1.5$. $p>0.1$).

Standard protocol approvals, registrations, and patient consent

The Ethics Committee of the MNI approved the study and written informed consent was obtained from all participants.

MRI acquisition and image preparation

The 1.5 Tesla MRI protocol has been described in details elsewhere [99]. The 3.0 Tesla images were acquired on a Siemens Trio Tim scanner using a 32-channels phased-array head coil. The protocol included a 3D magnetization-prepared rapid-acquisition gradient echo (MPRAGE) sequence providing isotropic voxels of 1x1x1 mm^3 (TR = 2300 ms, TE = 2.98 ms, flip angle = 7^o), axial proton-density (PD) and T_2-weighted images (voxel size = 0.4x0.4x3mm, TR = 2300, 11000 ms, TE = 20, 81 ms), coronal fluid attenuation inversion recovery (FLAIR, voxel size = 1x1x3 mm, TR = 9000 ms, TE = 80 ms), and coronal T_2-weighted images (voxel size = 0.5x0.5x5 mm, TR = 7000 ms, TE = 79 ms). Pre-processing involved automated correction of all images for intensity non-uniformity and intensity standardization [133], linear registration into standardized stereotaxic space [92], and automatic classification of T1-weighted images into white matter (WM), grey matter (GM), and cerebrospinal fluid (CSF) [134].

Cortical surface construction and FCD feature extraction

We applied the Constrained Laplacian Anatomic Segmentation using Proximity algorithm [90] on preprocessed T1-weighted images to generate a model of the GM-WM and GM-CSF surfaces with 40,962 vertices per hemisphere. This algorithm iteratively warps a surface mesh to fit the GM-WM boundary in the segmented image. The outer surface is then estimated by expanding the inner surface along a Laplacian map between GM-WM and GM-CSF boundaries. During this step, partial volume information is used to preserve the morphology of the GM-CSF boundary. The

expansion proceeds at a uniform rate proportional to local thickness and is governed by topological constraints. Extracted surfaces were non-linearly aligned to the surface template using a 2D registration procedure based on patterns of cortical folding that improves inter-individual correspondence [96]. The accuracy of surface extraction was verified by visual inspection prior to further analysis. We calculated at each vertex of the cortical surface the following morphological and intensity-based features. To avoid data interpolation related to registration, features were computed after surfaces were warped back into each individual's native space.

a) Morphological features

- C*ortical thickness.* We measured thickness as the distance between corresponding vertices on the GM-WM and GM-CSF surfaces [90].
- *Sulcal depth.* We have shown that small FCD lesions are often located at the bottom of a deep sulcus [99]. To calculate sulcal depth across the entire cortex, we first overlaid a brain hull model on the cortical manifold to detect vertices on the gyral crowns, which were initialized with a depth of zero. The depth of vertices located within sulci was then computed using the geodesic distance from gyral crown vertices [135].
- *Curvature.* By disrupting the mechanical properties of the cortical mantle, FCD may cause local curvature change [99]. We obtained the absolute mean curvature by estimating the area-minimizing flow that defines the deviation from the cortical surface to a sphere.

b) Intensity-based features

- *Relative intensity.* We used a modified version of our previous index of relative intensity (RI) [136] as: $RI(x) = 100 \times I(x) - GM_{peak}) / (B - GM_{peak})$, where $I(x)$ is the intensity at voxel x, GM_{peak}, the intensity of GM peak obtained from the whole-brain histogram, and B the intensity at the boundary between GM and WM. For surface-based sampling of RI, we constructed three equidistant intra-cortical surfaces by placing uniformly spaced vertices

between linked vertices of inner (GM-WM) and outer (GM-CSF) surfaces. The RI was then interpolated at each vertex of these surfaces and averaged.

- *Gradient.* To model blurring at the GM-WM interface, we applied a gradient operator that measured intensity differences 0.5 mm above and below the GM-WM interface along the surface normal vector.

Classifier design

Classification was performed using Fishers' linear discriminant analysis (LDA), an algorithm that automatically finds the optimal weights for a linear combination of features to achieve maximal separation between classes [137]. Prior to classification, features were smoothed using a 5mm full-width-at-half-maximum Gaussian surface kernel and normalized with respect to healthy controls' distribution through a z-transform. FCD lesions were segmented manually on MRI by an expert (D.S.), projected onto cortical surfaces, and blurred with a kernel of the same size. We trained and cross-validated the classifier using a-leave-one-out strategy, by which a patient is classified based on data of all patients other than that patient. This procedure allows an unbiased assessment of lesion detection performance for previously unseen FCD cases.

The classification steps are detailed in the **Figure 3.2**. The classifier was trained on patients' multivariate set of features sampled from all lesional and randomly selected non-lesional vertices, balancing their number in both classes. It generated vertex-wise probability maps for each individual to test (*i.e.*, patients and controls). On these maps, a cluster was defined as a collection of vertices that form 6-connected neighbours on the triangulated cortical surface. Within each cluster, we assessed the overall load of anomalies by computing the Mahalanobis' distance (a multivariate z-transform between each patient's feature vector and the corresponding distribution in controls).

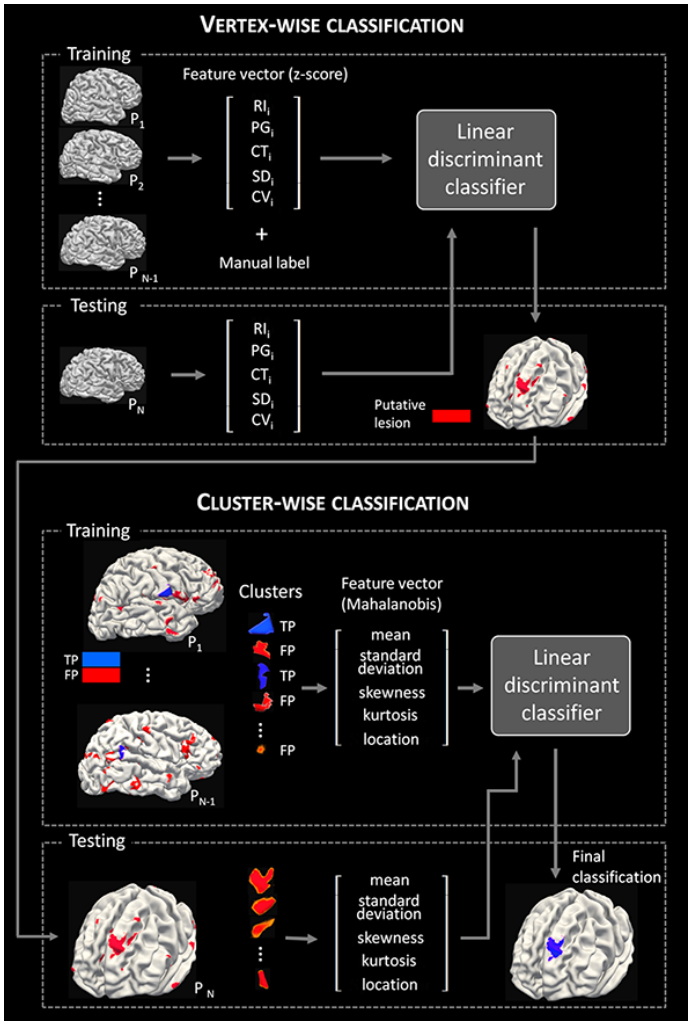

Figure 3.2. Construction of the two-step linear discriminant algorithm for FCD detection. *Vertex-wise classification*. For each patient (P), morphological and textural features are calculated at each vertex (*i*) of the cortical surface and z-scored w.r.t controls. For training, features are vectorized and fed to the classifier. To test a new, unseen case, the classifier generates a probability map of putative lesional vertices. *Cluster-wise classification*. Separates lesional (true positives; TP) from non-lesional (false positives; FP) vertices using statistical moments (mean, standard deviation, skewness, kurtosis, spatial location) of the multivariate feature z-scores (Mahalanobis). Classifiers were validated through a leave-one-out strategy, by which an individual is classified based on the training data of all other patients, allowing unbiased assessment of performance for previous unseen cases. *Abbreviation*: RI (relative intensity), PG (perpendicular gradient), CT (cortical thickness), SD (sulcal depth), CV (curvature)

For the set of vertices displaying the highest distance, we computed statistical moments (*i.e.*, mean, asymmetry, SD, skewness, and kurtosis representing the shape of the distribution of each feature) and spatial location (as determined by anatomical parcellation [138] and 3D coordinates). We fed these values to a second classifier and generated probability maps. For both classification schemes, we set the threshold of probability maps at the highest detection and lowest false positive rates.

Evaluation of classification accuracy

Performance of the classifier was assessed with regards to manual lesion labels. Sensitivity was defined as the proportion of patients in whom a detected cluster correctly co-localized with the manual lesion label. Specificity was calculated as the proportion of healthy or disease controls in whom no FCD lesion cluster was falsely identified.

Cross-dataset classification

We also evaluated the performance of our classifier trained on 3.0 Tesla data on a different dataset acquired at 1.5 Tesla including 14 patients (7 males, mean ± SD age 28 ± 11 years) with histologically-proven FCD (4 Type IIa and 10 Type IIb) and 20 age- and sex-matched healthy controls (8 males, mean ± SD age 27 ± 5 years). As for the 3.0 Tesla dataset, lesions had been overlooked on the initial radiological assessment and subsequently recognized through expert evaluation of texture maps.

3.4 Results

For the vertex-wise classification, the threshold of the posterior probability providing the best trade-off rate between true positives and false positives was 0.90. At this threshold, the classifier detected all but one lesion (18/19 = 95%); nevertheless, there was still a high proportion of false positives (mean ± SD clusters: patients = 32 ± 17; controls = 27 ± 16). In the subsequent cluster-wise classification (threshold of 0.90), no lesional clusters were identified in healthy subjects nor the disease control TLE group, resulting in 100% specificity. The LDA assigned the highest normalized weights (*i.e.*, more than 10% of total weighting) as follows; vertex-wise classification was mainly driven by perpendicular gradient (42%), followed by cortical thickness (41%), and sulcal depth (14%). Cluster-wise classification was largely based on perpendicular gradient (48%), followed by sulcal depth (13%), and cortical thickness (11%).

In FCD patients, the detected clusters co-localized with the manual lesion in 14/19, yielding a sensitivity of 74%. In 50% of them (7/14), the cluster corresponded to the FCD lesion (**Figure 3.3**). In the remaining 7 patients, besides the cluster co-localizing with the manual label, a median of one extra-lesional cluster was found (range = 1-3); in all but one patient, the extra-lesional clusters had the smallest size or the lowest multivariate z-score, the most abnormal feature being increased sulcal depth (**Figure 3.4**).

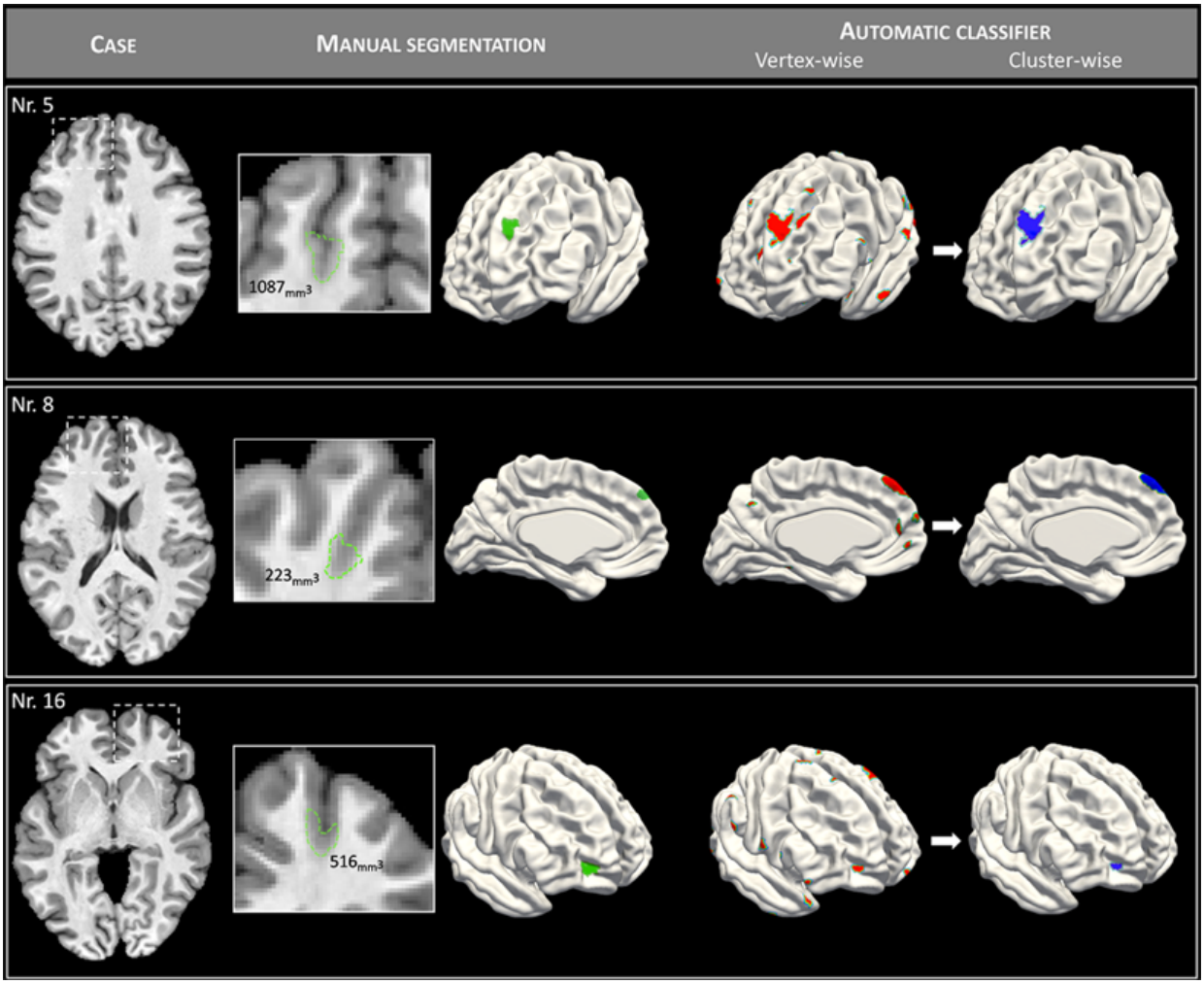

Figure 3.3. Examples of automated FCD type II detection. The axial T1-weighted MRI sections show the region containing the FCD (dashed square). The magnified panel displays the manually segmented FCD label (dotted green line) and its volume; the label is projected onto the surface template. In these three examples, the vertex-wise classification identified several putative lesions (red), whereas the subsequent cluster-wise classification discarded all false positives except the cluster co-localizing with the manual label (blue). The case number refers to that listed in the Table.

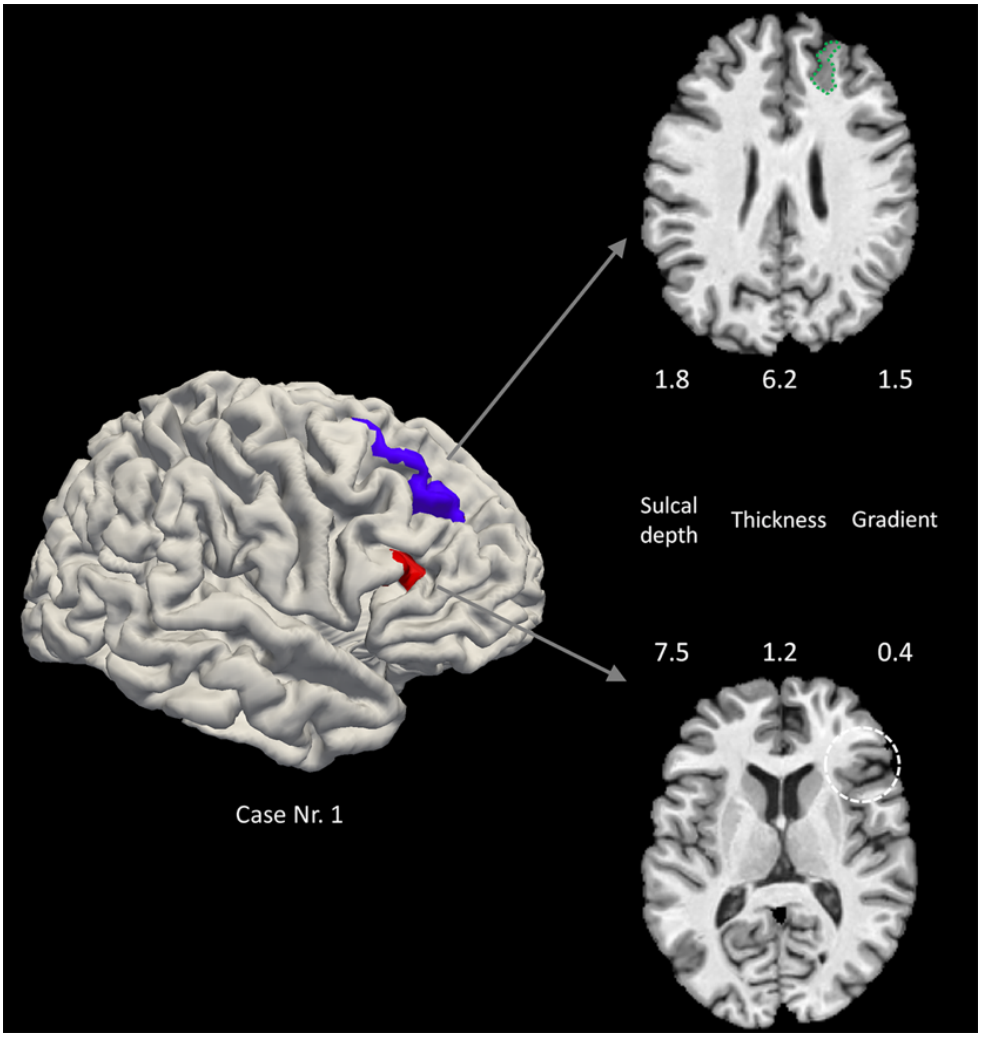

Figure 3.4. Extra-lesional findings. Results of the automated classification are projected onto the patient's cortical surface (case Nr.1, see Table for details). Z-scores of sulcal depth, thickness, and gradient for the lesional (blue) and extra-lesional (red) clusters are indicated. While the lesional cluster co-localizing with the manually segmented FCD label (dotted green line on axial T1-weighted MRI) exhibits abnormalities evenly distributed across the different features, the extra-lesional cluster is mainly characterized by increased sulcal depth. Visual MRI inspection in this region (dashed white circle, frontal operculum) does not reveal any obvious anomaly besides altered sulcal arrangement.

Extra-lesional clusters were found in frontal or central areas. They were located in the same lobe as the primary lesion in 2 patients; in 3 of the remaining 5 they were in the contralateral hemisphere, bilateral in 2. Among these 7 patients, 5 were operated at the primary lesion site; extra-lesional clusters were not resected. Three patients (60%) became completely seizure free (Engel class Ia), one had Class II outcome, while incomplete resection of the primary lesion was likely responsible of the unsatisfactory result (Engel class III) in the remaining one.

Repeating the analysis in the 15 patients with histologically-proven FCD, the classifier performance was virtually identical as in the overall group of 19 with 10/15 lesions detected (67% sensitivity, 100% specificity against healthy and disease controls, median of 1 extra-lesional cluster; **Table 3.2**).

TABLE 3.2. Individual results in the patients with histologically-proven FCD.

Nr	Age/ sex	Duration (yrs)	EEG inter-ictal/ictal	PET (FDG)	detection lesion/extra-clusters	FCD histology	Engel (months)
2	33/F	25	Bil. F/none	-	-	IIa	Ia (33)
3	21/M	21	L CP/L FC	Normal	-	IIa	Ia (15)
5	24/F	20	Bil. FC/Bil. F	R F	Yes / 0	IIb	II (32)
6	26/F	18	L FCT/L FCT	-	Yes / 1	IIb	Ia (26)
7	22/F	5	Bil. F/none	L FT	Yes / 0	IIa	II (26)
8	29/F	27	L F/L FC	Normal	Yes / 0	IIb	Ia (24)
9	24/M	24	none/L FCT	Normal	Yes / 0	IIb	II (24)
10	48/M	18	none/Bil. F	R FP	-	IIa	Ia (25)
11	37/M	18	R F/R F	R F	-	IIb	Ia (31)
13	34/M	18	Bil. FC/R FC	R T	Yes / 1	IIa	Ia (12)
15	19/F	7	CzPz/CzPz	Normal	Yes / 2	IIa	Ia (10)
16	30/M	13	Bil. FT/R F	L T	Yes / 0	IIb	Ia (19)
17	34/M	27	Bil. F/Bil. F	L F	-	IIa	Ia (12)
18	28/M	25	Bil. CP/Bil. CP	-	Yes / 3	IIb	III (18)
19	22/F	4	Bil. FT/L FCT	Normal	Yes / 3	IIb	III (10)

Lesion classification in the 1.5 Tesla dataset provided virtually identical results compared to the 3.0 Tesla cohort. In the vertex-wise classification, the classifier achieved high sensitivity (13/14 = 93%) with a high proportion of false positives (mean ± SD clusters: patients = 38 ± 18; controls = 17 ± 17). Subsequent cluster-wise classification eliminated false positive clusters in both patients and controls, while maintaining a high lesion detection rate, with 71% sensitivity (lesion detected in 10/14 patients) and 95% specificity (three false positive clusters in a single control; **Table 3.3**).

Table 3.3. Demographics and individual results of patients examined at 1.5 Tesla.

Nr	Age/ sex	Duration (yrs)	EEG inter-ictal/ictal	Automatic detection lesion/extra-lesional clusters	FCD histology	Engel (months)
1	30/F	18	R FC / R FC	Yes / 0	IIa	Ia (67)
2	17/M	12	L FC / L FC	Yes / 2	IIb	II (62)
3	25/F	21	None / none	Yes / 0	IIb	II (42)
4	43/F	23	L F / none	-	IIa	Ia (52)
5	16/M	9	FzCz / none	Yes / 0	IIb	II (36)
6	26/M	22	L FC / CzPz	Yes / 0	IIb	Ia (60)
7	32/F	28	L FC / none	-	IIb	III (32)
8	18/F	14	R FC / R FC	Yes / 0	IIa	Ia (40)
9	36/M	30	None / Bil. F	Yes / 0	IIb	Ia (70)
10	16/M	12	R F / R F	Yes / 3	IIa	Ia (70)
11	22/M	21	R CP / R CP	-	IIb	Ia (61)
12	50/F	41	R FC / none	Yes / 5	IIb	Ia (69)
13	34/M	26	Bil. CP / Bil. CP	Yes / 0	IIb	II (48)
14	16/F	3	None / none	-	IIb	Ia (33)

3.5 Discussion

MRI has undoubtedly transformed the management of drug-resistant epilepsy by allowing the detection of structural lesions associated with the epileptogenic zone. Yet, despite technical improvements in hardware and sequences, MRI inspection is often unremarkable, as shown by our patients who were considered MRI-negative on both 1.5 and 3.0 Tesla scanners. Re-assessment guided by texture analysis, nevertheless, identified the lesion in all. Notably, although texture maps model FCD characteristics in a quantitative fashion, they are evaluated visually, making the distinction between lesional areas and false positives challenging. Moreover, integrating the diverse and complex information embedded in the various maps requires expertise that few centers have developed so far. Another source of difficulty arise from the paucity or lack of localizing clinical semiology and surface EEG findings to direct the search for FCD.

Our previous automatic FCD detection on 1.5 Tesla MRI relied on voxel-based texture analysis combined with a Bayesian classifier [81]. The algorithm was validated with mid- to large-sized lesions visible on routine radiological inspection. Nevertheless, classification failed in up to 20% of cases. Such performance is unsatisfactory given current referral patterns, with an increasing number of patients with extra-temporal epilepsy and non-diagnostic MRI, even at 3.0 Tesla. In these patients, lesions are subtle, with morphological characteristics that may differ only slightly from normal tissue. Voxel-based methods do not optimally characterize morphology as they neglect anatomical relationships across the folded cortex; while relatively efficient in detecting obvious lesions, they amplify unwanted partial volume effects, leading to a loss of signal from confined or subtle abnormalities [139]. Our current algorithm relies on surface-based multivariate pattern recognition that statistically combines morphology and intensity taking advantage of their

covariance, thus unveiling sub-threshold tissue properties not readily identified on a single modality. For automated lesion detection, we chose a linear discriminant model, a supervised technique that is mathematically robust and simple to interpret [140]. The most significant contribution of machine learning to clinical practice is that it provides an automatic and objective way to extend knowledge obtained from training data to unknown (*i.e.*, first seen) cases. Compared to previous work, we explicitly circumvented several sources of bias. Firstly, we cross-validated our findings using a leave-one-out strategy and obtained a sensitivity of 74% after post-hoc removal of false positives, half of patients presenting with a single lesional cluster. Secondly, when applying our classifier trained on 3.0 Tesla images to an independent dataset of patients with histologically-proven FCD acquired at 1.5 Tesla, we maintained high sensitivity. Given that all subjects were initially diagnosed as MRI-negative, this fully automated approach offered a substantial gain in sensitivity over standard radiological assessment. Cross-dataset classification results support the generalizability of our method to MRI-negative FCD across different cohorts, scanners, and field strengths.

In addition to high sensitivity, another equally important result is that, after removal of false positives, no lesional vertices were identified in healthy or disease control subjects. Such high specificity indicates that our classifier correctly ignored healthy tissue in normal controls, and disregarded FCD-unrelated pathology in the disease control group. These findings are especially relevant as in 50% of patients the classifier identified 1-3 extra-lesional clusters (median of 1). Extra-lesional clusters were not resected; thus, no pathology was available. Retrospective analysis revealed that, although these clusters presented with features similar to those of the primary FCD, they were smaller and their contribution to the multivariate distribution was somewhat different.

While cortical thickness had the highest z-score within the primary lesion, sulcal depth typified extra-lesional clusters. Additionally, there were no EEG anomalies associated with the latter; no clinical or histopathological characteristics differentiated these patients from those with a single cluster. Yet, the absence of false positives in healthy and disease controls combined with reports of diffuse [141] or multifocal FCD [18], suggests that these clusters may indeed indicate abnormal, not necessarily epileptogenic regions that are otherwise undetectable *via* conventional means. Sulcal abnormalities in cortical malformations have been described in the proximity of MRI-visible lesions [99], but also at distance [129, 142, 143], and are thought to result from disturbed neuronal connectivity and WM organization [144, 145]. Alternatively, these regions may present with variations in cyto- and myelo-architecture, and decreased neuronal density [146] leading to changes in micromechanical properties [147] resulting in local weakness within the developing neocortex.

The absence of a visible lesion is one of the greatest challenges in epilepsy surgery and has lead to an increase in invasive EEG studies. Yet, without informed, image-guided implantation, even with widespread coverage, sampling errors may occur in up to 40% of cases; consequently the target cannot be defined and the outcome of surgery, if considered, is poorer [148]. To optimize hypothesis formulation and to improve the patient's safety while minimizing costs of the presurgical diagnostic procedures, future efforts should aim at creating independent non-invasive techniques that take into account all facets of the epileptogenic process.

CHAPTER 4

WHOLE-BRAIN STRUCTURAL ALTERATIONS IN DYSPLASIA-RELATED FRONTAL LOBE EPILEPSY

Preface

In the previous chapter, we observed that 50% our FCD patients presented with extra-lesional clusters. As our algorithm demonstrated perfect specificity in both healthy and disease controls, we interpreted these clusters as non-primary cortical malformations that would otherwise go undetected on conventional imaging. The consistency of these finding, however, remained unclear given that patients presented with lesions located in various brain regions and thus presenting with diverse epileptic syndromes.

Here, the purpose of this study was to examine whole-brain MRI morphology in dysplasia-related frontal lobe epilepsy. It is of note that cohorts did not differ in demographics, disease duration, and number of generalized seizures, but diverged only with respect to the FCD type.

* * *

4.1 Abstracts

We assessed whole-brain anomalies in frontal lobe epilepsy patients with histologically-verified focal cortical dysplasia (FCD) and evaluated the utility of group-level patterns for individualized diagnosis and prognosis. We compared MRI-based cortical thickness and folding complexity between two frontal lobe epilepsy cohorts with histologically-verified FCD (13 Type-I; 28 Type-II) and closely-matched 41 controls. Pattern learning algorithms evaluated the utility of group-level findings to predict histological FCD subtype, the side of the seizure focus, and post-surgical seizure outcome in single individuals. Relative to controls, FCD Type-I displayed multilobar cortical thinning that was most marked in ipsilateral frontal cortices. Conversely, Type-II showed thickening in temporal and post-central cortices. Cortical folding also diverged, with increased complexity in prefrontal cortices in Type-I and decreases in Type-II. Group-level findings successfully guided automated FCD subtype classification (Type-I: 100%; Type-II: 96%), seizure focus lateralization (Type-I: 92%; Type-II: 86%), and outcome prediction (Type-I: 92%; Type-II: 82%). FCD subtypes relate to diverse whole-brain structural phenotypes. While cortical thickening in Type-II may indicate delayed pruning, a thin cortex in Type-I likely results from combined effects of seizure excitotoxicity and the primary malformation. Group-level patterns have a high translational value in guiding individualized diagnostics.

This work was published in:
Hong SJ, Bernhardt BC, Schrader D, Bernasconi N, Bernasconi A. *Whole-brain MRI phenotyping in dysplasia-related frontal lobe epilepsy*. Neurology 2016. 86(7):643-50

4.2 Introduction

Focal cortical dysplasia (FCD) is a frequent epileptogenic developmental malformation in children and adults undergoing epilepsy surgery [3]. While FCD Type-II combining cytological anomalies with varying degrees of dyslamination [60] is generally associated with obvious morphology and signal changes on MRI [7], the imaging signature of FCD Type-I, characterized by subtle cortical thinning and dyslamination [60], remains elusive.

Because of the crucial role of MRI in defining the surgical target, imaging studies in FCD have been primarily dedicated to lesion detection in single patients [149]. Whole-brain cohort-specific structural brain anomalies remain largely unknown [150]. In other epilepsy syndromes, group-based designs have provided new insights by unveiling clinically relevant characteristics and helped formulating hypotheses about disease mechanisms [151, 152]. Here, we aimed at comparing whole-brain morphology between frontal lobe epilepsy cohorts with histologically-verified FCD Type-I and II. Our approach was motivated by case reports indicating that FCD Type-II may present with histological [18] and MRI anomalies [16, 153] in remote cortices resembling those found in the primary lesion and that Type-I may be associated with subtle multi-lobar hypoplasia on MRI [67].

We hypothesized widespread, yet diverging patterns of anomalies, with cortical thinning in FCD Type-I and thickening in Type-II. Our MRI phenotyping combined group- and individual-level analysis of cortical thickness and folding complexity, two established *in vivo* markers of brain morphology and development. We evaluated the clinical utility of group-level patterns to classify the histopathological FCD subtype, lateralize the seizure focus, and to predict post-surgical seizure outcome in individual patients using machine learning.

4.3 Methods

Subjects

From a database of patients hospitalized for pre-surgical workup of drug-resistant extratemporal epilepsy at the Montreal Neurological Institute (MNI) and Hospital who underwent video-EEG telemetry and examined on a single scanner with an identical imaging protocol [99] (n=73), we selected those with frontal lobe epilepsy and histologically-verified FCD (Type-I, n=13; Type-II, n=28).

In patients with FCD Type-II, the lesion was seen either on conventional MRI (n=18) or became visible through texture analysis [80] (n=10). In the latter group, surgery was preceded by invasive monitoring using stereotactic implanted depth electrodes (SEEG), with positioning of the leads guided by the putative lesion seen on texture maps; in all, SEEG demonstrated a very active inter-ictal activity and focal changes at seizure onset in the electrodes targeting the lesion. Mean post-operative follow-up time was 4.9±3 years; eighteen patients became seizure free (Engel I) [132], 6 had rare disabling seizures (Engel II), and 4 with lesions encroaching eloquent areas had worthwhile improvement (class III) as lesionectomy was incomplete. In patients with FCD Type I, both preoperative visual MRI and image processing were unremarkable; surgery in these patients was preceded by SEEG. Implantations were guided by findings derived from video-EEG telemetry with scalp electrodes in all, with additional help from FDG-PET (n=9) and SPECT (n=7) data, and resulted in focal corticectomies in the supplementary motor area in 5 patients, prefrontal cortex in 4, lower central in 3 and orbitofrontal in one. Mean post-operative follow-up was 3.9±2 years; 3 patients became seizure-free (Engel I), 3 had rare disabling seizures (Engel II), 5 a worthwhile improvement (Engel III), and 2 no improvement (Engel IV).

Patient cohorts did not differ in age, disease duration, gender distribution, seizure focus lateralization, and number of generalized seizures ($p>0.15$). The control group consisted of 41 age-

and sex-matched healthy subjects. Demographic, clinical, and electrophysiological data are presented in the **Table 4.1**.

Table 4.1. Demographic and electro-clinical data.

	CONTROLS	FCD TYPE-I	FCD TYPE-II
Number of subjects	41	13	28
Male/Female	16/25	7/6	11/17
Age	31±11	29.2±8.7	29.1±10.4
Age at onset	-	12.2±6.4	6.7±4.2
Duration	-	17.1±10.2	22.1±11.8
Secondary GTCS	-	8 (62%)	17 (61%)
Seizure focus (R/L)		6/7	15/13

Age, age at seizure onset and duration of epilepsy presented as mean±SD in years; *Abbreviations*: GTCS=generalized tonic-clonic seizures; R/L=right/left

Standard protocol approvals, registrations, and patient consent

The Ethics Committee of the MNI approved the study and written informed consent was obtained from all participants.

MRI acquisition and image preparation

In all subjects, images were acquired on a 1.5 Tesla Gyroscan (Philips Medical Systems, Eindhoven, Netherlands) using a 3D T1-fast field echo sequence (TR=18 ms; TE=10 ms; flip angle=30˚; matrix size=256×256; FOV=256×256 mm^2; slice thickness=1 mm) providing isotropic voxel dimensions of 1×1×1 mm. MRI preprocessing included automated correction for intensity non-uniformity and intensity standardization, linear registration to the MNI152 template, and

classification into white matter (WM), gray matter (GM), and cerebrospinal fluid (CSF) [154]. We applied the Constrained Laplacian Anatomic Segmentation using Proximity (CLASP) algorithm [90] to generate a model of the inner (WM-GM) and outer (GM-CSF) surfaces with 40k surface points (or *vertices*) for each hemisphere. Extracted surfaces were non-linearly aligned to a surface template to improve inter-individual correspondence [96]. The accuracy of surface extractions was verified in all subjects prior to further analysis.

Surface-based morphometry

We generated cortical thickness and curvature maps using previously reported methodology [155, 156]. Cortical thickness was measured as the distance between corresponding vertices of inner and outer surfaces. To measure curvature, we generated a surface model running at mid-distance between the inner and outer surfaces. We subsequently applied a barycentric smoothing with three iterations to reduce high frequency noise in vertex positions [135]. Absolute mean curvature was calculated at each vertex to quantify changes in frequency and depth of sulcal and gyral folds, expressing local gyrification complexity. Structural metrics were blurred with a surface-based kernel of FWHM=20 mm that preserves cortical topology [154].

Statistical analysis

Statistical Analysis was performed using SurfStat for Matlab [157]. Patients were analyzed relative to the epileptogenic hemisphere; the symmetric template used for surface registration ensured an unbiased analysis when sorting hemispheres into ipsilateral/contralateral to the focus. Furthermore, we normalized thickness and curvature at each vertex using a z-transformation with respect to the corresponding distribution in controls; in other words, each patient's right/left feature was expressed as z-score with respect to right/left values in controls.

a) Mapping structural changes relative to controls

We assessed differences in cortical thickness and folding complexity between each patient group (i.e., FCD Type-I and Type-II) and controls using two-tailed Student's t-tests at each vertex. As curvature might be affected by variations of cortical thickness, we statistically adjusted this metric at every vertex by the corresponding thickness measure [158]. In FCD Type-II, to eliminate potential effect of the lesion on group comparisons, we performed an additional analysis, in which lesion labels obtained through expert manual segmentation (D.S.) were projected onto cortical surfaces and blurred with a 20 mm kernel, excluding cortical measures that fell within the blurred labels.

For individual analysis, we calculated proportions of patients with thickness/curvature measures beyond ±2SD from the mean of controls across the cortical surface [106]. In FCD Type-II, lesional labels were excluded. A leave-one-out approach calculated unbiased prevalence in controls.

b) Direct contrast between patient groups

Cortical thickness and curvature were directly compared between groups using vertex-wise two-sample t-tests.

c) Group differences in post-surgical outcome

We subdivided patients into seizure-free (Engel-I) and non-seizure-free (II-IV), and compared cortical markers between outcome classes.

d) Automatic classification of individual patients

We evaluated the yield of group-level findings to predict FCD subtypes, lateralize the seizure focus, and determine post-surgical outcome using a machine-learning approach with leave-one-out validation. Each hemisphere was subdivided into 500 equally-sized parcels [159]. The search space was confined to regions displaying group-level differences (FCD Type-I vs. Type-II for subtype prediction; FCDs vs. healthy controls for focus lateralization, and seizure-free vs. non-seizure-free for outcome prediction). Each parcel falling into a significant cluster was mirrored to both left and right hemispheres, as one cannot assume to know focus-laterality in a new patient. We extracted mean thickness and curvature z-scores from these parcels and fed them to a support vector machine (SVM) classifier that evaluated prediction performance based on single pairs of parcels. To optimize classification sensitivity, borrowing the concept of searchlight-based multivoxel pattern analysis [153], we evaluated combinations of single pairs of parcels (preselected from those achieving >80% accuracy) using a separate SVM. The optimal number of parcel pairs was empirically set to three.

e) Correction for multiple comparisons and assessment of classification accuracy

Group results were corrected using random field theory for non-isotropic images at a cluster-level [160]. We used the function SurfStatP.m, with a search space constrained to the neocortical mantle in both hemispheres. This controlled the family-wise error (FWE) probability to $p<0.05$. In all machine learning experiments, we used permutation tests to confirm whether the achieved accuracy exceeded chance-level (Bonferroni-corrected $p<0.05$).

4.4 Results

Group analysis (**Figure 4.1**)

a) Cortical thickness.

Compared to controls, FCD Type-I showed bilateral multilobar cortical thinning, with ipsilateral lateral frontal and mesial precentral changes (FWE-corrected p-value, $p_{FWE}<0.0001$; *Cohen's d*=0.78; 95% Confidence interval [CI]= -1.53 to -0.40). Atrophy was also present in ipsilateral insular, supramarginal, and temporal cortices ($p_{FWE}<0.02$; *Cohen's d*=0.72; 95% CI=-1.37 to -0.29). Comparing Type-II to controls revealed contralateral post-central and temporal thickening ($p_{FWE}<0.005$; *Cohen's d*=0.63; 95% CI=0.24 to 1.13), together with medial occipital thinning ($p_{FWE}<0.04$; *Cohen's d*=0.69; 95% CI=-1.07 to -0.28). Notably, at uncorrected thresholds, thickness increases were also present ipsilaterally; moreover, asymmetry analysis did not show inter-hemispheric differences in this cohort ($t<0.5$, $p>0.3$). Excluding lesional vertices from comparisons did not modify results. Finally, directly contrasting both patient cohorts confirmed frontal and cingulate atrophy in Type-I ($p_{FWE}<0.005$; *Cohen's d*=0.82; 95% CI=-1.66 to -0.34).

b) Cortical folding complexity.

Compared to controls, while FCD Type-I showed increased curvature in ipsilateral orbitofrontal cortices ($p_{FWE}<0.001$; *Cohen's d*=0.71; 95% CI=0.16 to 1.24), complexity in Type-II was decreased in bilateral frontopolar regions ($p_{FWE}<0.03$; *Cohen's d*=0.62; 95% CI=-1.06 to -0.23). The direct between-group contrast confirmed increased folding in ipsilateral orbitofrontal in Type-I with additional increases in frontopolar cortices ($p_{FWE}<0.01$; *Cohen's d*=0.84; 95% CI=0.17 to 1.38).

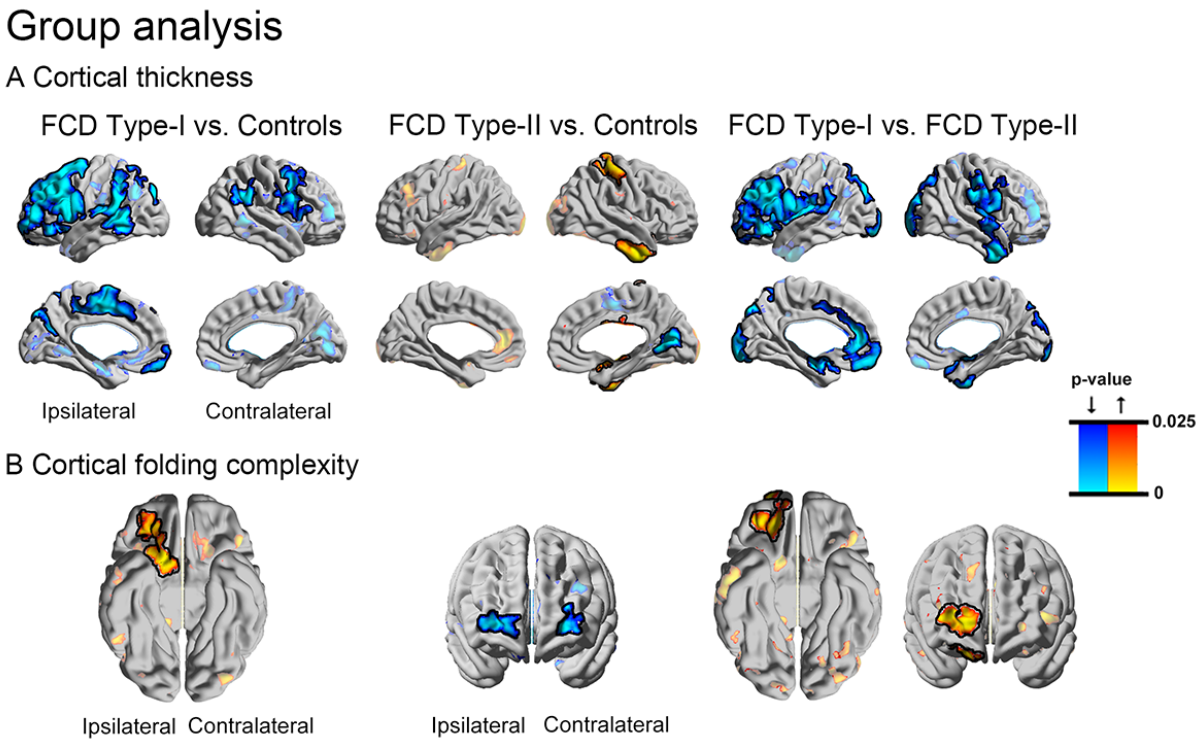

Figure 4.1. Group-level alterations in cortical thickness **(A)** and folding complexity **(B)** in patients with FCD. In A and B, the *left panels* show comparison between FCD Type-I and healthy controls; the *middle panels* between Type-II and controls; and the *right panels* show the direct contrast between the two FCD cohorts. *Increases/decreases* are shown in *red/blue*. Significant clusters, corrected for multiple comparisons using random field theory at $p_{FWE}<0.05$, are shown in solid colors and outlined in black; trends are shown in semi-transparent.

Individual analysis (**Figure 4.2**)

In both patient cohorts, individual analysis revealed a spatial distribution of highly prevalent anomalies resembling the group-level findings, with up to 55% showing marked morphological abnormalities (*i.e.,* more than 2SD beyond the mean of controls). Furthermore, prevalent anomalies were seen in lateral temporal cortices in FCD Type-I and medial frontal cortices in Type-II. In controls, on the other hand, prevalence for abnormal z-scores did not surpass more than 5% at any vertex.

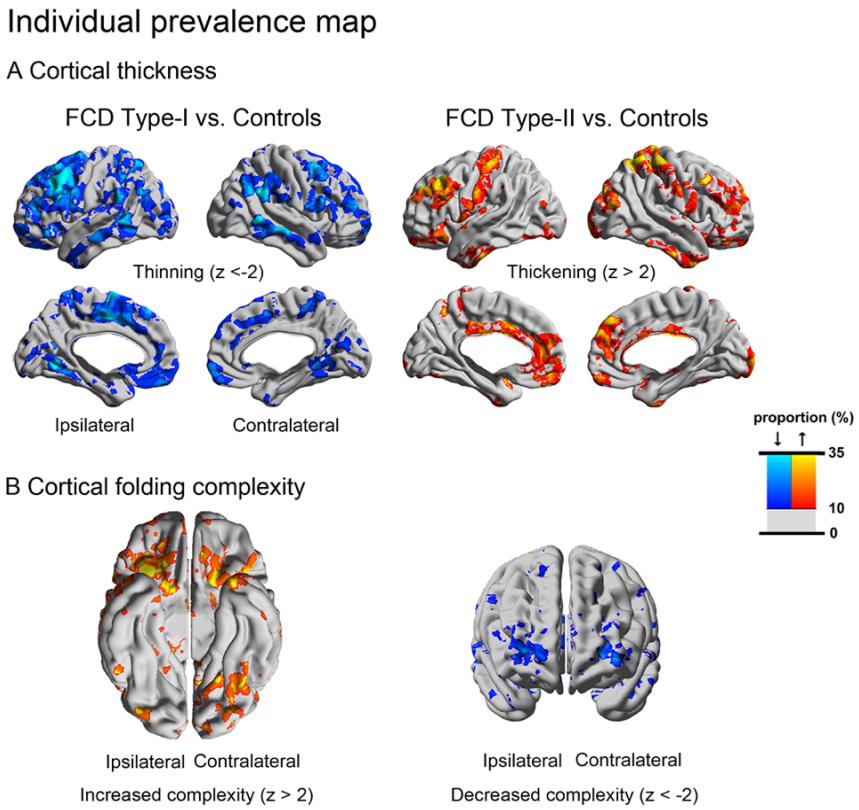

Figure 4.2. Individual analysis. At each vertex, the proportion of patients with a thickness (A) and complexity (B) z-score beyond ±2SD relative to controls is shown. Only fractions above 10% are displayed.

Duration-stratified subgroup analysis (**Figure 4.3**)

To explore the dichotomy between patient cohorts, we subdivided each with respect to its median duration (14 years in FCD Type-I, 21 years in Type-II) into short (FCD Type-I: n=7; FCD Type-II: n=14) and long (FCD Type-I: n=6; FCD Type-II: n=14), and compared them to controls. The difference in duration between FCD Type-I and Type-II was not significant, neither for the short (10.1±3.2 *vs*. 12.9±6.2; t=1.1, p>0.28) nor long-duration subgroups (25.2±9.4 *vs*. 31.4±8.1; t=1.4, p>0.15). On the other hand, as the short duration subgroups were younger than controls (22±5 *vs.* 31±11 years, p=0.001), we controlled for age in subsequent comparisons.

In FCD Type-I, both subgroups presented with diffuse and bilateral cortical thinning, with a somewhat more marked and extended distribution in ipsilateral frontal cortices in those with long disease duration. In Type-II, on the other hand, patients with short duration showed bilateral symmetric thickening in frontal, central, and temporal areas ($p_{FWE}<0.04$), while those with long duration presented with peri-central and temporo-occipital thinning ($p_{FWE}<0.04$). Results in Type-II remained unchanged after excluding lesional vertices. In a separate analysis, linearly modeling vertex-wise duration effects revealed progressive cortical thinning in ipsilateral middle frontal and contralateral orbitofrontal cortices in FCD Type-I. A similar direction and extent of progressive thinning was observed in Type-II; interaction analysis did not show differences in duration effects between both patient cohorts. These findings suggest that disease progression occurs in both FCD subtypes, though with differential timelines (*i.e.,* FCD Type-II: thick cortex in patients with short disease duration, thinner cortex with longer duration; FCD Type-I: thin cortex in patients with short duration, very thin cortex in those with longer duration).

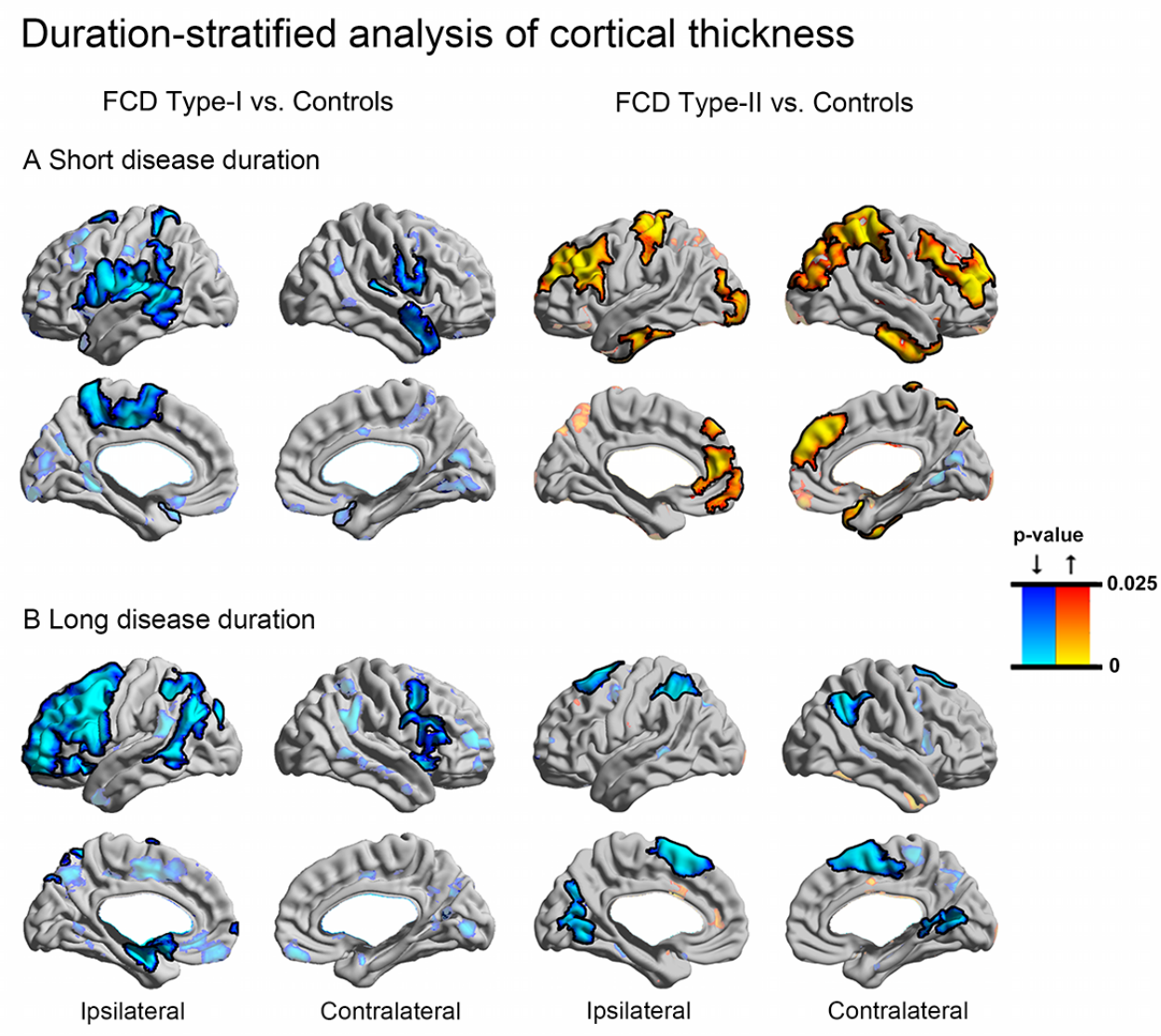

Figure 4.3. Duration-stratified cortical thickness group analysis. Each patient cohort was split into short **(A)** and long **(B)** duration subgroups according to its respective median (FCD Type-I: 14 years; FCD Type-II: 21 years), and compared to controls. Cortical thickness increases/decreases are shown in red/blue. Significant clusters, corrected for multiple comparisons using random field theory at FWE<0.05, are shown in solid colors and outlined in black; trends are shown in semi-transparence.

Analysis of post-surgical outcome (**Figure 4.4**)

In FCD Type-I, patients with residual seizures had more marked cortical thinning compared to seizure-free patients in a large region within the ipsilateral medial frontal cortex ($p_{FWE}<0.05$). In FCD Type-II, on the other hand, non seizure-free patients presented with thicker contralateral mid/posterior cingulate, parietal, and temporopolar cortices compared to those who achieved seizure-freedom ($p_{FWE}<0.05$). Folding complexity did not relate to outcome in either cohort.

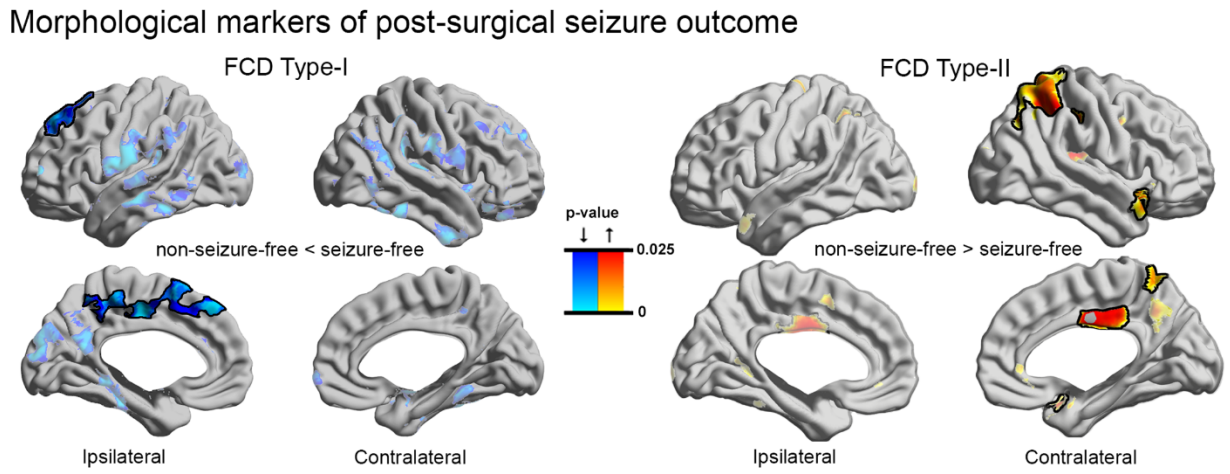

Figure 4.4. Morphological markers of post-surgical seizure outcome. Cortical thickness comparison between seizure-free (Engel-I) and non-seizure-free patients (II-IV). Please see *Figure 1* for details on statistical procedures. Given the small number of seizure-free patients (n=3) in Type-I, findings were cross-validated using non-parametric permutation tests, both for group comparison and FWE-correction.

Automated patient classification **(Figure 4.5)**

The SVM predicting the histological subtype achieved 98% accuracy (13/13=100% in FCD Type-I; 27/28=96% in FCD Type-II), with frontopolar and ventrolateral prefrontal regions contributing to optimal classification. Automated lateralization of the epileptic focus was also highly accurate (12/13=92% in Type-I; 24/28=86% in Type-II), with lateral frontal, temporal, and frontobasal features driving performance for Type-I, and post-central, lateral temporal, and frontopolar regions for Type-II. Finally, we could predict outcome in 92% (12/13) of patients with Type-I and 82% (23/28) with Type-II; predictive parcels were situated in superior frontal and parietal regions in Type-I, and in the mid/posterior cingulate cortex in Type-II. Permutation tests with 1000 iterations confirmed that achieved accuracies exceeded chance-level (Bonferroni-corrected $p<0.05$).

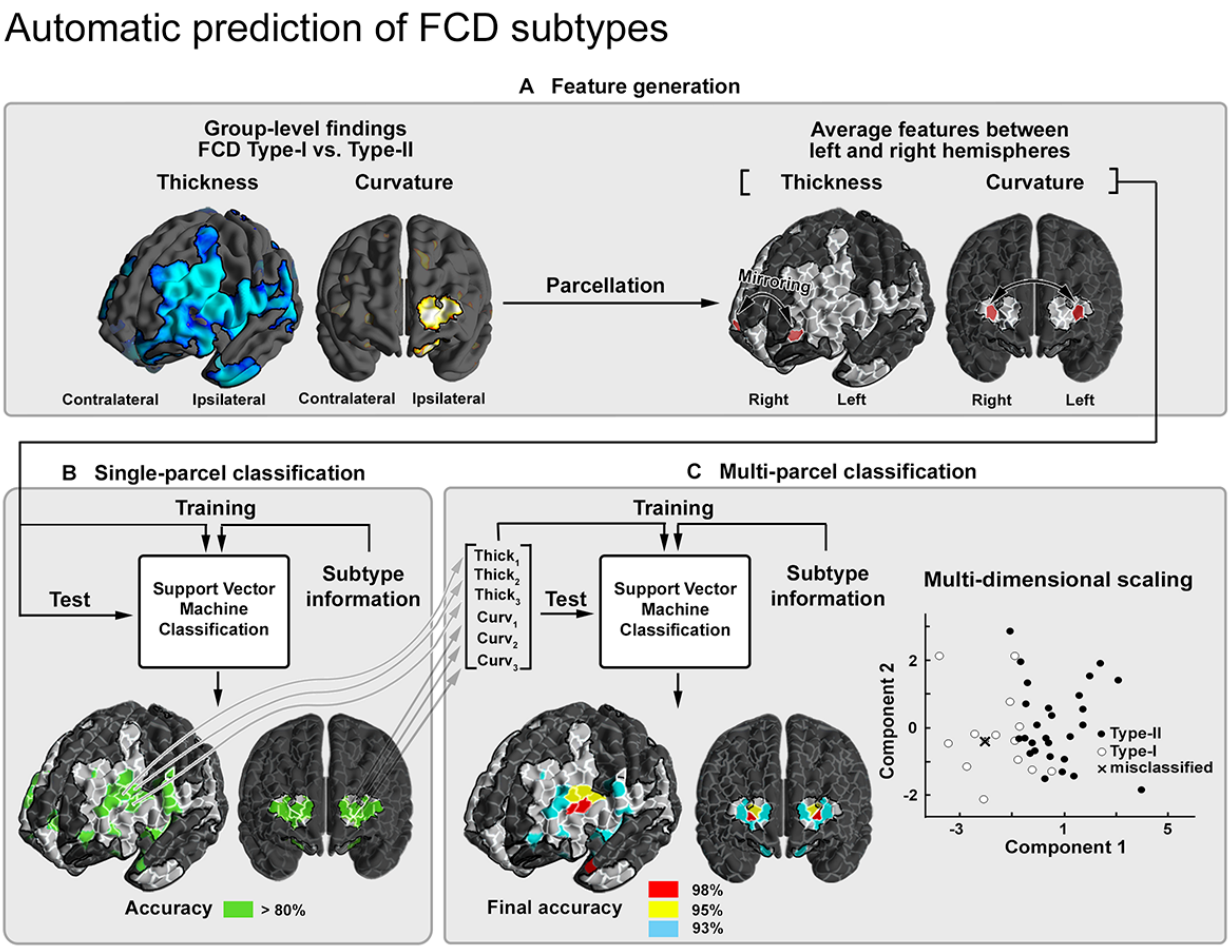

Figure 4.5. Machine-learning framework applied to FCD subtype prediction. A) *Feature generation*. Each hemisphere was subdivided into 500 equally-sized parcels. The search space was confined to significant clusters of group-level differences (*i.e.*, FCD Type-I *vs.* Type-II). After mirroring each parcel to both left and right hemispheres, we generated a feature vector by extracting mean thickness and curvature z-scores. **B)** *Single-parcel classification.* Features obtained in A were fed to a support vector machine classifier, which evaluated subtype prediction performance at each pairs of parcels. **C)** *Multi-parcel classification.* To optimize sensitivity, among parcels achieving >80% accuracy in B (color-coded in green), combinations of *k* pairs of parcels (optimal *k* empirically set at 3) were fed to a separate classifier. Multi-dimensional scaling allows reducing dimensionality to 2D while preserving inter-feature distances. Misclassified cases are highlighted with an 'x'. Steps A-C are carried out in a leave-one-out framework that allows determining prediction accuracy for previously unseen cases.

4.5 Discussion

We examined whole-brain MRI morphology in dysplasia-related frontal lobe epilepsy. Cohorts did not differ in demographics, disease duration, and number of generalized seizures, but diverged with respect to the FCD type, lesion visibility, and post-surgical outcome. In FCD Type-I, surface-based analysis unveiled widespread atrophy, a finding cross-validated by direct comparison to those with Type-II lesions. Moreover, individual analysis showed that group-level patterns were highly prevalent, dispelling possible concerns that outliers could have driven findings.

Widespread neocortical atrophy, often observed in drug-resistant temporal lobe epilepsy [161] and idiopathic generalized epilepsy [162], is thought to reflect combined effects of neuronal disconnection and seizure-related damage. Sustained seizure activity may lead to cell loss in both seizure-generating regions and areas of spread [163], particularly through upregulation of glutamate [164]. While this scenario may explain cortical thinning in our patients with Type-I FCD, it is seemingly at odds with findings in those with Type-II lesions, who showed increased thickness in several cortices. This paradox was further amplified when stratifying patients according to disease duration: close to the onset, Type-I FCD patients displayed diffuse bilateral cortical atrophy, while those with Type-II lesions presented with marked and fairly extensive cortical thickening, even when controlling for age and after excluding the lesion label.

Diverging morphometric patterns, particularly at early disease stages, may point to distinct mechanisms and timing underlying the anomalous cortical development in these cohorts. Typical brain growth entails a series of complex and overlapping steps, including synaptogenesis with elaboration of dendrites, which continue into early childhood [165]. In this context, pruning, a self-regulatory process starting in late gestation (which eliminates redundant axons, dendrites, and

synapses, as well as neurons) plays a pivotal role in shaping cortical network organization until late adolescence, sparing only the most efficient connectivity configurations [166]. Notably, in FCD Type-II, aberrant synaptogenesis of dysmorphic neurons and failure of oligodendroglial differentiation result in erroneous axonal processes and hypomyelination [124]. In light of our observations, one may postulate that the primary lesion and mutually connected cortices show delayed pruning that manifest as gray matter excess. Moreover, according to models of structural covariance and maturational coupling of brain networks, regions belonging to the same network show correlated growth due to exchange of trophic factors and common molecular signaling pathways [167]. Conceivably, developing cortices sharing links with the lesion may be influenced in similar ways. A post-hoc analysis indeed supported a selective thickening of contralateral neocortices homotopic to the primary FCD Type-II in patients with short disease duration ($p<0.05$ relative to controls), while thickness of non-homotopic contralateral vertices was not increased.

Diffuse cortical thinning in FCD Type-I warrants several considerations. Firstly, in light of the recent histopathological findings showing a tendency for reduced cortical thickness in FCD Type-I [124], primary frontal cortical thinning observed in our patients may reflect, in part, the primary lesion. This hypothesis is justified by our inclusion criteria, as we restricted the assessment to patients with frontal lobe epilepsy only. Secondly, in young children with psychomotor handicap this malformation may span across several lobes [69]. Further support for the widespread nature of morphological anomalies and the associated epileptogenic zone may come from the unfavorable surgical outcome after focal resections in our patients, in line with reported series of patients with non-lesional frontal lobe epilepsy [3, 168]. While pathogenic mechanisms underlying FCD Type-I remain largely uncertain, it is enticing to hypothesize that cortical architecture in this condition may relate to abnormal tangential migration. Contrary to excitatory projection neurons obeying

the laws of gliophilic radial migration, the vast majority of GABAergic inhibitory interneurons arrive in the cortex *via* a tangential migratory corridor [169]. Notably, in this migration mode, neurons move parallel to the brain surface and their final positioning often transgresses regional boundaries [170]. Reduced arrival and abnormal maturation of inhibitory interneurons into the cortical plate may alter the balance between excitatory and inhibitory signaling, resulting in aberrant network hyperexcitability and widespread subtle morphological defects. This hypothesis is supported by metabolic imaging studies showing diffuse abnormalities of $GABA_A$ receptors [171].

Alterations of folding patterns are often used to typify malformations of cortical development, ranging from reduction in lissencephaly spectrum disorders caused by defective early neuronal proliferation to increased folding frequency in polymicrogyrias related to abnormal post-migrational development [72]. Considering this continuum, decreased sulcal-gyral complexity in FCD Type-II reinforces the notion of a defect occurring during initial stages of corticogenesis; conversely, increased complexity in FCD Type-I suggest a post-migrational anomaly [72].

Evidence-based clinical practice parameters foster novel combinations of quantitative neuroimaging with pattern learning techniques to objectively extract critical features and high dimensional data relationships [172]. Our findings emphasize that group-level phenotypes may guide fully automated and accurate diagnostic procedures in single patients. While seizure focus lateralization may optimize the performance of automated lesion detection algorithms, especially for previously overlooked lesions, non-invasive pre-operative prediction of FCD subtype and outcome may have implications for surgical planning and optimized patient counseling.

CHAPTER 5

MULTIMODAL MRI PROFILING AND SUBTYPE PREDICTION OF FOCAL CORTICAL DYSPLASIA TYPE-II

Preface

The previous project revealed diverging patterns of whole-brain structures between FCD Type-I and Type-II. These distinctive patterns allowed predicting the histopathological trait of an unseen case based on a pre-operative MRI and to develop subtype-specific machine-learning approaches for seizure-focus lateralization and outcome prediction. The excellent accuracies suggest that objectively grouping patients with seemingly heterogeneous pathological substrates into more homogenous sub-cohorts is critical for the optimization of clinical diagnoses.

Importantly, however, dysplasias may display subtle variabilities even within each subtype (*e.g.*, Type-IIA *vs.* IIB or Type-IA *vs.* IB) that are not distinguishable on visual inspection of MRI. Indeed, previous studies based on conventional MRI and qualitative assessments rarely provided systematic evidence of subtype-specific imaging features, except for the easily detectable transmantle sign, a salient feature of FCD Type-IIB.

The purpose of this study was to devise a novel lesion-profiling framework to maximally dissociate the imaging signatures between FCD Type-IIA and IIB, cohorts that are most frequently associated to extra-temporal drug-resistant focal epilepsy. To this end, we combined multimodal MRIs with advanced computational modeling of intra- and subcortical tissue properties of the primary lesion.

* * *

5.1 Abstracts

Focal cortical dysplasia (FCD) Type-II, a developmental malformation, is a leading cause of drug-resistant epilepsy. While cytopathological features distinguish FCD Type-IIA and IIB on histology, subtype-specific signatures on *in vivo* MRI remain unclear. We carried out a multimodal 3T MRI profiling of FCD. To dissociate subtypes, we quantified morphology, intensity, diffusion, and function across multiple intra- and subcortical surfaces. Geodesic distance mapping assessed the same features in the lesion perimeter. We applied our method to 33 consecutive patients with histologically-verified FCD Type-II. FCD Type-IIB was characterized by abnormal morphology, intensity, diffusivity and function across all surfaces, while Type-IIA lesions presented only with increased FLAIR signal and reduced diffusion anisotropy close to the grey-white matter interface. Similar to lesional patterns, peri-lesional anomalies were more marked in Type-IIB extending up to 16 mm. Structural MRI markers correlated with categorical histological characteristics. Machine-learning validated between-group differences at the level of individual subjects by automatically discriminating lesional from healthy tissue and predicting FCD subtypes with > 90% accuracy. Our ability to dissociate FCD subtypes at a mesoscopic level emphasizes the power of image processing applied to widely available MRI contrasts. *In vivo* staging of pathological traits promises to guide novel non-invasive surgical approaches as well as future individualized pharmacological interventions, such as those modulating mTOR-signaling.

This work was published in:
Hong SJ, Bernhardt BC, Caldairou B, Schrader D, Bernasconi N, Bernasconi A. *MRI-Based Lesion Profiling of Epileptogenic Cortical Malformations*. MICCAI 2015 9350:501-509.

and is under review:
Hong SJ, Bernhardt BC, Caldairou B, Hall JA, Guiot MC, Schrader D, Bernasconi N, Bernasconi A. *Multimodal MRI profiling of focal cortical dysplasia type II.* Neurology

5.2 Introduction

Focal cortical dysplasia (FCD) Type-II is a developmental malformation, primarily characterized by intracortical dyslamination and dysmorphic neurons, either in isolation (FCD Type-IIA) or together with balloon cells (FCD Type-IIB) [60]. Despite clear cytomorphological differences, FCD subtypes cannot be reliably distinguished on conventional MRI, even though qualitative studies have reported a tendency for more subtle anomalies in Type-IIA [68]. It has been suggested that identifying subtype-specific imaging signatures has potential clinical utility [60, 173, 174]. Notably, this ability may become increasingly relevant with the emergence of minimally invasive surgical procedures [175], which do not supply specimens for histological diagnosis.

The current study carried out a multimodal MRI analysis that combines morphometry with metrics interrogating tissue intensity, microstructure, and function in a cohort of patients with histopathologically-validated FCD Type-II. We designed a multisurface approach to systematically assess intra- and subcortical lesional features. Furthermore, motivated by reports showing pathological extension outside the lesional margin [14, 176], we evaluated the integrity of brain tissue adjacent to the lesion using a novel geodesic distance mapping and feature sampling procedures. Univariate and multivariate statistics were used to identify structural and functional signatures of FCD subtypes, logistic regression assessed the relationship between MRI and histology, while machine-learning allowed for individualized subtype prediction.

5.3 Methods

Subjects

From a database of patients with drug-resistant neocortical epilepsy admitted to the Montreal Neurological Institute and Hospital between 2009 and 2012, we selected 33 consecutive patients with histologically-proven FCD Type-II (17 males; mean±SD age=28±10 years, 13-55 years) [60].

Serial 5μm paraffin-embedded sections of lesional tissue were stained with haematoxylin and eosin or Bielschowsky, and other sections were immunostained using antibodies against glial fibrillary acid protein (GFAP), phosphorylated neurofilaments (SMI-32 monoclonal), microtubule-associated protein-2 (MAP-2), and neuronal specific nuclear protein (NeuN). FCD Type-II was defined as the presence of disrupted cortical lamination and cytological abnormalities characterized by dysmorphic neurons in isolation (Type-IIA, n=9) or together with balloon cells (Type-IIB, n=24). We evaluated the severity of cortical dyslamination, blurring of GM-WM boundary and gliosis on histology using categorical scoring (1=mild, 2=moderate, 3=severe). Histopathological subgroups did not show statistical differences in age, gender, age at seizure onset, disease duration, and seizure focus laterality ($p>0.1$).

The pre-surgical workup included seizure history, neurologic examination, neuroimaging, and video-EEG monitoring. EEG inter-ictal activity and ictal onset were concordant with the location of FCD lesions in 31 (94%) and 24 (73%) patients, respectively. In 15, surgery was preceded by invasive monitoring using stereotactic depth electrodes; all displayed a very active inter-ictal activity and focal changes at seizure onset in the electrodes targeting the lesion. Mean±SD postoperative follow-up was 4.1±1.4 years. We determined post-surgical seizure outcome using Engel's modified classification [177]; 21 patients became seizure-free (Engel-I), 8 had rare disabling seizures (Engel-II), and 4 had worthwhile improvement (Engel-III). The control group consisted of 41 age- and sex-matched healthy individuals, recruited through advertisements during the same

enrollment time as the patients. Demographic, clinical, and histological data are shown in **Table 5.1**.

Standard protocol approvals, registrations and patient consent

The Ethics Committee of the Montreal Neurological Institute and Hospital approved the study and written informed consent was obtained from all participants in accordance with the Declaration of Helsinki.

Table 5.1 | Demographic, electro-clinical data and histology

		Controls	FCD Type-IIA	FCD Type-IIB
Number of subjects		41	9	24
Male/Female		20/21	5/4	11/13
Age		29.7±7.3	29.4±9.9	26.3±8.5
Age at onset		-	14.1±7.0	13.6±5.9
Duration		-	13.8±7.2	13.9±9.7
Seizure focus (L/R)		-	6/3	10/14
Histopathology				
Dyslamination	Mild	-	57%	0%
	Moderate	-	43%	33%
	Severe	-	0%	67%
GM-WM blurring	Mild	-	43%	0%
	Moderate	-	43%	39%
	Severe	-	14%	61%
Gliosis	Mild	-	43%	0%
	Moderate	-	57%	17%
	Severe	-	0%	83%

Age, age at seizure onset, and duration of epilepsy are presented as mean±SD in years. Right and left refer to the seizure focus. Individual prevalence of histological anomalies in %.

MRI acquisition

Images were acquired on a 3T Siemens TimTrio scanner using a 32-channel head coil. The protocol included the following sequences: 3D T1-weighted MPRAGE (T1w; TR=2300 ms, TE=2.98 ms, flip angle=9°, voxel size=1×1×1 mm^3), 3D fluid attenuation inversion recovery (FLAIR; TR=5000 ms, TE=389 ms, flip angle=120°, voxel size=0.9×0.9×0.9 mm^3), 2D twice-refocused echo-planar diffusion-weighted images (d-MRI; TR=8400 ms, TE=90 ms, flip angle=90°, 63 axial slices, voxel size=2×2×2 mm^3, diffusion-sensitized images in 64 diffusion directions with b=1000 s/mm^2 along with one non-diffusion weighted volume), and echo planar resting-state functional MRI (rs-fMRI; TR=2020 ms, TE=30 ms, flip angle=90°, 34 slices, voxel size= 4×4×4 mm^3, 150 volumes). For the latter, participants were instructed to lie still with their eyes closed while remaining awake; to minimize signal loss and distortion affecting orbitofrontal and mesiotemporal regions, slices were tilted in an oblique axial orientation.

MRI preprocessing and multimodal data fusion (**Figure 5.1A-B**)

T1w and FLAIR images underwent intensity non-uniformity correction [91] and intensity normalization. T1w images were linearly registered to the MNI152 symmetric template, followed by classification into white matter (WM), gray matter (GM), and cerebro-spinal fluid (CSF) [178]. The d-MRI data were corrected for motion, eddy currents, and distortions; a tensor was fitted at every voxel to derive fractional anisotropy (FA) and mean diffusivity (MD) (FSL v5.0; http://www.fmrib.ox.ac.uk/fsl). After discarding the first 5 volumes, rs-fMRI underwent slice-time and motion correction, realignment, followed by statistical correction for nuisance effects of WM signal, CSF signal, and head motion. To correct for residual motion, we included time points with a frame-wise displacement >0.5mm as separate covariates [179]. Processing was conducted using DPARSFA (http://www.restfmri.net). All modalities (FLAIR, d-MRI, rs-fMRI) were linearly

registered to T1w MRI in MNI space. A boundary-based registration that prioritizes cortical alignment mapped rs-fMRI and d-MRI to T1w MRI [180].

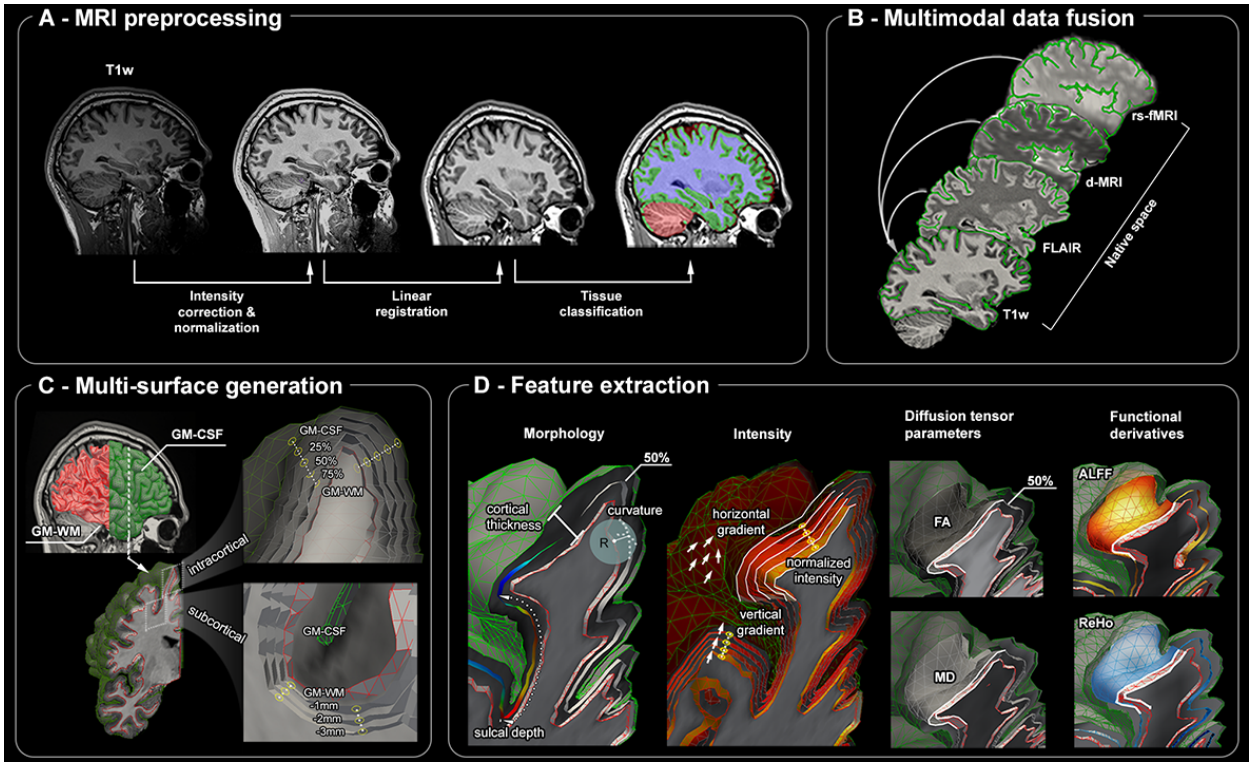

Figure 5.1. Image processing. **A)** T1-weighted undergoes intensity non-uniformity correction and normalization. T1w images are linearly registered to the ICBM-152 template and classified into tissue types. **B**) Multi-modal co-registrations map each modality to native T1w space. **C**) Models of the grey-white matter (GM-WM) and GM-CSF interface are generated, followed by reconstruction of equidistant intra-cortical and subcortical WM surfaces. **D)** Features of cortical and subcortical morphology, intensity, diffusion, and function (ALFF - amplitude of local functional fluctuation; ReHo - regional homogeneity) are calculated and represented in a unified surface-based frame of reference. See *Methods* for details.

Surface construction (**Figure 5.1C**)

We applied the CLASP algorithm [90] to preprocessed T1w images to generate models of the inner (GM-WM) and outer (GM-CSF) surfaces. In brief, CLASP iteratively warps a surface to fit the GM-WM boundary and estimates the outer surface by expanding the inner one along a Laplacian map. Surfaces were aligned based on cortical folding, improving inter-individual correspondence. Surface extraction accuracy was visually verified. To examine the intracortical GM, we positioned three surfaces between the inner and outer cortical surfaces at 25%, 50%, and 75% cortical thickness [181], guided by a straight line that provides vertex-correspondence across surfaces. These systematically sample the axis perpendicular to the cortical ribbon and may be used to probe laminar alterations [181]. To assess the WM immediately beneath the cortex, we generated a set of subcortical surfaces guided by a Laplacian field running between the GM-WM interface and the ventricles. Intervals between surfaces were adapted to the resolution of each modality.

Surface-based feature extraction **(Figure 5.1D)**

Two experts (DS and NB), blinded to clinical information and histopathology, segmented independently lesions on co-registered T1w and FLAIR images based on a combination of typical signs of FCD [8]. Inter-rater Dice agreement index, $D = 2|M_1 \cap M_2|/(|M_1|+|M_2|)$ (M_1: 1st label, M_2: 2nd label; $M_1 \cap M_2$: intersection of M_1 and M_2), was 0.91±0.11. This label was intersected with intra- and subcortical surfaces, generating a surface-based lesion label on which profiling was performed. We calculated at each vertex of the lesion label a series of morphological, intensity, diffusion, and functional features. To minimize interpolation during feature sampling, we mapped all surfaces (i.e., GM-WM, GM-CSF, intra-/subcortical surfaces) to the native space of each modality using the inverse transform of the initial linear registration.

a) Morphological features

- *Cortical thickness*. We measured thickness as the Euclidean distance between corresponding vertices on GM-WM and GM-CSF surfaces [90].
- *Sulcal depth and curvature*. Small FCD lesions are often located at the bottom of a deep sulcus [99]. To calculate sulcal depth, a brain hull model overlaid on cortical surfaces was used to detect gyral crown vertices, initialized at zero depth. The depth of vertices located within sulci was computed using the geodesic distance from gyral crown vertices [182]. By disrupting mechanical properties of the cortical mantle, FCD lesions may cause local curvature changes [99]; we measured absolute mean curvature along the 50% intracortical surface [183].

b) Intensity-based features

- *Normalized intensity*. We divided voxel-wise T1w and FLAIR intensity by the average GM-WM boundary intensity; this value was normalized with respect to the mode of the T1w and FLAIR intensity histogram [184] and mapped on each intra-/subcortical surface. Notably, we did not sample intensity on the outermost (i.e., GM-CSF) surface to avoid CSF contamination [181]; at remaining surfaces, we corrected intensities for residual CSF partial volume effect similar to a previous study [185].
- *Gradient*. At a vertex v, vertical gradient was computed as the difference in normalized intensity between corresponding vertices above and below v on neighboring surfaces, divided by their distance. For example, vertical gradient at v on the 50% intracortical surface was calculated as the intensity difference between the 25% and 75% intracortical surfaces, subsequently normalized by the inter-surface distance at v. Horizontal gradient was computed as mean intensity difference between v and its immediate surface neighbors,

divided by the mean distance between v and its neighbors. As for intensity, values at the GM-CSF surface were not considered. Decreased vertical/horizontal gradients within cortical surfaces were interpreted as proxies of radial/tangential dyslamination. Decreased vertical gradient at the level of GM-WM interface modeled blurring [184].

c) Diffusion parameters

FA and MD are surrogate markers of fiber architecture and tissue microstructure [186]. Given the lower resolution of d-MRI compared to FLAIR and T1w MRI, diffusion parameters were interpolated only at the 50% intracortical surface, the GM-WM boundary, and subcortical surfaces running at 2 and 4 mm depth.

d) Functional derivatives

We calculated two voxel-wise markers of local function: amplitude of low-frequency fluctuations (ALFF), a measure of bulk activation shown to relate to inter-ictal spiking [187], and regional homogeneity (ReHo) [188], which estimates time-series concordance between a voxel and its neighbors. Similar to d-MRI parameters, ALFF and ReHo were sampled on the 50% intracortical surface.

Statistical analysis

Our sampling assigned at each vertex a unique vector of intra/subcortical structural, diffusion, and functional features. To control for regional variations, features were smoothed using a surface-based 5 mm full-width-at-half-maximum Gaussian kernel and z-normalized at each vertex with respect to the corresponding distribution in controls.

a) Multisurface lesional profiling

By averaging features along each cortical and subcortical surface within a patient's consensus label, we generated MRI profiles for each patient. Student's t-tests compared these profiles between FCD subtypes. For individual analysis, we calculated proportions of patients with abnormal features (absolute z-scores $\geq$ 1.5) and feature combinations (multivariate Mahalanobis z-scores $\geq$1.5) averaged across surfaces.

b) Distance-based profiling

To assess feature transitions between the lesion and adjacent cortex, we computed the surface-based geodesic distance between all cortical points outside the label to the lesional boundary [189]. Compared to the Euclidian distance that measures the "straight line" distance, the geodesic distance is defined as the length of the shortest path between two vertices along the cortical surface, thus respecting topology. The distance map was discretized into bins of 2mm for T1w, FLAIR, d-MRI, and 4mm for rs-fMRI. Data were blurred using a minimal anisotropic smoothing (FWHM = 2mm) to maximize local specificity [190]; groups were compared using Student's t-tests.

c) Correlation with histological data

We applied multinomial logistic regression between histology scores and structural MRI markers (T1w, FLAIR, d-MRI): cortical dyslamination was modeled as decreased vertical gradients/ intensity, blurring as decreased vertical gradient at the GM-WM interface and subcortical intensity, and gliosis as hyperintensity and increased MD [191, 192]. Model fits were compared to null models using χ^2 tests [193].

d) Correction for multiple comparisons. Findings were controlled at a false discovery rate (FDR) of $q<0.05$ [194].

Prediction of histological subtypes through machine-learning

A multi-class support vector machine (SVM) [195] assessed the utility of imaging profiles to discriminate lesional from non-lesional tissue and to predict FCD subtypes. The learner integrated predictions of three base SVMs (IIA vs. IIB; IIA vs. controls; IIB vs. controls) through a max-wins voting scheme [195]. Specifically, the 3-class classification task was split into 3 binary classifications and the class with the most votes across learners determined the final prediction. Classifier performance was evaluated across combinations of: *i*) global features from single modalities (averaged across all surfaces); *ii*) global features from multiple modalities; *iii*) multimodal and multisurface features; *iv*) multimodal, multisurface, and distance-based features. Feature selection, classifier training, and performance evaluation were carried out using 10-fold cross-validation with 100 iterations. At each iteration, we randomly split the dataset in 10 subsets; the classifier was trained on nine and tested on the remaining one. A feed-forward procedure selected features best separating the three groups. McNemar's tests compared classifiers performance.

5.4 Results

Multimodal lesion profiling (**Figure 5.2**)

Relative to controls, FCD Type-IIB presented with FLAIR intensity increases across all cortical and subcortical surfaces, while T1w intensity was decreased only subcortically. T1w and FLAIR vertical gradients, modeling cortical radial dyslamination and blurring, were decreased at all

intracortical surfaces and at the GM-WM junction. Lesions also displayed increased subcortical MD and perturbed function, indexed by decreased ALFF and ReHo. With regards to morphology, Type-IIB also showed increased thickness and sulcal depth (**Figure 5.3**).

Unlike Type-IIB lesions, FCD-IIA did not show significant morphological, diffusion, or functional anomalies relative to controls. We only observed marginally increased cortical thickness and ReHo, and trends for decreased FA at the GM-WM interface (for these features, power analysis at α=0.025 and 1-β=0.8 revealed that limited findings were due to small effects; >125 patients would have been required to detect marginal changes). This subtype was mainly characterized by decreased T1w and FLAIR gradients (vertical and horizontal) close the GM-WM interface, as well as increased subcortical intensity relative to controls.

Directly comparing patient cohorts revealed increased thickness, sulcal depth, FLAIR intensity, as well as decreased ALFF and ReHo in Type-IIB, while Type-IIA showed decreased FA at the GM-WM interface.

Individual analysis is reported in the **Table 5.2**. Univariate analysis of single features confirmed more prevalent abnormalities in Type-IIB compared to IIA (mean [range]: 47% [13-88] vs. 23% [0-44], Wilcoxon Signed-rank test: $p<0.01$). Conversely, multivariate feature integration revealed comparable lesional load in both FCD subtypes (IIA: 75%; IIB: 88%). In controls, univariate and multivariate prevalence did not surpass 10%.

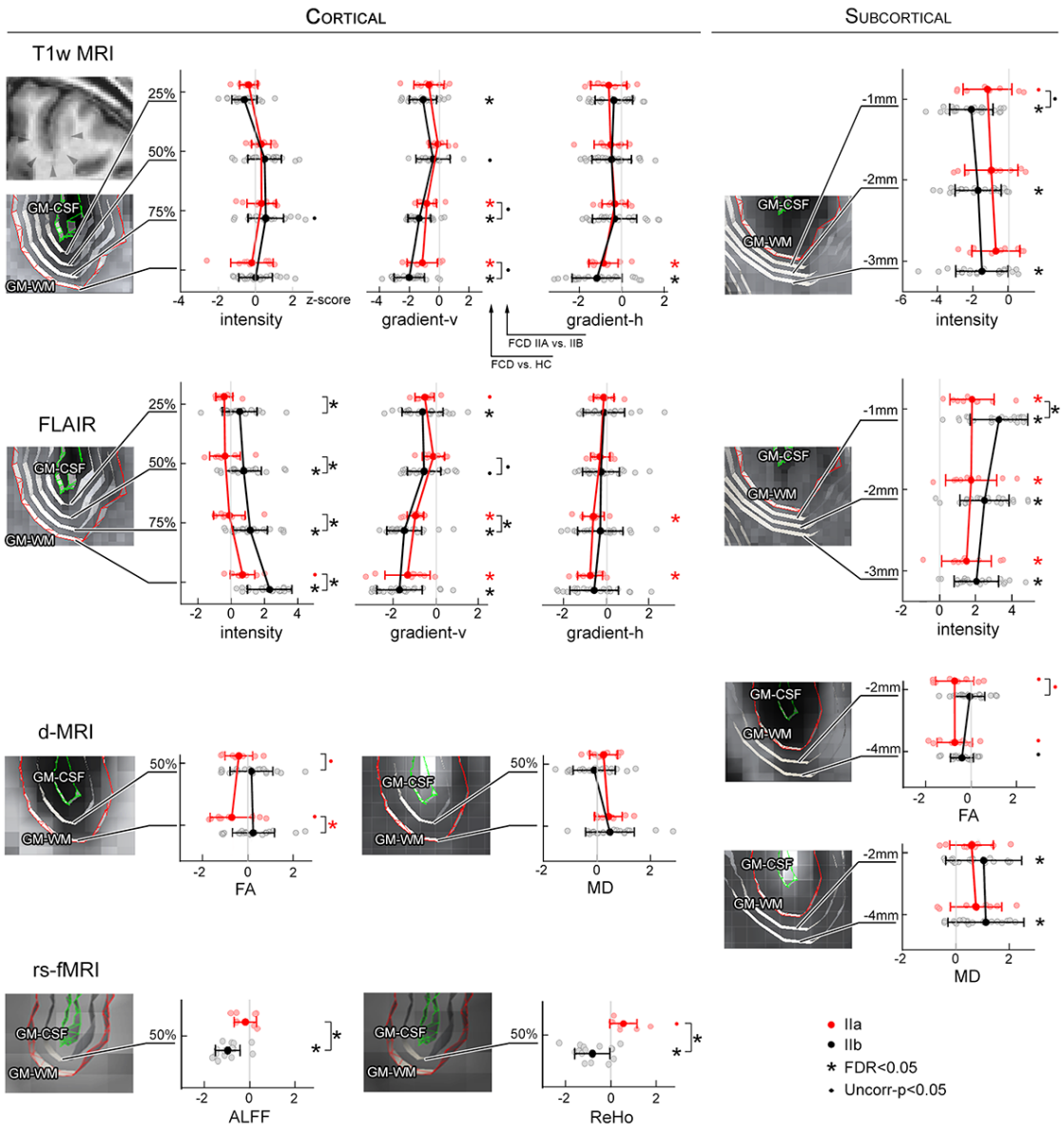

Figure 5.2. Multi-surface lesion profiling. For each modality, individual patients (normalized with respect to corresponding regions in healthy controls) are plotted as a function of intra-cortical and subcortical level, separately for Type IIA (red dot) and Type IIB (black dot); zero reference line indicates the mean of controls; mean values and standard deviations in patients are shown as horizontal lines.

Figure 5.2. Contd. Asterisks indicate significant differences from controls and between cohort contrasts; small dots indicate trends. Profiling was based on a surface spacing that accommodated imaging resolution. An example case is shown in the upper left panel, with arrowheads pointing to the lesion. For abbreviations, see ***FIGURE 1***.

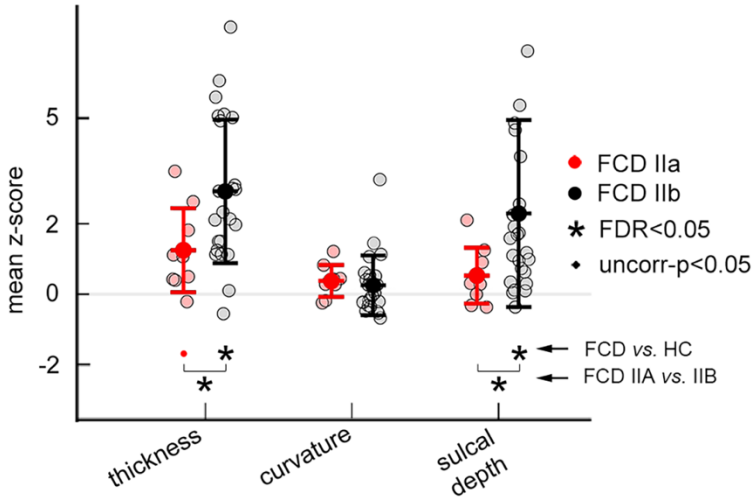

Figure 5.3. Morphological profiling. Individual patients, mean lesional feature values, and standard deviations (normalized with respect to corresponding regions in healthy controls) are plotted. For details, please see ***Figure 2***.

Table 5.2. Individual prevalence of MRI abnormalities across FCD subtypes.

Modalities and features		|z| > 1.5	
		Type IIA	Type IIB
T1weighted - thickness, curvature, sulcal depth		33%	75%
T1weighted, FLAIR			
normalized intensity	*Cortical*	11%	33%
	Subcortical	44%	88%
vertical gradient	*Cortical*	0%	42%
	GM-WM boundary	44%	79%
horizontal gradient	*Cortical*	11%	13%
	GM-WM boundary	22%	50%
Diffusion MRI - FA & MD	*Cortical*	11%	13%
	Subcortical WM	44%	33%
FMRI - ALFF & ReHo	*Cortical*	11%	46%
Multimodal combination		75%	87%

For individual analysis, features (*i.e.*, absolute z-scores ≥ 1.5) and feature combinations (*i.e.,* multivariate z-scores ≥1.5) are averaged across surfaces. *Abbreviations:* FA: fractional anisotropy; MD: mean diffusivity; ALFF: amplitude of local functional fluctuation; ReHo: regional homogeneity.

Distance-based analysis (**Figure 5.4**)

Structural neocortical features were abnormal until 6 mm away from the lesional boundary, while functional and subcortical diffusion alterations extended up to 16 mm. Anomalies were more marked in Type-IIB, aside from FLAIR cortical vertical gradient and subcortical intensity that were equally present in both subtypes. On the other hand, reduced cortical FA, specific to Type-IIA, extended up to 6 mm outside the lesion. Notably, the extent of peri-lesional anomalies did not correlate with lesion volume ($p>0.2$).

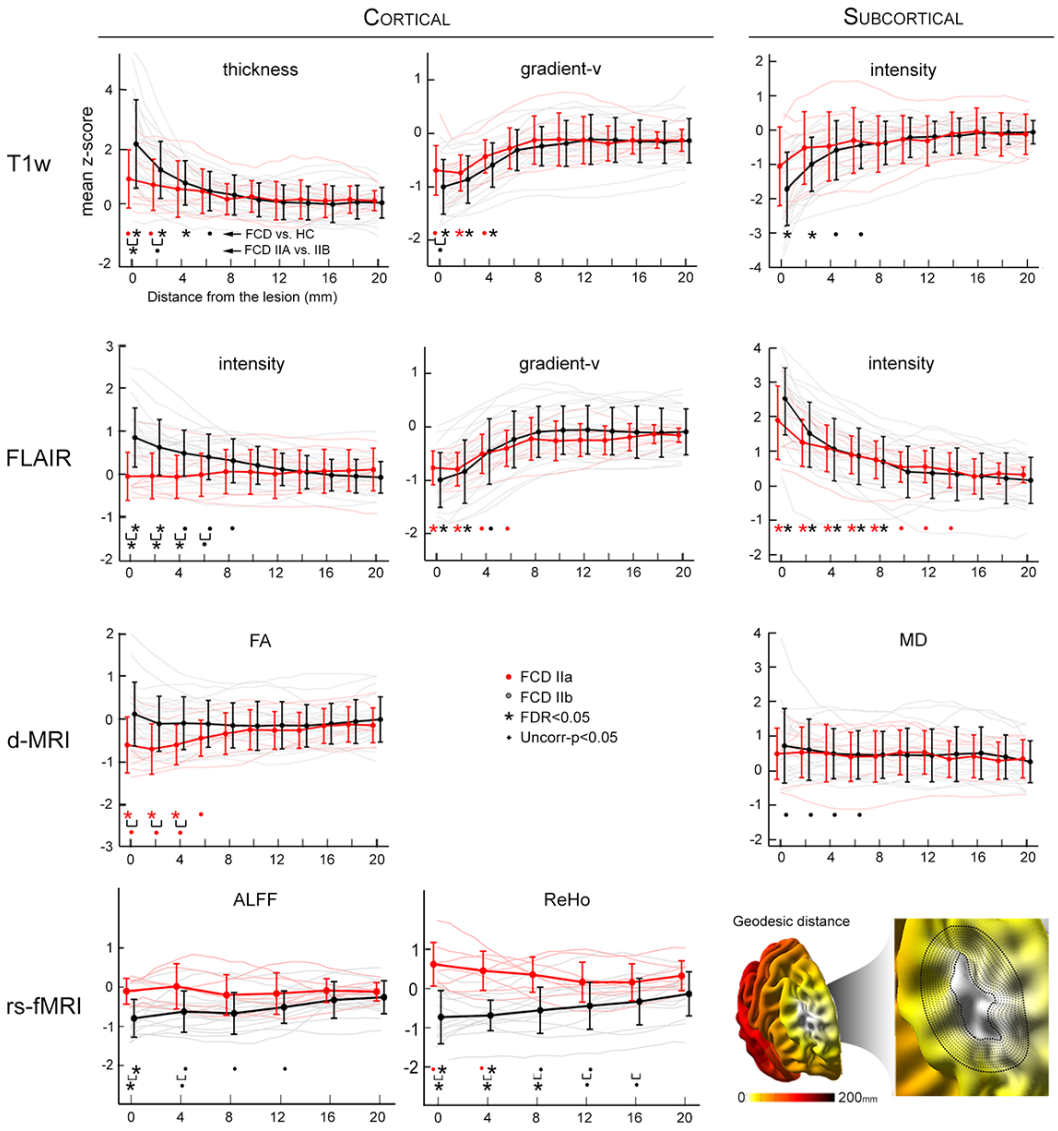

Figure 5.4. Distance-based profiling of the lesion perimeter. For each modality, features were normalized with respect to corresponding regions in controls and averaged across cortical and subcortical surfaces. Normalized data are plotted relative to the geodesic distance from the primary lesion (in steps of 2mm for T1w, FLAIR and d-MRI and 4mm for rs-fMRI). The binning scheme is exemplified in the right bottom panel.

Histological correlation analysis (**Figure 5.5**)

As for the MRI profiles, we observed more marked anomalies across histological features (i.e., dyslamination, GM-WM blurring, and gliosis) in Type-IIB compared to Type-IIA (χ^2 test; $p<0.005$; see **Table 5.1** for details). Moreover, the severity of histological anomalies correlated with the corresponding MRI profiles for dyslamination ($R^2 = 0.71$; $p<0.005$), GM-WM blurring ($R^2 = 0.73$; $p<0.003$) and gliosis ($R^2 = 0.55$; $p<0.01$).

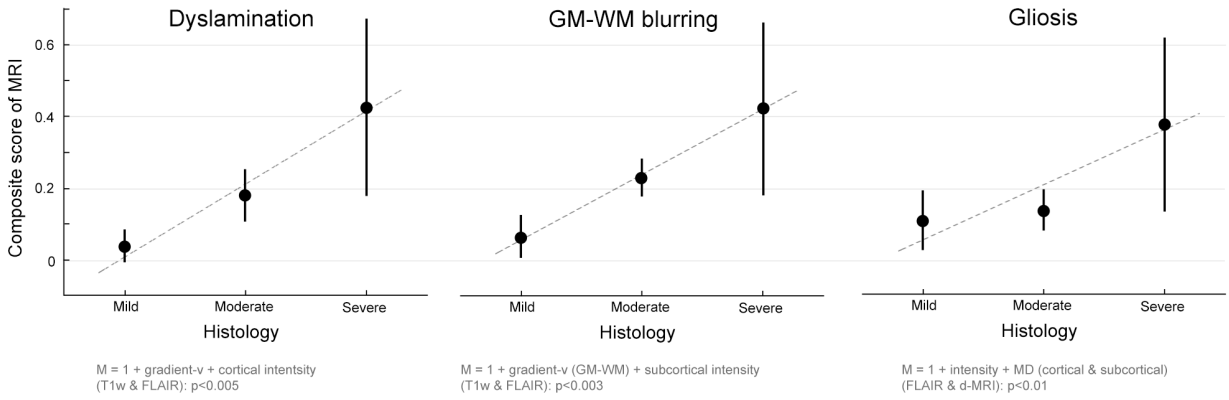

Figure 5.5. Histological correlation. Associations between severity of cortical dyslamination, blurring of GM-WM boundary and gliosis on histology using categorical scoring and composite scores of MRI features. The composite score was computed based on regression coefficients estimated from a statistical model. Details of models are displayed below each graph, together with MRI features as independent variables as well as significance of model fit.

Subtype prediction (**Figure 5.6**)

When using unimodal features averaged across all surfaces, multiclass SVM correctly predicted subtypes in 61±3% (d-MRI), 73±4% (T1w), 78±2% (rs-fMRI), and 79±3% (FLAIR) of cases. Combining features in a multivariate manner did not improve overall accuracy (75±4%).

Conversely, multisurface classifiers improved performance (89±4%; McNemar's test: χ^2>3.13, p<0.04), especially when adding distance-based profiles (91±4%, McNemar's test: χ^2>4.0, p<0.025). Permutation tests with 10,000 iterations confirmed that accuracy surpassed chance-level (p<0.001, permutation-based accuracies = 13-61%). Features discriminating FCD subtypes (ordered by contribution) were: T1w vertical gradient (75% intracortical level), ReHo, T1w cortical intensity (50-75% levels), FLAIR vertical gradient (75% level), and FLAIR subcortical intensity (2 mm below GM-WM). cross-validations, a mean±SD=0.6±0.7 (range=0-2) of controls were categorized as FCD, indicating excellent specificity.

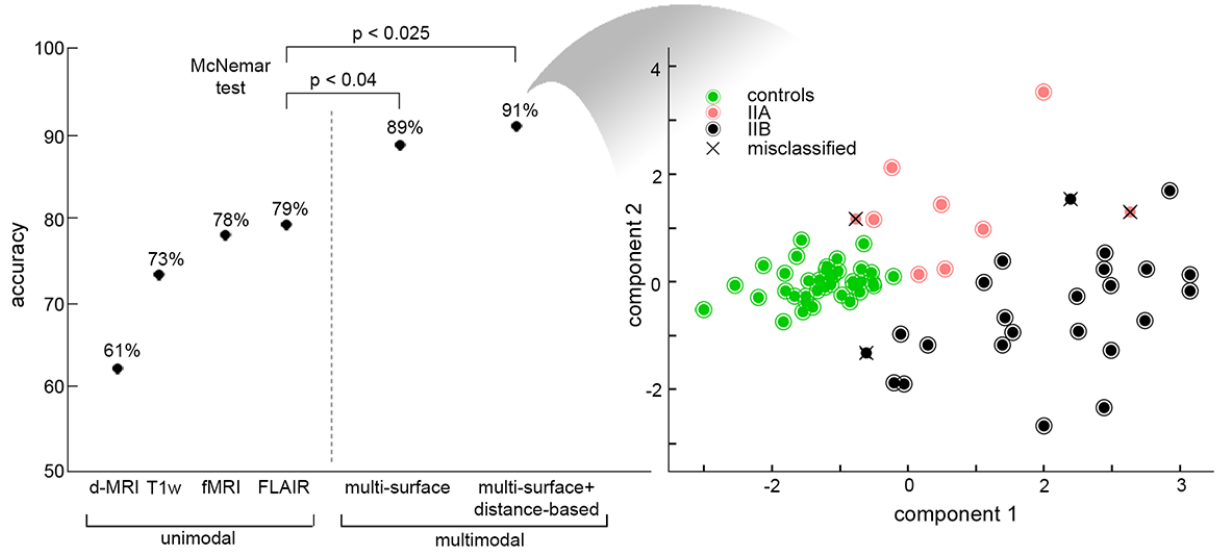

Figure 5.6. Automated FCD subtype prediction based on supervised pattern learning. *Left panel:* Prediction accuracy across unimodal (*i.e.*, lesional features derived from one modality) and multimodal feature combinations (multi-surface and distance-based). McNemar's test compared classifier accuracy across different feature combinations. *Right panel:* Illustration of classifier accuracy at optimal performance. The high dimensional feature space was projected to 2D using a multi-dimensional scaling. Red and Black indicate each Type-IIA/-IIB, respectively. Corresponding control profiles are shown in green. Misclassified cases are marked by a cross. Please see *Methods* and *Results* for details.

5.5 Discussion

We designed a novel multisurface image analysis method that integrates structural and functional MRI in a unified framework, allowing for dense *in vivo* sampling of FCD Type-II characteristics based on manually segmented lesion labels. To to avoid rater-bias, we relied on two experts separately outlining FCD lesions based on typical signs. Moreover, access to healthy controls added confidence to establish the degree of anomalies. While absence of digitized tissue samples prevented a fully quantitative comparison between MRI and histology, our imaging markers reflecting categorical variations of the main FCD characteristics emphasize the ability of advanced multimodal MRI post-processing to capture histopathology at mesoscopic scale.

In line with histopathological reports [196, 197], abnormal morphology, intensity, and gradients across both GM and WM compartments characterized FCD Type-IIB. Conversely, Type-IIA lesions primarily displayed increased FLAIR and decreased diffusion anisotropy close to the GM-WM interface, which may reflect preferential occurrence of dysmorphic neurons in deeper cortical layers [198], while decreases in diffusion anisotropy may speak to minimal demyelination and decreased fiber membrane circumference without apparent changes in density [186]. Notably, increased subcortical FLAIR in both subtypes is highly suggestive of gliosis, which was equally prevalent in our cohorts.

Functional profiling provided independent support for subtype difference. In Type-IIA, increased ReHo, similar to observations in the epileptogenic hippocampus of patients with temporal lobe epilepsy, may reflect enhanced synchronization [199]. As epileptogenicity in FCD Type-II is primarily attributed to dysmorphic neurons [64], it is plausible that aberrant neuronal activity may propagate more freely in Type-IIA than IIB; in the latter, balloon cells would hinder local

connectivity to the surrounding networks or disrupt it [200, 201], a hypothesis corroborated by the decrease in both ALFF and ReHo.

There is only little consensus on whether Type-II dysplasias have distinct - or rather gradual - boundaries with adjacent cortex [14, 196]. Using distance-based feature profiling along the cortical manifold, we showed that normal-looking cortex in the lesion perimeter is impacted by alterations resembling those found in the core of the FCD. At the scale of neuroimaging, our findings suggest a rather smooth transition from dysplastic to normal cortex that challenges visual appreciation, motivating quantitative approaches to refine objective lesion delineation. To address the clinical significance of perilesional anomalies, particularly with regards to seizure outcome, future studies should integrate preoperative profiling data with postoperative imaging, histopathology, and long-term follow-up information. Moreover, it is noteworthy that local implementation of routines such as those we propose would rely on the availability of independent patient datasets, expert MRI segmentation and control population to assess specificity.

Pattern-learning paradigms validated between-group differences at the level of individual subjects, by automatically discriminating lesional from healthy tissue and predicting FCD subtypes with high accuracy. Such an approach has also been successfully used for *in vivo* staging of dementia [186] and tumor grades [202]. In our data, maximal discrimination accuracy was achieved when integrating multisurface profiles with distance mapping, emphasizing the value of multimodal feature engineering that comprehensively characterizes the embedding of the dysplastic tissue. Ultimately, the image analysis framework we propose may promises to guide novel non-invasive surgical approaches, such as minimally invasive laser-induced thermal ablation for which the underlying histological substrate will remain unknown [175]. Moreover, our distance-based profiling

that quantifies the tissue beyond the visible border offers novel opportunities to optimize the treatment of cortical dysplasias. With respect to resective surgery, a lack of precise delineation of lesional extent may prompt either an incomplete or too large resection; in the first scenario, the seizure outcome is compromised, while the second may be associated with functional deficits. Finally, in light of new data showing alterations in the mechanistic target of rapamycin (mTOR)-signaling pathway in cortical dysplasia, our multimodal profiling approach may inform the selection of novel therapeutic agents and monitor individualized response to pharmacological interventions, such as those modulating mTOR-signaling. In all these instances, pre-treatment mapping combining in vivo image-based analysis of structural integrity together with non-invasive electrophysiological techniques, such as MEG, is likely to define physiological and functional integrity of the dysplastic tissue, improving the likelihood of a successful surgical or medical therapy [203].

CHAPTER 6

MAPPING BRAIN NETWORK ALTERATIONS IN MALFORMATIONS OF CORTICAL DEVELOPMENT

Preface

Although our previous project (#2) provided the first evidence of widespread pathological substrates in MCD, the finding was limited to only a single subcohort (*i.e.*, FCD) and thus needs to be assessed its generalizability across different spectrum of MCD. Moreover, previous MRI studies so far carried out only a univariate analysis, where each cortex has been separately probed. Given that the brain is inherently a network structure, however, this approach may not adequately capture a systemic disease effect that can alter large-scale organizational principles.

While the majority of MCD onsets during a corticogenic period, the effect of its initial insults is lifelong in affected patients, significantly disrupting functional integrity of their mature brains. To fully understand these disease effects, therefore, one needs appropriate tools to separately probe structural organization affected during development and its functional consequence on the post-natal brain. Although the ideal approach for this purpose would be a prospective longitudinal follow-up of diseased brains using multimodal imaging even from a fetal period, practical cost-related challenges as well as difficulty of knowing in advance whether a given case will manifest as a diseased brain or not prevent to apply this design on actual researches.

Here, we carried out a structural covariance analysis, a meaningful and cost-effective, cross-sectional approach to infer networks closely corresponding to those undergoing common maturational change during development, based on anatomical MRI of a patient's mature brain. Assessing multiple subtypes of MCD, we also analyzed its counterpart, functional networks to evaluate the disease translation from an atypical structure to the functional architecture as a pathological consequence. Together with a final integrative structural-functional coupling analysis, this project tried to find novel evidence to show main principles of developmental organization that may be shared by a full spectrum of MCDs.

* * *

6.1 Abstracts

Malformations of cortical development (MCDs) are increasingly recognized to participate in multiple neurological and neuropsychiatric disorders. While traditionally associated to focal lesions, emerging evidence suggests rather distributed underlying pathological substrates in MCDs. By combining structural covariance assessment with resting-state fMRI connectivity analysis, we provide novel evidence for large-scale network reorganization across a spectrum of MCD patients. We observed that structural networks were more regularized in patient groups whereas their functional topology became increasingly inefficient. Notably, these findings consistently revealed gradually altered patterns depending on the presumed onset of the underlying malformative process. Specifically, cortical dysplasias (associated to atypical neuronal proliferation) showed only subtle alterations, while effects were larger in heterotopias (related to abnormal neuronal migration), and maximal in polymicrogyria (perturbed in a late-stage cortical disorganization). By suggesting progressive structure-function decoupling along the malformative onset, our connectome-level phenotyping offers novel perspectives on brain development and neurodevelopmental disorders.

This work is to be submitted in:
Hong SJ, Bernhardt BC, Bernasconi N, Bernasconi A. *The spectrum of cortical malformations is associated to gradual structural–functional network alterations*. Proceedings of the National Academy of Sciences

6.2 Introduction

Cortical development is governed by a multitude of interacting genetic, epigenetic, and environmental factors, and has been a focus of neuroscience for decades [1]. Empirical studies as well as theoretical models have largely converged in sub-classifying this process into three partially overlapping phases, which nevertheless occur serially throughout the gestational period [21, 30]: *i) Proliferation* of primary progenitor cells and differentiation into neurons or glial cells in the ventricular periphery; *ii) Migration* of cortical neurons along the radial glial scaffold or in tangential direction towards the cortical plate, where cells arrive in an inside-out pattern depending on their ontogenetic age; *iii) Organization* of the cortex, characterized by substantial areal and laminar differentiation, together with the formation of large-scale connections.

Disturbances at different stages of the complex neurodevelopmental process are related to disorders affecting a large proportion of children and adults worldwide, with an immense individual burden and societal cost [204]. A highly prevalent and relatively well-characterized class of such conditions is referred to as malformations of cortical development (MCDs), frequently associated with drug-resistant epilepsy, intellectual disability [50], and likely autism spectrum disorders [205]. A current taxonomy classifies individual MCDs with different phenotypical and genetic causes into three main categories, relative to the stage in which corticogenesis is mostly affected [48]. For instance, focal cortical dysplasia type-II (FCD-II; dysplastic cortex characterized by dysmorphic neurons and balloon cells) has been related to abnormal cell proliferation, whereas periventricular or subcortical heterotopia (HET; neuronal clusters in the subcortical white matter) has been suggested as a result of a neuronal migration failure. On the other hand, polymicrogyria (PMG; excessive number of small and shallow sulci) or FCD-I (subtle dyslamination and ectopic neurons in the white matter) is associated with atypical cortical organization. Given that these

primary lesions are often epileptogenic, the majority of previous clinical neuroimaging studies were largely translational in nature and focused on localized lesion characterization [49, 206, 207].

Nonetheless, single case-reports and sporadic radiological studies have suggested that structural anomalies in MCDs may extend beyond the margins of the visible lesion [14, 16] and even affect whole-brain morphology [103, 208]. While incompletely understood, extra-lesional anomalies have been attributed to aberrant inter-regional connectivity between a core pathology and the rest of the brain [209], as demonstrated by an early animal study showing distant gyral abnormalities in the prenatal brain following experimental lesioning [210]. Collectively, these findings suggest that MCD may not solely be a pure focal disease related to a single lesion, but more adequately be conceptualized as a network disorder that involves distributed pathological substrates [104] and whose developmental origins may derive from wide-reaching disruptions in genetic expression levels and maturational-trophic exchange patterns [211, 212].

Here, we assessed large-scale structural and functional brain networks in a sample of 154 MCD patients, who showed disruptions at different main stages of corticogenesis (*i.e.*, FCD-II, HET, PMG and FCD-I). We aimed at evaluating two key principles of cortical malformations. First, given a high influence of the malformative onset on the phenotype of the primary lesion, we hypothesized that large-scale network organization may also be perturbed as a function of corticogenic timing. Second, in light of the notion that the structural basis largely determines functional interactions in a given system [213], one may expect that MCD-related alterations in structural network organization translate into abnormal functional architecture. We generated structural networks in MCD patients using covariance analysis of MRI-derived cortical thickness, a technique that infers networks closely corresponding to those undergoing common maturational change during development [110]. On the other hand, functional connectomes were derived from the analysis of inter-regional fMRI time-series correlations, obtained during a task-free acquisition.

Based on multimodal connectome datasets, we carried out a comprehensive array of statistical and graph-theoretical analyses evaluating alterations in inter-regional associations, small-world parameters [214], and rich-club organization [215] across a large cohort of MCD patients. Analyses were repeated across two parcellation schemes (*i.e.*, 78 and 1000 cortical parcels) and across independent datasets, to verify robustness of our findings. In an integrative structural-function analysis, we finally evaluated the coupling between reorganization of the structural-maturational and functional connectome at rest.

6.3 Methods

Subjects

From a database of patients admitted to the Montreal Neurological Institute and Hospital for the investigation of drug-resistant epilepsy, we selected 154 consecutive patients with different MCDs who had been examined with either a 1.5T (n=91) or 3T (n=63) MRI scanner with an identical imaging protocol.

In 1.5T dataset, subtypes of MCDs included Focal Cortical Dysplasia (FCD) Type-II (n=30, male=16, mean±SD of age=29±9; abnormal neuroglia proliferation), heterotopia (HET; n=27, male=11, age=28±12; arrested cell migration), as well as polymicrogyria (PMG; n=21, male=12, age=29±11) and FCD-I (n=13, male=7, age=29.2±8.7) (both disturbed cortical organization). Demographic and clinical data were obtained through interviews with the patients and their relatives and by reviewing hospital charts. In all patients, diagnosis and lateralization of the seizure focus were determined by a comprehensive evaluation, including detailed seizure history and semiology, neurological examination, video-EEG telemetry, and neuroimaging.

While the primary lesions in patients with FCD-II were seen either on conventional MRI (n=20) or became visible through texture analysis [80] (n=10), those in FCD-I cohort were all unremarkable

even after MRI postprocessing. In the latter group, surgery was preceded using stereotactic implanted depth electrodes. A putative FCD lesion was surgically resected in all FCD patients and histopathologically confirmed as either Type-I or Type-II along the criteria of recent FCD classification system (*i.e.*, based on the existence of dysmorphic neurons) [60]. A lesion in these groups (Type-I and Type-II) was located in the left/right side in 7/6 and 15/15 patients, respectively.

On the other hand, the classification of HET and PMG was carried out based on MRI phenotype of the primary lesion. Majority of HET cases had a periventricular nodule (n=25) whereas only 2 cases had a subcortical nodule. A nodule was located in the left/right/bilateral side in 6/10/11 patients, respectively. PMG consists of 17 typical perisylvian lesion cases and 4 fronto-parietal lesion cases. The lesion was located in the left/right/bilateral side in 6/5/10 patients, respectively. In patient groups, there were no statistical differences in age, disease duration, gender distribution, seizure focus lateralization and localization, and number of generalized seizures.

3T MRI dataset was included for the purpose of reproducibility test and also for evaluation of resting-state functional network. It included FCD-II (n=33, male=16, age=28±10), HET (n=17, male=10, age=31±10) and PMG (n=13, male=8, age=31±12). Every details related to the clinical workup and disease classification have been carried out using identical procedures than those of patients with 1.5T MRI. In both 1.5T and 3T datasets, the control groups consisted of 41 age- and sex-matched healthy subjects. **Table 6.1 and 6.2** summarized demographic and clinical data. The Ethics Committee of the Montreal Neurological Institute and Hospital approved the study and written informed consent was obtained from all participants.

Table 6.1. Demographic and electro-clinical data.

	Controls	MCD			
		FCD-II	HET	PMG	FCD-I
No. participants	41	30	27	21	13
Male/Female	16/25	16/14	11/16	12/9	7/6
Age, y	31±11	28±10	28±12	29±11	29±9

Age, age at seizure onset, and duration of epilepsy presented as mean±SD. *Abbreviations*: R/L; right/left

Table 6.2. Demographic and clinical data of patients with 3T MRI.

	Controls	MCD			
		FCD-II	HET	PMG	FCD-I
No. participants	41	33	17	13	
Male/Female	21/20	16/17	10/7	8/5	
Age, y	30±7	28±10	31±10	31±12	

Age, age at seizure onset, and duration of epilepsy presented as mean±SD. *Abbreviations*: R/L; right/left

MRI acquisition and processing

1.5T structural T1-weighted MRIs were acquired on a Philips Gyroscan using a 3D T1-fast field echo sequence (TR=18 ms; TE=10 ms; flip angle=30°; matrix=256×256; FOV=256×256 mm^2; slice thickness=1 mm) providing isotropic voxel dimensions of 1×1×1 mm. The 3T dataset was obtained on a Siemens TimTrio scanner using a 32-channel head coil. The structural MRI acquisition employed 3D T1-weighted (T1w) magnetization-prepared rapid-acquisition gradient echo (TR=2300 ms, TE=2.98 ms, flip angle=9°, voxel size=1×1×1 mm^3), the functional data was scanned using 2D echo planar resting-state functional MRI (rs-fMRI; TR=2020 ms, TE=30 ms, flip angle=90°, 34 slices, voxel size= 4×4×4 mm^3, 150 volumes). For the latter, participants were instructed to lie still with their eyes closed while remaining awake; to minimize signal loss and

distortion affecting orbitofrontal and mesiotemporal regions, slices were tilted in an oblique axial orientation.

Structural MRI preprocessing included correction for intensity non-uniformity, intensity standardization, linear registration to the MNI152 template, and classification into white matter (WM), gray matter (GM), and cerebrospinal fluid (CSF). The Constrained Laplacian Anatomic Segmentation using Proximity (CLASP) algorithm generated a model of the inner (WM-GM) and outer (GM-CSF) surfaces with 40k points (or vertices) for each hemisphere. Surfaces were aligned to a hemisphere-symmetric surface template to improve inter-individual correspondence. The accuracy of surface extractions was verified in all subjects prior to further analysis. Since each vertex on the surface has a correspondence between inner and outer boundary through a straight link (*i.e.*, 't-link'), we could generate a map of cortical thickness, as in our previous study [156].

After discarding the first 5 volumes, rs-fMRI underwent slice-time and motion correction, realignment, followed by nuisance covariate regression to remove effects of WM signal, CSF signal, and head motion. To correct for residual motion, we included time points with a framewise-displacement >0.5mm as separate covariates [179]. Processing was conducted using DPARSFA for Matlab (http://www.restfmri.net). A boundary-based registration that prioritizes cortical alignment allowed us for projecting cortical surfaces from T1w to the native space of rs-fMRI and mapping the time-series on the 50% of mid-surface (averaged one between inner and outer cortical surfaces). For functional network construction, we used these surface-mapped time-series signals across subjects.

*Construction of cortical covariance matrices and density-based thresholding (**FIG 1A**)*

a) Parcellation.

We used automated anatomical labeling (AAL) to parcellate the cerebral cortex into 78 cortical regions [138]. An individual MRI was nonlinearly warped to the Colin27 single-subject template [216] on which the original AAL was defined. Using the inverse of this transformation, labels were mapped to the individual MRI and intersected with cortical surfaces to generate a subject-specific AAL surface parcellation.

b) Structural and functional network construction.

We first calculated parcel-wise mean values of each metric (*i.e.*, cortical thickness and functional time-series); parcel-wise thickness were, in turn, statistically corrected for effects of age, gender, and global mean values, as in previous work [107]. For the methodological consistency, we equally regressed out same statistical effects from functional time-series. To construct a structural covariance network ($R_{S\text{-}78}$), we systematically calculated the cross-correlation coefficient r_{ij} of the mean cortical thickness between all pairs of regions i and j across subjects, providing a single group-level matrix at each cohort (*i.e.*, control, FCD, HET and PMG, separately). On the other hand, generating a functional network ($R_{F\text{-}78}$) was based on the temporal correlation between inter-parcel 'time-series' signals, therefore yielding an individual matrix at each subject.

c) Network thresholding.

The correlation matrix $R_{S/F\text{-}78}$ was thresholded to a binarized matrix $A_{S/F\text{-}78}$ at a certain density, where an entry a_{ij} equals 1 if r_{ij} exceeded a given threshold and 0 otherwise. The density of a

network was defined as the percentage of the number of actual connections K divided by the number of possible connections, density = $K / (n \times (n\text{-}1)) \times 100\%$ where n is the number of nodes. To evaluate whether findings are robust against different densities of the network, we systematically varied this threshold over a wide range (5-40%) throughout the study, using algorithms implemented in the Brain Connectivity Toolbox [217]. We restricted our analysis to positive correlations only.

d) Group networks.

Notably, the main purpose of this study was to evaluate the '*backbone*' of a given system [218] that epitomizes the core *group-level* characteristics of MCD networks. While the matrix of structural covariance network was naturally constructed to capture the group-level patterns by the methodological principle, the functional network matrices are originally individual-based; thus, again, in order to keep a methodological consistency, we combined those individual matrices at each group, following previously proposed approaches [215, 219]. Briefly, from the set of individual matrices, only connections that were present in at least 50% of population of a given group were selected, while all other connections were set to 0. This procedure effectively removed the improvised correlation occurred among subjects and identified only highly consistent "group-representative" connections.

Assessment of inter-regional correlation

To assess differences in inter-regional correlation coefficients between each patient group and controls, entries r_{ij} of the correlation matrices R were transformed using Fisher's *R-to-Z* transformation, where an individual entry was calculated as

$$z_{ij} = \frac{1}{2} ln\left(\frac{1 + r_{ij}}{1 + r_{ij}}\right)$$

Clustering Coefficient and Characteristic Path Length

We computed the clustering coefficient and characteristic path length in controls and all MCD groups at both global and nodal level, using standard formulas [220]. These quantities are the widely used graph-theoretical parameters to describe the topology of complex networks. Clustering coefficient c_i of a given node i, and mean clustering C were defined as:

$$c_i = \frac{E_i}{k_i(k_i - 1)/2} \qquad \mathrm{C} = \frac{1}{n}\sum_{i=1}^{n} c_i$$

where E_i is the number of existing connections among the neighbors of node i. As k_i is the actual number of neighbors of node i (*i.e.*, its degree), the denominator term $k_i(k_i-1)/2$ quantifies the number of all possible connections among the neighboring nodes. If a node i had only one edge or no edges, c_i was set to 0. The mean clustering coefficient C of a network was defined as the average of c_i over all nodes in the network N. C quantifies the cliquishness and is related to the local efficiency of a network [221].

Average shortest path length l_i of a given node i, and characteristic path length L were defined as

$$l_i = \frac{1}{n-1}\sum\nolimits_{i \neq j} min\{l_{ij}\} \qquad \mathrm{L} = \frac{n}{\sum_{i=1}^{n} l_i}$$

In the above formula, $\min\{l_{ij}\}$ denotes the shortest absolute path length between two given nodes *i* and *j*. The characteristic path length *L* of a network was defined as the mean minimum number of edges that lie between any two nodes in the network. To overcome the problem of dramatically increased L values in networks with possibly disconnected components, L was calculated using a harmonic mean definition [107]. The reciprocal of *L* is a measure of parallel information transfer or global efficiency of a network [221].

Normalized Clustering Coefficient and Path Length

The normalized clustering coefficient γ was computed by dividing the clustering coefficient of the actual network *C* by the mean clustering coefficient C_{rand} across 1000 randomly generated networks. These random networks had the same number of nodes, edges, and an identical degree distribution as the real network [222]. An analogous approach was used to compute the normalized path length λ. Compared with random networks, small-world networks have a similar characteristic path length, but higher clustering, that is $\gamma = C/C_{rand} > 1$ while $\lambda = L/L_{rand} \approx 1$ [220].

Rich Club Organization of Structural and Functional Brain Network

The '*rich club*' organization refers to the topology in which the highly connected (high-degree) hubs of a network are more densely connected among themselves than predicted on the basis of their high degree alone [215]. This topology, previously found as a typical characteristic of human brain, is a critical feature to form a central high-capacity backbone for integrative brain communication [218]. By quantifying the degree of this topology in MCDs, therefore, we can evaluate malformation-related changes in inter-hub connectivity, the core underlying architecture to sustain a given system. A rich-club coefficient $\phi(k)$ was computed as the ratio of the number of connections between nodes within the k^{th} subgraph and the total number of possible

connections between them, which can be formulized as a following equation:

$$\phi(k) = \frac{2E_{>k}}{N_{>k}(N_{>k} - 1)}$$

Since even random networks may show an increasing value of $\phi(k)$ simply because the nodes with a higher degree have a higher probability of being interconnected by chance, we normalized $\phi(k)$ of each group with respect to those of its corresponding random networks that have been generated in an exactly same manner (*i.e.*, 1000 iterations of randomization) than in small-world parameters.

$$\phi_{norm}(k) = \frac{\phi(k)}{\phi_{random}(k)}$$

Finally, we designate the range of *k* where ϕ_{norm} shows >1 as the gnate-club regime".

Rich club nodes and connection classes

After computing a global coefficient, nodal-level rich club regions were also identified at each group by setting up the rich-club level as more that 11 of *k*, a degree providing the highest $\phi_{\square orm}$ in the control group. Accordingly, the nodes of $k<11$ were categorized into non-rich "peripheral" nodes, while those with $k \geq 11$ belonged to rich-club nodes. This classification allowed for the categorization of connections into three subgroups, namely rich-club connections (linking rich club nodes each other), feeder connections (linking rich club nodes to non-rich club nodes), and local connections (linking between only non-rich club nodes). We then computed the group differences of these three-tiered connectivity patterns across MCD groups and controls.

Structural-Functional coupling

All previous metrics were computed at each modality separately. To model a direct relationship between structural and functional network organization, we carried out two post-hoc analyses, namely a *whole-brain* and AAL-based *lobe-wise* (*i.e.*, frontal, parietal, occipital, temporal, limbic cortices and insula) correlation tests between $R_{S\text{-}78}$ and $R_{F\text{-}78}$ matrices of 3T MRI, and compared between controls and each MCD group.

Statistical Analysis

As in previous work [223, 224], analysis was performed separately for each patient group (*i.e.*, FCD, HET and PMG) relative to controls using permutation tests with 1000 repetitions.

a) Inter-regional correlation coefficients.

In each permutation, parcel-wise metrics (*i.e.*, cortical thickness or functional time-series) of a given subject were randomly reassigned to one of the two groups (*i.e.*, each MCD cohort or controls). Correlation matrices in each randomized group were converted to z-scores using Fisher *R-to-Z* transform. We computed the differences of this matrix between the random "MCD" and "control" groups across 1000 times, generating a permutation distribution of between-group differences under the null hypothesis. The true between-group z-score difference was placed in this distribution to obtain the significant level.

b) Graph-theoretical parameters.

Differences in small-world parameters $C, L, \gamma, \lambda, \sigma$ and rich-club coefficient $\phi(k), \phi_{norm}(k)$ together with rich-club, feeder and local connectivity degrees were assessed using an approach

similar to *a)*. Following each random group assignment, we thresholded the correlation matrices and computed the above network parameters. For each parameter, the actual difference between a MCD group and controls was placed in its corresponding permutation distribution to obtain the significance level.

c) Structural-functional coupling.

We directly correlated entries of matrices between structural covariance and functional network using Spearman's rank correlation coefficient at each group. To compare the correlation values between groups (*i.e.*, each patient cohort *vs.* controls), again, permutation tests were employed to provide a null distribution of structural and functional coupling from 1000 random networks, which allowed to compute the statistical significance of a true coupling value by ranking.

d) Correction for multiple comparisons.

We corrected for multiple comparisons using the false discovery rate procedure [194], controlling the proportion of false positive findings to FDR<0.05.

6.4 Results

Structural network alterations

In accordance to our first main hypothesis, covariance analysis revealed that the degree of large-scale network alterations related to core stages during which corticogenesis was mostly disrupted. In fact, MCD subgroups presented with gradual network rearrangements relative to controls across multiple topological parameters, consistently indicating subtle alterations in FCD-II, moderate effects in HET, and most marked changes in PMG.

Specifically, while statistical comparisons of inter-regional thickness correlations between each MCD cohort and controls **(Figure 6.1)** consistently revealed increased intra-hemispheric coupling at the expense of inter-hemispheric covariance in patients (FDR<0.05), changes were subtle in FCD-II, intermediate in HET, and maximal in PMG.

Findings were also complemented by analyses of small-world parameters, namely clustering coefficient (*Cp*) and path length (*Lp),* two indices for network efficiency in terms of brain segregation and integration **(Figure 6.2)**. All MCD subgroups tended towards a more regularized topology with higher *Cp* and *Lp*; findings were again most marked in PMG (p=0.001), and only trending in HET and FCD-II (p<0.08). Notably, a similar gradient was seen on the basis of normalized parameters (where clustering coefficient and path length are normalized with respect to randomly rewired networks, prior to between-group comparisons; FDR<0.05).

Beyond non-specific global effects, we further evaluated MCD-related alterations the so-called *rich club*, an core subgraph composed of central hubs and their mutual interconnections [215] **(Figure 6.3)**. This topology has been shown in structural and functional connectomes, and is thought to form a central high-capacity backbone for integrative communication [218]. While both patient and control cohorts showed a rich-club regime across multiple degree thresholds (*k*=6-13), the former

group revealed markedly decreased rich-club coefficients, compared to the latter. Again, maximal alterations were seen in PMG whereas the other two groups showed milder changes. Notably, disruption were generally related to reduced connectional density among rich-club nodes, and not to that of links between rich-club and non-rich-club nodes (so-called *feeder* links) and links among non-rich-club nodes (so-called *local* links) (FDR<0.05).

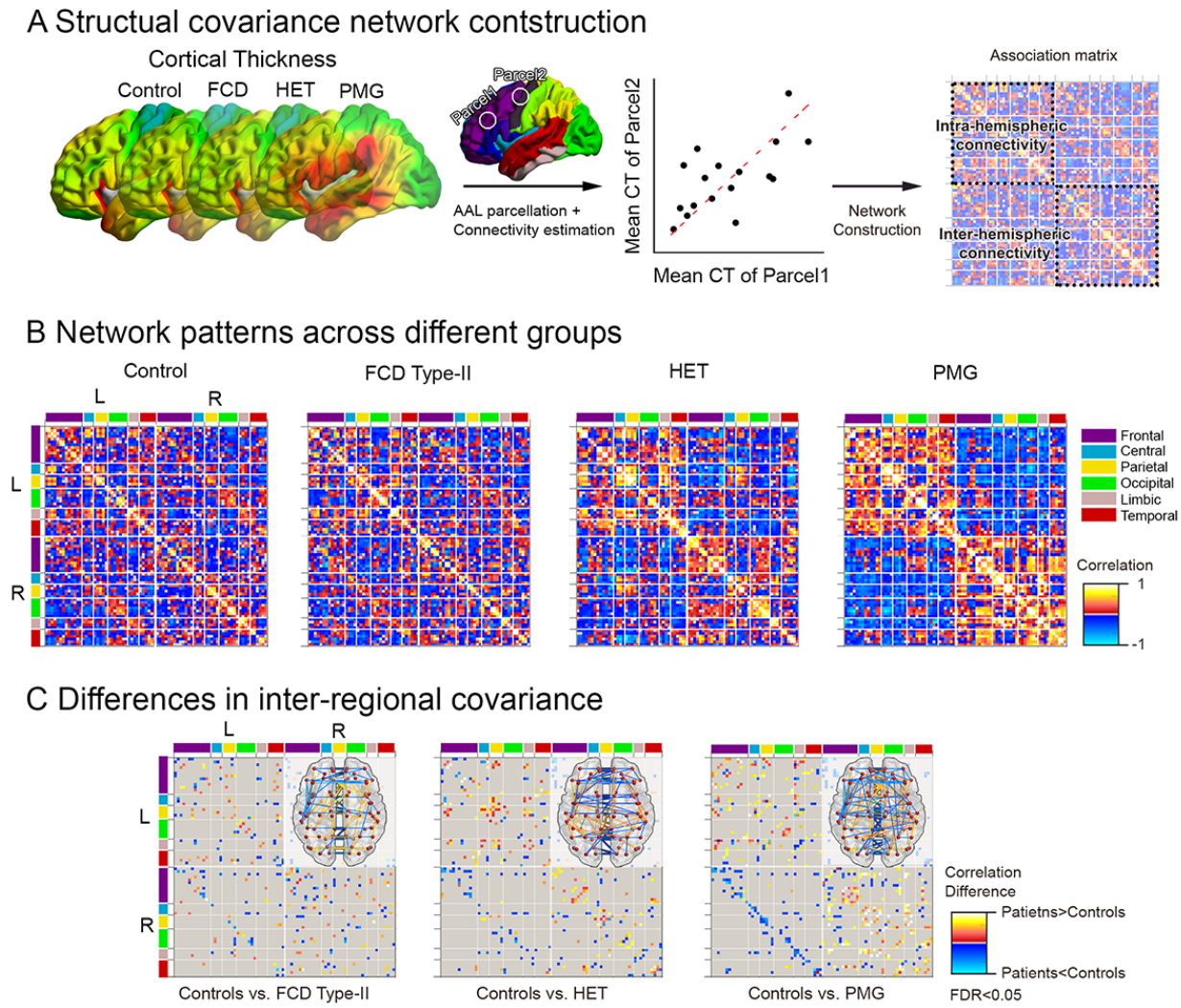

Figure 6.1. Inter-regional covariance and group differences across MCDs. A) The methodological principle of a covariance network construction is shown. A cortical thickness extraction followed by parcel-wise average and their cross-correlation across subjects between a pair of AAL parcels generates a group-wise covariance matrix, the basis of our further analyses. B) Raw patterns are displayed across subjects for controls, Focal Cortical Dysplasia Type-II (FCD-II), heterotopia (HET) and polymicrogyria (PMG). C) Significant group differences in inter-regional correlation. Increase/decrease in patients relative to controls are shown in red/blue, corrected for multiple comparisons at FDR<0.05.

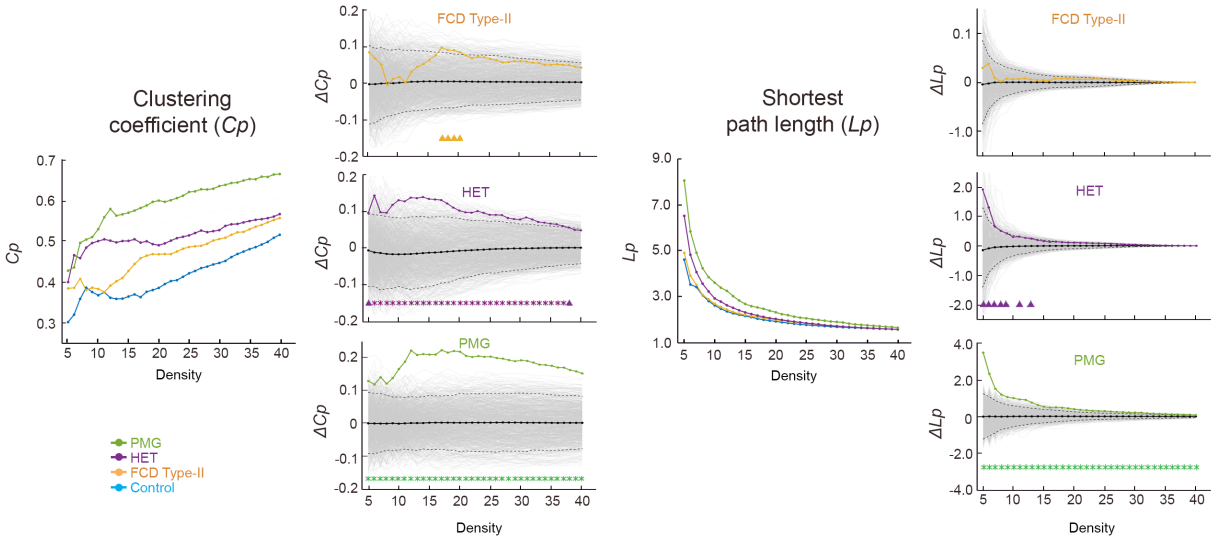

Figure 6.2. Small-world parameters. The patterns of global clustering coefficient (Cp; upper) and shortest path length (Lp; bottom) are shown as a function of network density (5-40%) for each patient cohort and controls. For patient groups, differences of these metrics compared to controls are also presented with same graph details, superimposed on a null distribution derived from non-parametric permutation analysis (gray). Significant group differences were indicated by asterisks (FDR<0.05) and triangles (uncorrected p<0.05).

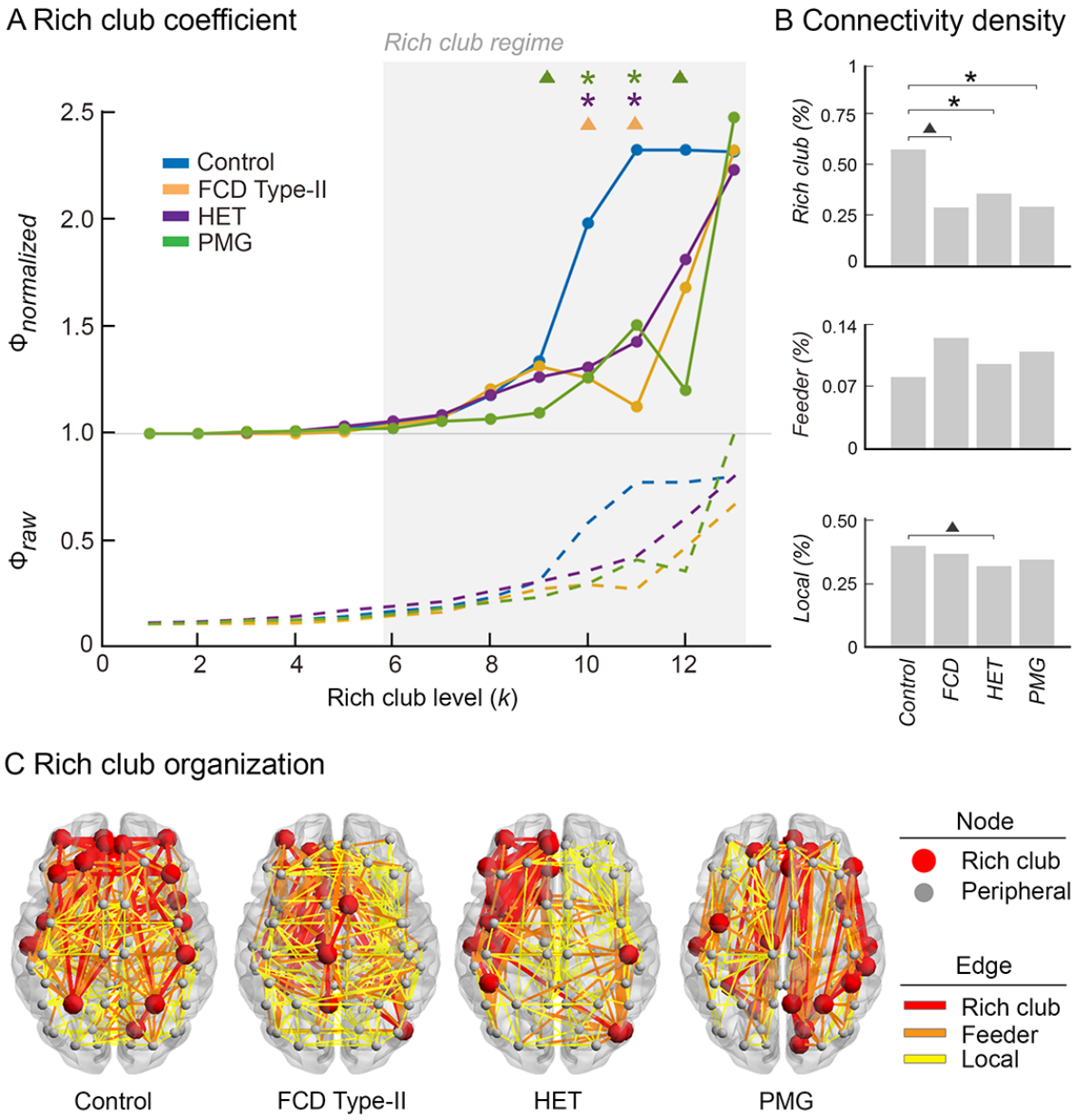

Figure 6.3 See legend on next page.

Figure 6.3. Rich-club organization. A) Rich club coefficient () and its normalized value (with respect to randomly rewired networks is displayed as a function of degree ("rich club level, *k*) across groups. A grey zone indicates the rich-club regime where is positive for a given network. While starts indicate a significant between-group difference relative to controls, corrected at FDR<0.05, triangles note a tendency (uncorrected p<0.05). B) The rich club organization set by *k*=11 (the degree where the control group showed highest rich-club coefficient) allows for categorizing the connectivity into three subgroups, namely rich-club, feeder and local links. See the text for the definition of each subgroup of links. Group differences of connectivity density based on this categorization are shown with same statistical notes as in A). C) The actual nodal organization of this rich club, together with three subgroups of connectivity distribution are visualized with different colors.

Functional network analysis across the spectrum of MCDs

To evaluate our second main hypothesis – whether abnormal properties are equally observed in the functional architecture of MCD patients – we studied same network parameters, analyzing task-free functional imaging data. While marked changes were indeed found in functional networks across MCD groups, their patterns were mainly characterized by a globally inefficient organization (*i.e.*, decreased inter- and intra-hemispheric connectivity, reduced *Cp* and *Lp*, and disrupted rich-club topology; FDR<0.05; **Figure 4AB**) instead of a regularized topology, suggesting diverging phenotypes between structural and functional networks. This pattern was emphasized by the structure-functional coupling analysis (**Figure 4C)**, which demonstrated reduced cross-modal correlations in global connectivity matrices. Again, presumed effects along different malformative onsets were consistently observed, showing most marked structure-function segregation in PMG compared to controls, while HET and FCD-II presented relatively milder reductions (*rho*: 0.26/0.30/0.34/0.36 for PMG/HET /FCD-II/controls; FDR<0.05). Notably, lobe-wise analyses suggested that coupling reductions in HET and PMG were not driven by localized changes in specific anatomical areas, but rather diffusely altered across multiple lobes (FDR<0.05).

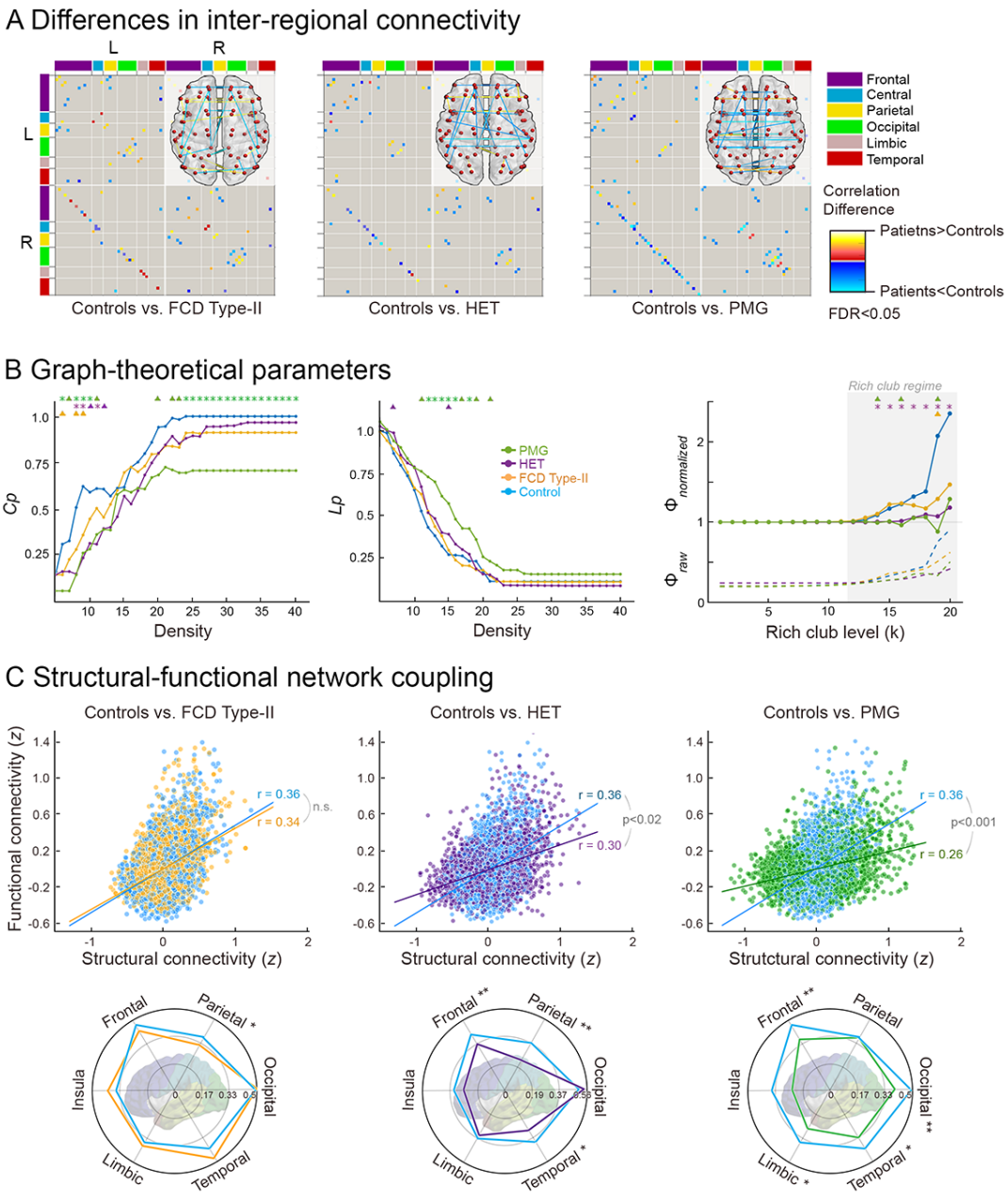

Figure 6.4 See legend on next page.

Figure 6.4. Resting-state functional organization and coupling with structural network. Graph details and statistical indices across A-C) are same as in previous figures. Group differences of A) inter-regional functional connectivity, B) graph-theoretical parameters including small-world and rich-club organization and C) structural-functional network coupling measured by Spearman's rank correlation, both at global and lobe-wise assessment.

Reliability test

a) Parcellation (**Figure 6.5)**. Using an alternative high resolution parcellation, we could verify that our results across all parameters remained virtually identical, with even increased effects sizes.

b) Independent datasets (**Figure 6.6A**). Repeating the structural covariance analyses in an independent dataset scanned at a different field strength that consists of identical spectrum of MCD cohorts (*i.e.*, FCD-II, HET and PMG) revealed highly similar patterns compared to the main analysis.

c) Impact of macroscopic anomalies on network metrics (**Figure 6.6B**). To dispel concerns that high effect sizes in post-migratory MCDs may be largely driven by severely deformed cortices harboring a polymicrogyric lesion, we furthermore analyzed covariance networks in an independent cohort of patients with FCD-I, an MCD currently classified as a post-migratory disorder but does not present with visually appreciable lesions. Compared to controls, FCD-I also displayed robust disruptions across all network parameters, comparable to those seen in PMG.

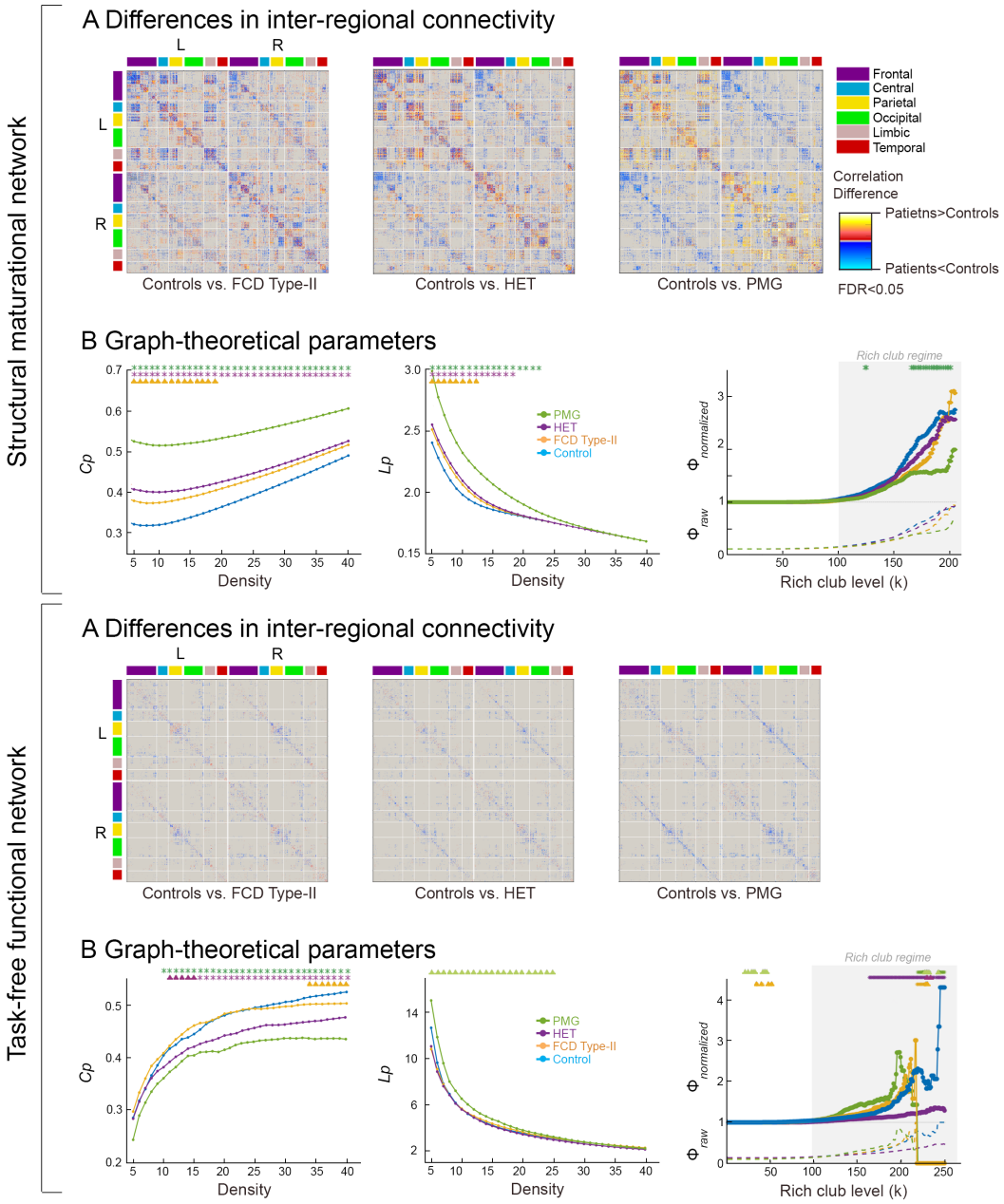

Figure 6.5. See legend on next page.

Figure 6.5. Reliability test for a different scale of parcellation. A high-resolution parcellation was generated based on the previous approach [159]. Briefly, constrained by anatomical boundaries of AAL parcels that consists of 78 different regions of interest, the proposed method subdivided the map into ~1000 parcels through an iterative process such that they gradually form an anatomically meaningful border while maintaining a comparable surface area across parcels. Same analyses (*i.e.*, connectivity comparison, small-world, rich-club analyses) were repeated based on this parcellation both at structural (upper) and functional networks (bottom). Please see figure 1-3 for statistical details.

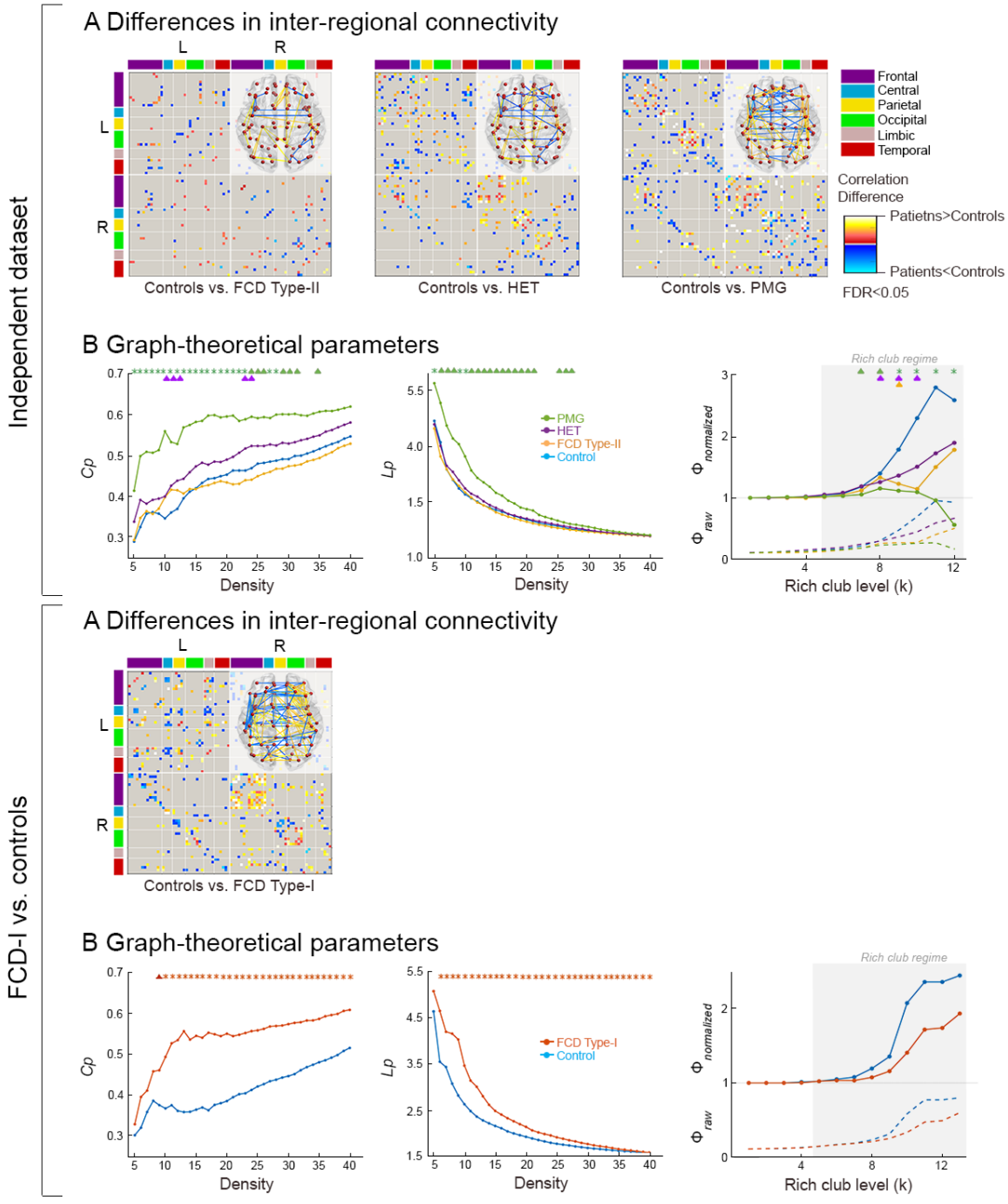

Figure 6.6. See legend on next page.

Figure 6.6. Reliability test for independent datasets. Same analyses (*i.e.*, connectivity comparison, small-world, rich-club analyses) were repeated for structural covariance network, using a new 3T dataset which consists of identical MCD spectrum (*i.e.*, FCD-II, HET and PMG) (upper) and also using a 1.5T data of FCD-I, another MCD cohort related to abnormal post-migratory cortical organization (bottom). Please see figure 1-3 for statistical details.

6.5 Discussion

Ongoing advances in neuroimaging and complex network analysis have fostered a paradigm shift to conceptualize the substrate of numerous developmental diseases, including autism [225], schizophrenia [226], attention-deficit hyperactivity disorder [227], and epilepsy [223, 228]. These accounts increasingly acknowledge a pathological substrate not only characterized by localized abnormalities but additionally by altered connectome organization [229]. By assessing for the first time network-level alterations in patients with malformations with cortical development (MCD), a prevalent condition with congenital anomalies occurring at variable stages of corticogenesis, we were able to systematically assess the impact of malformative timing on large-scale network formation. Comparing graph-theoretical markers derived from MRI structural covariance, a proxy for maturational-developmental structural networks, between our MCD cohorts and controls indicated a consistent direction of topological rearrangement across all MCD subtypes towards a more regularized pattern characterized by increased path length and clustering, as well as disrupted rich club topology. Importantly, effects were most marked in PMG and FCD-I, MCDs thought to relate to a disruption of post-migratory cortical organization, while topology was only marginally affected in malformations such as FCD-II occurring in early, proliferative stages of brain development. These findings provide the first non-invasive demonstration of a gradual impact of malformative timing on the large-scale cortical network organization.

As PMG lesions are radiologically recognized to encompass a rather broad cortical territory, findings in this group could have partially related to the lesional imaging phenotype and not necessarily to malformative timing *per se*. Two separate lines of evidence from our data, however, dispel this concern. First, within the PMG group, we failed to observe a relationship between lesion size and the degree of network anomalies. Second, we observed comparably marked anomalies in FCD-Type I, a subtle lesion that frequently eludes clinical MRI evaluations, than in PMG, both exceeding by far the extent of disruptions seen in patients with HET and FCD Type-II. These findings support the generalization within MCDs that topological impacts on brain network organization may be larger at later than at earlier cortico-genic stages. Research in developmental neurobiology has indeed emphasized a key role of area specialization in late-stage corticogenesis, mainly affected by the formation of cortico-cortical connections [34, 35]. While the early period focuses on the development of major projection fiber tracts (*e.g.*, thalamo-cortical connection), as the mid-late period get closer, the long distance, inter-and intra-hemispheric white matter bundles, namely commissural and cortico-cortical association fibers, are more actively developed, finalizing a large-scale brain network organization [30, 230, 231]. It is thus likely that late-stage disruptions ultimately impact the organization of maturing regions into regional communities, a subnetwork organization thought to play leading role in large-scale topology, dynamics, and adaptability [232-234].

Complimentary analysis of functional networks also revealed a more marked rearrangement of post-migratory compared to early-stage MCDs, validating our main findings using an independent imaging modality and furthermore supporting the general notion that structural networks may largely determine brain function [213]. It is of note, however, that the direction of topological rearrangement was rather different, and not indicative of a regularized configuration (*i.e.*, a

decreased global efficiency together with increased local clustering). Instead, we observed a consistently decreased efficiency, both at the local and global level. On the one hand, decreased structure-function coupling in MCDs compared to controls may indicate a gradual loss of optimal information processing in an increasingly regularized structural network. On the other hand, our findings may also indicate different disease effects on structural-maturational networks, possibly largely determined by genetic contributions and prenatal processes [110, 211], and on functional connectivity, which rather taps into state-based physiological interactions, likely related to comorbid cognitive disabilities [235] often seen in patients with MCDs.

Our findings in MCD may contrast findings in other developmental disorders that posit a gradient in the reverse direction, arguing for rather cumulative effects of early corticogenic disruptions on large-scale brain structure and function. In autism [236] and schizophrenia [237], for example, effects of altered gene expression during early neurodevelopment have been hypothesized to accumulate throughout subsequent corticogenic stages, potentially resulting a more severely affected clinical phenotype. Although the exact mechanism needs further verification, our findings in MCDs suggest a *cascading,* in which an early malformative process may carry on throughout development in a rather selective way without affecting multiple simultaneous processes, thus not necessarily expressing a cumulative *snowball effect* on network formation. To clarify this question, and to establish the role of potentially compensatory processes, however, longitudinal imaging studies during gestational and early postnatal periods in humans at risk and experimental models are recommended.

PART III

CONCLUSIONS

CHAPTER 8

KEY FINDINGS AND SIGNIFICANCE

This dissertation describes a series of advanced multimodal imaging studies that combined a rich array of MRI-based morphometric, diffusion and functional features with recently emerging machine-learning and graph-theoretical paradigms. Applying these novel techniques on patients with MCD, we aimed at comprehensive *in-vivo* assessment of neocortical, subcortical tissue and network-level integrity in both lesional and extralesional areas, and also evaluation of clinical utility of these findings.

PROJECT 1(P.48). This project was targeting currently the most challenging condition in the epilepsy field, namely patients with MRI-negative epileptogenic lesion. By implementing an automated classifier relying on multivariate surface-based features of FCD morphology and intensity, our study provided for the first time Class II evidence that a machine learning framework could accurately identify subtle cortical malformations initially overlooked on routine radiological inspection of 1.5 and 3.0 Tesla scans. Indeed, our approach correctly detected the lesion in 74% of cases while maintaining a relatively high specificity both in controls and patients. Especially, we achieved 100% of specificity in healthy and diseased controls (*i.e.*, no detection of false-positive), suggesting an excellent ability to distinguish between true malformative lesion and non-lesional

healthy cortices. Importantly, the performance of our algorithm showed a high generalizability across different cohorts, scanners and field strengths of MRI.

PROJECT 2 (P.68). Inspired by the finding of extra-lesional clusters in the first project as well as previous case-reports of anomalies extending beyond the lesion, this project carried out the study mapping whole-brain anomalies in the frontal lobe epilepsy patients with the histologically-verified FCD. By evaluating cortical thickness and folding complexity, we found significantly diverging patterns of whole-brain structures between two pathological groups (*i.e.*, FCD Type-I and II). While FCD Type-I displayed multilobar cortical thinning that was most marked in ipsilateral frontal cortices, Type-II showed thickening in temporal and post-central cortices. Cortical folding also diverged, with increased complexity in prefrontal cortices in Type-I and decreases in Type-II. These findings successfully guided automated FCD subtype classification, seizure focus lateralization, and outcome prediction, suggesting a high translational value of group-level assessments in improving individualized diagnostics.

PROJECT 3 (P.87). Contrary to clearly divergent patterns between FCD Type-I and II in the previous project, distinguishing subtype-specific signatures within each group (*e.g.*, between Type-IIA and Type-IIB) has not been demonstrated so far. Here, we designed a comprehensive FCD phenotyping framework based on multi-modal MRI investigations to maximally dissociate subtype-specific features by evaluating markers of morphology, intensity, diffusion, and function across multiple intra- and subcortical surfaces. We indeed identified subtype-specific MRI profiling and were able to accurately predict the histopathological trait already in a pre-operative phase using this profiling features. While FCD Type-IIB revealed abnormal patterns in almost all MRI features across multiple cortical and subcortical surfaces, IIA lesions displayed only subtle increases in FLAIR

signal as well as reduced diffusion anisotropy mainly at the cortico-subcortical interface. Our ability to dissociate FCD subtypes at a mesoscopic level emphasizes the power of image processing applied to widely available clinical 3T MRI.

PROJECT 4 (P.109). We carried out multimodal connectome analyses on a large sample of 154 MCD patients, evaluating comprehensive metrics derived from group-level structural covariance and task-free functional networks. We found that the structural-maturational network of MCDs gradually alters relative to the timing of the underlying malformative process, with the most marked disruption in patients belonging to a disorder of perturbed cortical organization (polymicrogyria), intermediate alterations in those of a failure of cell migration (heterotopia), and subtle changes in those of abnormal neuronal proliferation (focal cortical dysplasia). While the covariance analysis revealed increasing network regularization and rich-club rearrangement, we observed gradually reduced local and global efficiency in functional network. By suggesting progressive structure-function decoupling relative to the malformative onset, our connectome-level phenotyping offers novel perspectives on neurodevelopmental disorders.

Our integrated approach based on multi-modal and multi-compartment, surface-based analysis is designed to statistically model various aspects of pathology that have not been previously assessed on MRI. By combining the approach with pattern-learning paradigms, we demonstrated that advanced multimodal imaging frameworks could maximize the sensitivity to characterize and identify cortical malformations. Beyond focusing the primary lesion, our quantitative evaluation on whole-brain structures and network properties also found novel aspects in relations between structural/functional/organizational phenotypes of MCD-related brain and underlying pathology,

emphasizing the power of MRI post-processing that can extract a critical information from high-dimensional imaging datasets. The proposed methods together with our findings will provide a new avenue to better understand fundamental pathological mechanisms related to MCD, and clinically improve lesion detection and treatment strategies in this disease.

* * *

PART IV

BIBLIOGRAPHY

1. Lenroot RK, Giedd JN. Brain development in children and adolescents: insights from anatomical magnetic resonance imaging. Neurosci Biobehav R 2006;30:718-729.

2. Barkovich A, Guerrini R, Kuzniecky R, Jackson G, Dobyns W. A developmental and genetic classification for malformations of cortical development: update 2012. Brain : a journal of neurology 2012;135:1348-1369.

3. Lerner JT, Salamon N, Hauptman JS, et al. Assessment and surgical outcomes for mild type I and severe type II cortical dysplasia: a critical review and the UCLA experience. Epilepsia 2009;50:1310-1335.

4. Wiebe S, Blume WT, Girvin JP, Eliasziw M, Effectiveness, Efficiency of Surgery for Temporal Lobe Epilepsy Study G. A randomized, controlled trial of surgery for temporal-lobe epilepsy. The New England journal of medicine 2001;345:311-318.

5. Fauser S, Schulze-Bonhage A, Honegger J, et al. Focal cortical dysplasias: surgical outcome in 67 patients in relation to histological subtypes and dual pathology. Brain : a journal of neurology 2004;127:2406-2418.

6. Colombo N, Salamon N, Raybaud C, Ozkara C, Barkovich AJ. Imaging of malformations of cortical development. Epileptic disorders : international epilepsy journal with videotape 2009;11:194-205.

7. Sisodiya SM, Fauser S, Cross JH, Thom M. Focal cortical dysplasia type II: biological features and clinical perspectives. Lancet Neurol 2009;8:830-843.

8. Bernasconi A, Bernasconi N, Bernhardt BC, Schrader D. Advances in MRI for 'cryptogenic' epilepsies. Nature reviews Neurology 2011;7:99-108.

9. McGonigal A, Bartolomei F, Regis J, et al. Stereoelectroencephalography in presurgical assessment of MRI-negative epilepsy. Brain : a journal of neurology 2007;130:3169-3183.

10. Bien CG, Szinay M, Wagner J, Clusmann H, Becker AJ, Urbach H. Characteristics and surgical outcomes of patients with refractory magnetic resonance imaging-negative epilepsies. Archives of neurology 2009;66:1491-1499.

11. Barazany D, Assaf Y. Visualization of Cortical Lamination Patterns with Magnetic Resonance Imaging. Cerebral Cortex 2012;22:2016-2023.

12. Nelson F, Datta S, Garcia N, et al. Intracortical lesions by 3T magnetic resonance imaging and correlation with cognitive impairment in multiple sclerosis. Mult Scler 2011;17:1122-1129.

13. Hodozuka A, Tsuda H, Hashizume K, Tanaka T. Focal cortical dysplasia: pathophysiological approach. Child's nervous system : ChNS : official journal of the International Society for Pediatric Neurosurgery 2006;22:827-833.

14. Cohen-Gadol AA, Ozduman K, Bronen RA, Kim JH, Spencer DD. Long-term outcome after epilepsy surgery for focal cortical dysplasia. J Neurosurg 2004;101:55-65.

15. Ferrier CH, Alarcon G, Engelsman J, et al. Relevance of residual histologic and electrocorticographic abnormalities for surgical outcome in frontal lobe epilepsy. Epilepsia 2001;42:363-371.

16. Bonilha L, Montenegro MA, Rorden C, et al. Voxel-based morphometry reveals excess gray matter concentration in patients with focal cortical dysplasia. Epilepsia 2006;47:908-915.

17. Richardson MP, Friston KJ, Sisodiya SM, et al. Cortical grey matter and benzodiazepine receptors in malformations of cortical development. A voxel-based comparison of structural and functional imaging data. Brain : a journal of neurology 1997;120 (Pt 11):1961-1973.

18. Fauser S, Sisodiya SM, Martinian L, et al. Multi-focal occurrence of cortical dysplasia in epilepsy patients. Brain : a journal of neurology 2009;132:2079-2090.

19. Krsek P, Pieper T, Karlmeier A, et al. Different presurgical characteristics and seizure outcomes in children with focal cortical dysplasia type I or II. Epilepsia 2009;50:125-137.

20. Janszky J, Ebner A, Kruse B, et al. Functional organization of the brain with malformations of cortical development. Annals of neurology 2003;53:759-767.

21. Rakic P. Evolution of the neocortex: a perspective from developmental biology. Nat Rev Neurosci 2009;10:724-735.

22. Bystron I, Blakemore C, Rakic P. Development of the human cerebral cortex: Boulder Committee revisited. Nat Rev Neurosci 2008;9:110-122.

23. Lui JH, Hansen DV, Kriegstein AR. Development and evolution of the human neocortex. Cell 2011;146:18-36.

24. Iacopetti P, Michelini M, Stuckmann I, Oback B, Aaku-Saraste E, Huttner WB. Expression of the antiproliferative gene TIS21 at the onset of neurogenesis identifies single neuroepithelial cells that switch from proliferative to neuron-generating division. Proceedings of the National Academy of Sciences of the United States of America 1999;96:4639-4644.

25. Pontious A, Kowalczyk T, Englund C, Hevner RF. Role of intermediate progenitor cells in cerebral cortex development. Developmental neuroscience 2008;30:24-32.

26. Noctor SC, V M-C, Ivic L, Kriegstein AR. Cortical neurons arise in symmetric and asymmetric division zones and migrate through specific phases. Nature neuroscience 2004;7:136-144.

27. Haubensak W, Attardo A, Denk W, Huttner WB. Neurons arise in the basal neuroepithelium of the early mammalian telencephalon: A major site of neurogenesis. Proceedings of the National Academy of Sciences of the United States of America 2004;101:3196-3201.

28. Sidman RL, Rakic P. Neuronal migration, with special reference to developing human brain: a review. Brain Res 1973;62:1-35.

29. Zecevic N, Chen Y, Filipovic R. Contributions of cortical subventricular zone to the development of the human cerebral cortex. The Journal of comparative neurology 2005;491:109-122.

30. Budday S, Steinmann P, Kuhl E. Physical biology of human brain development. Front Cell Neurosci 2015;9:257.

31. Marin O, Rubenstein JL. Cell migration in the forebrain. Annual review of neuroscience 2003;26:441-483.

32. Nadarajah B, Parnavelas JG. Modes of neuronal migration in the developing cerebral cortex. Nat Rev Neurosci 2002;3:423-432.

33. Hansen DV, Lui JH, Flandin P, et al. Non-epithelial stem cells and cortical interneuron production in the human ganglionic eminences. Nature neuroscience 2013;16:1576-1587.

34. Sur M, Rubenstein JLR. Patterning and plasticity of the cerebral cortex. Science 2005;310:805-810.

35. O'Leary DDM, Chou SJ, Sahara S. Area patterning of the mammalian cortex. Neuron 2007;56:252-269.

36. Oleary DDM. Do Cortical Areas Emerge from a Protocortex. Trends in neurosciences 1989;12:400-406.

37. Rakic P. Specification of cerebral cortical areas. Science 1988;241:170-176.

38. Forster E, Jossin Y, Zhao ST, Chai XJ, Frotscher M, Goffinet AM. Recent progress in understanding the role of Reelin in radial neuronal migration, with specific emphasis on the dentate gyrus. European Journal of Neuroscience 2006;23:901-909.

39. Molyneaux BJ, Arlotta P, Menezes JR, Macklis JD. Neuronal subtype specification in the cerebral cortex. Nat Rev Neurosci 2007;8:427-437.

40. Poulain FE, Sobel A. The microtubule network and neuronal morphogenesis: Dynamic and coordinated orchestration through multiple players. Mol Cell Neurosci 2010;43:15-32.

41. Dekkers MPJ, Nikoletopoulou V, Barde YA. Death of developing neurons: New insights and implications for connectivity. Journal of Cell Biology 2013;203:385-393.

42. Leventer RJ, Guerrini R, Dobyns WB. Malformations of cortical development and epilepsy. Dialogues in clinical neuroscience 2008;10:47-62.

43. Kuzniecky RI, Jackson GD. Magnetic Resonance in Epilepsy: Raven Press, 1995.

44. Sutula TP, Hagen J, Pitkanen A. Do epileptic seizures damage the brain? Curr Opin Neurol 2003;16:189-195.

45. Begley CE, Beghi E, Beran RG, et al. ILAE Commission on the Burden of Epilepsy, Subcommission on the Economic Burden of Epilepsy: Final report 1998-2001. Epilepsia 2002;43:668-673.

46. Wiebe S. Burden of intractable epilepsy. Advances in neurology 2006;97:1-4.

47. Kuzniecky R. Epilepsy and malformations of cortical development: new developments. Curr Opin Neurol 2015;28:151-157.

48. Barkovich AJ, Guerrini R, Kuzniecky RI, Jackson GD, Dobyns WB. A developmental and genetic classification for malformations of cortical development: update 2012. Brain : a journal of neurology 2012;135:1348-1369.

49. Blumcke I, Vinters HV, Armstrong D, Aronica E, Thom M, Spreafico R. Malformations of cortical development and epilepsies: neuropathological findings with emphasis on focal cortical dysplasia. Epileptic disorders : international epilepsy journal with videotape 2009;11:181-193.

50. Guerrini R, Dobyns WB. Malformations of cortical development: clinical features and genetic causes. Lancet Neurol 2014;13:710-726.

51. Papayannis CE, Consalvo D, Kauffman MA, et al. Malformations of cortical development and epilepsy in adult patients. Seizure : the journal of the British Epilepsy Association 2012;21:377-384.

52. Pang T, Atefy R, Sheen V. Malformations of cortical development. Neurologist 2008;14:181-191.

53. Chang B, Walsh CA, Apse K, Bodell A. Polymicrogyria Overview. In: Pagon RA, Adam MP, Ardinger HH, et al., eds. GeneReviews(R). Seattle (WA)1993.

54. Leventer RJ, Phelan EM, Coleman LT, Kean MJ, Jackson GD, Harvey AS. Clinical and imaging features of cortical malformations in childhood. Neurology 1999;53:715-722.

55. Barkovich AJ. Current concepts of polymicrogyria. Neuroradiology 2010;52:479-487.

56. Barkovich AJ. Morphologic characteristics of subcortical heterotopia: MR imaging study. AJNR American journal of neuroradiology 2000;21:290-295.

57. Donkol RH, Moghazy KM, Abolenin A. Assessment of gray matter heterotopia by magnetic resonance imaging. World J Radiol 2012;4:90-96.

58. Kobayashi E, Bagshaw AP, Grova C, Gotman J, Dubeau F. Grey matter heterotopia: what EEG-fMRI can tell us about epileptogenicity of neuronal migration disorders. Brain : a journal of neurology 2006;129:366-374.

59. Sisodiya SM. Malformations of cortical development: burdens and insights from important causes of human epilepsy. Lancet Neurol 2004;3:29-38.

60. Blumcke I, Thom M, Aronica E, et al. The clinicopathologic spectrum of focal cortical dysplasias: a consensus classification proposed by an ad hoc Task Force of the ILAE Diagnostic Methods Commission. Epilepsia 2011;52:158-174.

61. Hildebrandt M, Pieper T, Winkler P, Kolodziejczyk D, Holthausen H, Blumcke I. Neuropathological spectrum of cortical dysplasia in children with severe focal epilepsies. Acta Neuropathol 2005;110:1-11.

62. Muhlebner A, Coras R, Kobow K, et al. Neuropathologic measurements in focal cortical dysplasias: validation of the ILAE 2011 classification system and diagnostic implications for MRI. Acta Neuropathol 2011.

63. Urbach H, Scheffler B, Heinrichsmeier T, et al. Focal cortical dysplasia of Taylor's balloon cell type: a clinicopathological entity with characteristic neuroimaging and histopathological features, and favorable postsurgical outcome. Epilepsia 2002;43:33-40.

64. Cepeda C, Hurst RS, Flores-Hernandez J, et al. Morphological and electrophysiological characterization of abnormal cell types in pediatric cortical dysplasia. Journal of neuroscience research 2003;72:472-486.

65. Marin-Valencia I, Guerrini R, Gleeson JG. Pathogenetic mechanisms of focal cortical dysplasia. Epilepsia 2014;55:970-978.

66. De Ciantis A, Barkovich AJ, Cosottini M, et al. Ultra-High-Field MR Imaging in Polymicrogyria and Epilepsy. Am J Neuroradiol 2015;36:309-316.

67. Krsek P, Maton B, Korman B, et al. Different features of histopathological subtypes of pediatric focal cortical dysplasia. Annals of neurology 2008;63:758-769.

68. Colombo N, Tassi L, Deleo F, et al. Focal cortical dysplasia type IIa and IIb: MRI aspects in 118 cases proven by histopathology. Neuroradiology 2012;54:1065-1077.

69. Krsek P, Maton B, Jayakar P, et al. Incomplete resection of focal cortical dysplasia is the main predictor of poor postsurgical outcome. Neurology 2009;72:217-223.

70. de Lanerolle NC, Kim JH, Williamson A, et al. A retrospective analysis of hippocampal pathology in human temporal lobe epilepsy: evidence for distinctive patient subcategories. Epilepsia 2003;44:677-687.

71. Hauptman JS, Mathern GW. Surgical treatment of epilepsy associated with cortical dysplasia: 2012 update. Epilepsia 2012;53 Suppl 4:98-104.

72. Barkovich AJ, Guerrini R, Kuzniecky RI, Jackson GD, Dobyns WB. A developmental and genetic classification for malformations of cortical development: update 2012. Brain : a journal of neurology 2012;135:1348-1369.

73. Ashburner J, Friston KJ. Voxel-based morphometry--the methods. NeuroImage 2000;11:805-821.

74. Bernasconi A, Bernasconi N, Bernhardt BC, Schrader D. Advances in MRI for 'cryptogenic' epilepsies. Nature reviews Neurology 2011;7:99-108.

75. Colliot O, Bernasconi N, Khalili N, Antel SB, Naessens V, Bernasconi A. Individual voxel-based analysis of gray matter in focal cortical dysplasia. Neuroimage 2006;29:162-171.

76. Rugg-Gunn FJ, Boulby PA, Symms MR, Barker GJ, Duncan JS. Whole-brain T2 mapping demonstrates occult abnormalities in focal epilepsy. Neurology 2005;64:318-325.

77. Rugg-Gunn FJ, Eriksson SH, Boulby PA, Symms MR, Barker GJ, Duncan JS. Magnetization transfer imaging in focal epilepsy. Neurology 2003;60:1638-1645.

78. Focke NK, Symms MR, Burdett JL, Duncan JS. Voxel-based analysis of whole brain FLAIR at 3T detects focal cortical dysplasia. Epilepsia 2008;49:783-793.

79. Salmenpera TM, Symms MR, Rugg-Gunn FJ, et al. Evaluation of quantitative magnetic resonance imaging contrasts in MRI-negative refractory focal epilepsy. Epilepsia 2007;48:229-237.

80. Bernasconi A, Antel SB, Collins DL, et al. Texture analysis and morphological processing of magnetic resonance imaging assist detection of focal cortical dysplasia in extra-temporal partial epilepsy. Annals of neurology 2001;49:770-775.

81. Antel SB, Collins DL, Bernasconi N, et al. Automated detection of focal cortical dysplasia lesions using computational models of their MRI characteristics and texture analysis. NeuroImage 2003;19:1748-1759.

82. Antel SB, Bernasconi A, Bernasconi N, et al. Computational models of MRI characteristics of focal cortical dysplasia improve lesion detection. Neuroimage 2002;17:1755-1760.

83. Huppertz HJ, Grimm C, Fauser S, et al. Enhanced visualization of blurred gray-white matter junctions in focal cortical dysplasia by voxel-based 3D MRI analysis. Epilepsy Res 2005;67:35-50.

84. Colliot O, Mansi T, Bernasconi N, Naessens V, Klironomos D, Bernasconi A. Segmentation of focal cortical dysplasia lesions using a feature-based level set. Medical image computing and computer-assisted intervention : MICCAI International Conference on Medical Image Computing and Computer-Assisted Intervention 2005;8:375-382.

85. Ashburner J, Friston KJ. Why voxel-based morphometry should be used. NeuroImage 2001;14:1238-1243.

86. Bookstein FL. "Voxel-based morphometry" should not be used with imperfectly registered images. NeuroImage 2001;14:1454-1462.

87. Tisserand DJ, Pruessner JC, Arigita EJS, et al. Regional frontal cortical volumes decrease differentially in aging: An MRI study to compare volumetric approaches and voxel-based morphometry. NeuroImage 2002;17:657-669.

88. MacDonald D, Kabani N, Avis D, Evans AC. Automated 3-D extraction of inner and outer surfaces of cerebral cortex from MRI. NeuroImage 2000;12:340-356.

89. Dale AM, Fischl B, Sereno MI. Cortical surface-based analysis. I. Segmentation and surface reconstruction. NeuroImage 1999;9:179-194.

90. Kim JS, Singh V, Lee JK, et al. Automated 3-D extraction and evaluation of the inner and outer cortical surfaces using a Laplacian map and partial volume effect classification. Neuroimage 2005;27:210-221.

91. Sled JG, Zijdenbos AP, Evans AC. A nonparametric method for automatic correction of intensity nonuniformity in MRI data. IEEE transactions on medical imaging 1998;17:87-97.

92. Collins DL, Neelin P, Peters TM, Evans AC. Automatic 3D intersubject registration of MR volumetric data in standardized Talairach space. Journal of computer assisted tomography 1994;18:192-205.

93. Zijdenbos A, Forghani R, Evans A. Automatic quantification of MS lesions in 3D MRI brain data sets: Validation of INSECT. Lect Notes Comput Sc 1998;1496:439-448.

94. Kim H, Caldairou B, Hwang JW, et al. Accurate cortical tissue classification on MRI by modeling cortical folding patterns. Human brain mapping 2015.

95. Tohka J, Zijdenbos A, Evans A. Fast and robust parameter estimation for statistical partial volume models in brain MRI. NeuroImage 2004;23:84-97.

96. Lyttelton O, Boucher M, Robbins S, Evans A. An unbiased iterative group registration template for cortical surface analysis. NeuroImage 2007;34:1535-1544.

97. Robbins S, Evans AC, Collins DL, Whitesides S. Tuning and comparing spatial normalization methods. Medical image analysis 2004;8:311-323.

98. Ghosh SS, Kakunoori S, Augustinack J, et al. Evaluating the validity of volume-based and surface-based brain image registration for developmental cognitive neuroscience studies in children 4 to 11 years of age. NeuroImage 2010;53:85-93.

99. Besson P, Andermann F, Dubeau F, Bernasconi A. Small focal cortical dysplasia lesions are located at the bottom of a deep sulcus. Brain : a journal of neurology 2008;131:3246-3255.

100. Mellerio C, Roca P, Chassoux F, et al. The power button sign: a newly described central sulcal pattern on surface rendering MR images of type 2 focal cortical dysplasia. Radiology 2015;274:500-507.

101. Roca P, Mellerio C, Chassoux F, et al. Sulcus-based MR analysis of focal cortical dysplasia located in the central region. PloS one 2015;10:e0122252.

102. Regis J, Tamura M, Park MC, et al. Subclinical Abnormal Gyration Pattern, a Potential Anatomic Marker of Epileptogenic Zone in Patients With Magnetic Resonance Imaging-Negative Frontal Lobe Epilepsy. Neurosurgery 2011;69:80-93.

103. Blackmon K, Kuzniecky R, Barr WB, et al. Cortical Gray-White Matter Blurring and Cognitive Morbidity in Focal Cortical Dysplasia. Cereb Cortex 2014.

104. Duchowny M. Clinical, functional, and neurophysiologic assessment of dysplastic cortical networks: Implications for cortical functioning and surgical management. Epilepsia 2009;50 Suppl 9:19-27.

105. Alexander-Bloch A, Raznahan A, Bullmore E, Giedd J. The Convergence of Maturational Change and Structural Covariance in Human Cortical Networks. Journal of Neuroscience 2013;33:2889-+.

106. Bernhardt BC, Worsley KJ, Besson P, et al. Mapping limbic network organization in temporal lobe epilepsy using morphometric correlations: insights on the relation between mesiotemporal connectivity and cortical atrophy. NeuroImage 2008;42:515-524.

107. Bernhardt BC, Chen Z, He Y, Evans AC, Bernasconi N. Graph-theoretical analysis reveals disrupted small-world organization of cortical thickness correlation networks in temporal lobe epilepsy. Cereb Cortex 2011;21:2147-2157.

108. Bullmore ET, Woodruff PWR, Wright IC, et al. Does dysplasia cause anatomical dysconnectivity in schizophrenia? Schizophrenia research 1998;30:127-135.

109. Lerch JP, Worsley K, Shaw WP, et al. Mapping anatomical correlations across cerebral cortex (MACACC) using cortical thickness from MRI. NeuroImage 2006;31:993-1003.

110. Alexander-Bloch A, Giedd JN, Bullmore ET. Imaging structural co-variance between human brain regions. Nat Rev Neurosci 2013;14:322-336.

111. Alexander-Bloch A, Giedd JN, Bullmore E. Imaging structural co-variance between human brain regions. Nat Rev Neurosci 2013.

112. Rimol LM, Panizzon MS, Fennema-Notestine C, et al. Cortical Thickness Is Influenced by Regionally Specific Genetic Factors. Biol Psychiat 2010;67:493-499.

113. Schmitt JE, Lenroot RK, Wallace GL, et al. Identification of genetically mediated cortical networks: a multivariate study of pediatric twins and siblings. Cereb Cortex 2008;18:1737-1747.

114. Khundrakpam BS, Reid A, Brauer J, et al. Developmental Changes in Organization of Structural Brain Networks. Cereb Cortex 2012.

115. He Y, Chen ZJ, Evans AC. Small-world anatomical networks in the human brain revealed by cortical thickness from MRI. Cerebral Cortex 2007;17:2407-2419.

116. Yuan WH, Szaflarski JP, Schmithorst VJ, et al. fMRI shows atypical language lateralization in pediatric epilepsy patients. Epilepsia 2006;47:593-600.

117. Gaillard WD, Berl MM, Moore EN, et al. Atypical language in lesional and nonlesional complex partial epilepsy. Neurology 2007;69:1761-1771.

118. Sethi M, Pedersen M, Jackson GD. Polymicrogyric Cortex may Predispose to Seizures via Abnormal Network Topology: An fMRI Connectomics Study. Epilepsia 2016;57:e64-e68.

119. Jeong W, Jin SH, Kim M, Kim JS, Chung CK. Abnormal functional brain network in epilepsy patients with focal cortical dysplasia. Epilepsy Res 2014;108:1618-1626.

120. Christodoulou JA, Walker LM, Del Tufo SN, et al. Abnormal structural and functional brain connectivity in gray matter heterotopia. Epilepsia 2012;53:1024-1032.

121. Archer JS, Abbott DF, Masterton RAJ, Palmer SM, Jackson GD. Functional MRI interactions between dysplastic nodules and overlying cortex in periventricular nodular heterotopia. Epilepsy & Behavior 2010;19:631-634.

122. Christodoulou JA, Barnard ME, Del Tufo SN, et al. Integration of gray matter nodules into functional cortical circuits in periventricular heterotopia. Epilepsy & Behavior 2013;29:400-406.

123. Shafi MM, Vernet M, Klooster D, et al. Physiological Consequences of Abnormal Connectivity in a Developmental Epilepsy. Annals of neurology 2015;77:487-503.

124. Muhlebner A, Coras R, Kobow K, et al. Neuropathologic measurements in focal cortical dysplasias: validation of the ILAE 2011 classification system and diagnostic implications for MRI. Acta neuropathologica 2012;123:259-272.

125. Thesen T, Quinn BT, Carlson C, et al. Detection of epileptogenic cortical malformations with surface-based MRI morphometry. PloS one 2011;6:e16430.

126. Huppertz HJ, Kurthen M, Kassubek J. Voxel-based 3D MRI analysis for the detection of epileptogenic lesions at single subject level. Epilepsia 2009;50:155-156.

127. Wilke M, Kassubek J, Ziyeh S, Schulze-Bonhage A, Huppertz HJ. Automated detection of gray matter malformations using optimized voxel-based morphometry: a systematic approach. NeuroImage 2003;20:330-343.

128. Kassubek J, Huppertz HJ, Spreer J, Schulze-Bonhage A. Detection and localization of focal cortical dysplasia by voxel-based 3-D MRI analysis. Epilepsia 2002;43:596-602.

129. Raymond AA, Fish DR, Sisodiya SM, Alsanjari N, Stevens JM, Shorvon SD. Abnormalities of gyration, heterotopias, tuberous sclerosis, focal cortical dysplasia, microdysgenesis, dysembryoplastic neuroepithelial tumor and dysgenesis of archicortex in epilepsy. Clinical, EEG and neuroimaging features in 100 adult patients. Brain 1995;118:629-660.

130. Sica GT. Bias in research studies. Radiology 2006;238:780-789.

131. Ashman EJ, Gronseth GS. Level of evidence reviews: three years of progress. Neurology 2012;79:13-14.

132. Engel J, Jr., Van Ness PC, Rasmussen T, Ojemann LM. Outcome with respect to epileptic seizures. In: Engel J, Jr., ed. Surgical treatment of the epilepsies, 2nd ed. New York: Raven, 1993: 609-621.

133. Sled JG, Zijdenbos AP, Evans AC. A nonparametric method for automatic correction of intensity nonuniformity in MRI data. IEEE Trans Med Imaging 1998;17:87-97.

134. Zijdenbos AP, Forghani R, Evans AC. Automatic quantification of ms lesions in 3D MRI brain data sets: validation of INSECT. Med Image Comput Comput Assist Interv 1998:439-448.

135. Im K, Lee JM, Lyttelton O, Kim SH, Evans AC, Kim SI. Brain size and cortical structure in the adult human brain. Cerebral cortex 2008;18:2181-2191.

136. Colliot O, Mansi T, Bernasconi N, Naessens V, Klironomos D, Bernasconi A. Segmentation of focal cortical dysplasia lesions on MRI using level set evolution. Neuroimage 2006;32:1621-1630.

137. Duda RO, Hart PE, Stork DG. Pattern Classification (2nd Edition): Wiley-Interscience, 2000.

138. Tzourio-Mazoyer N, Landeau B, Papathanassiou D, et al. Automated anatomical labeling of activations in SPM using a macroscopic anatomical parcellation of the MNI MRI single-subject brain. Neuroimage 2002;15:273-289.

139. Eriksson SH, Thom M, Symms MR, et al. Cortical neuronal loss and hippocampal sclerosis are not detected by voxel-based morphometry in individual epilepsy surgery patients. Human brain mapping 2009;30:3351-3360.

140. Wang S, Summers RM. Machine learning and radiology. Medical Image Analysis 2012;16:933-951.

141. Taylor DC, Falconer MA, Bruton CJ, Corsellis JAN. Focal dysplasia of the cerebral cortex in epilepsy. J Neurol Neurosurg Psychiatry 1971;34:369-387.

142. Bronen RA, Spencer DD, Fulbright RK. Cerebrospinal fluid cleft with cortical dimple: MR imaging marker for focal cortical dysgenesis. Radiology 2000;214:657-663.

143. Usui N, Matsuda K, Mihara T, et al. MRI of cortical dysplasia--correlation with pathological findings. Neuroradiology 2001;43:830-837.

144. Sisodiya SM, Free SL. Disproportion of cerebral surface areas and volumes in cerebral dysgenesis. MRI-based evidence for connectional abnormalities. Brain : a journal of neurology 1997;120 (Pt 2):271-281.

145. Lee SK, Kim DI, Mori S, et al. Diffusion tensor MRI visualizes decreased subcortical fiber connectivity in focal cortical dysplasia. Neuroimage 2004;22:1826-1829.

146. Thom M, Martinian L, Sen A, Cross JH, Harding BN, Sisodiya SM. Cortical neuronal densities and lamination in focal cortical dysplasia. Acta neuropathologica 2005;110:383-392.

147. Lu YB, Franze K, Seifert G, et al. Viscoelastic properties of individual glial cells and neurons in the CNS. Proceedings of the National Academy of Sciences of the United States of America 2006;103:17759-17764.

148. Tellez-Zenteno JF, Hernandez Ronquillo L, Moien-Afshari F, Wiebe S. Surgical outcomes in lesional and non-lesional epilepsy: a systematic review and meta-analysis. Epilepsy research 2010;89:310-318.

149. Hong SJ, Kim H, Schrader D, Bernasconi N, Bernhardt BC, Bernasconi A. Automated detection of cortical dysplasia type II in MRI-negative epilepsy. Neurology 2014.

150. Fonseca Vde C, Yasuda CL, Tedeschi GG, Betting LE, Cendes F. White matter abnormalities in patients with focal cortical dysplasia revealed by diffusion tensor imaging analysis in a voxelwise approach. Front Neurol 2012;3:121.

151. Keller SS, Roberts N. Voxel-based morphometry of temporal lobe epilepsy: An introduction and review of the literature. Epilepsia 2008;49:741-757.

152. Bernhardt BC, Hong S, Bernasconi A, Bernasconi N. Imaging structural and functional brain networks in temporal lobe epilepsy. Frontiers in human neuroscience 2013;7:624.

153. Kriegeskorte N, Goebel R, Bandettini P. Information-based functional brain mapping. Proceedings of the National Academy of Sciences of the United States of America 2006;103:3863-3868.

154. Bernhardt BC, Worsley KJ, Kim H, Evans AC, Bernasconi A, Bernasconi N. Longitudinal and cross-sectional analysis of atrophy in pharmacoresistant temporal lobe epilepsy. Neurology 2009;72:1747-1754.

155. Voets NL, Bernhardt BC, Kim H, Yoon U, Bernasconi N. Increased temporolimbic cortical folding complexity in temporal lobe epilepsy. Neurology 2011;76:138-144.

156. Bernhardt BC, Bernasconi N, Concha L, Bernasconi A. Cortical thickness analysis in temporal lobe epilepsy: reproducibility and relation to outcome. Neurology 2010;74:1776-1784.

157. Worsley K, Taylor J, Carbonell F, et al. SurfStat: A Matlab toolbox for the statistical analysis of univariate and multivariate surface and volumetric data using linear mixed effects models and random field theory. NeuroImage, OHBM poster 2009.

158. Glasser MF, Van Essen DC. Mapping human cortical areas in vivo based on myelin content as revealed by T1- and T2-weighted MRI. The Journal of neuroscience : the official journal of the Society for Neuroscience 2011;31:11597-11616.

159. Cammoun L, Gigandet X, Meskaldji D, et al. Mapping the human connectome at multiple scales with diffusion spectrum MRI. Journal of neuroscience methods 2012;203:386-397.

160. Worsley K, Andermann M, Koulis T, MacDonald D, Evans A. Detecting changes in nonisotropic images. Human brain mapping 1999;8:98-101.

161. Bonilha L, Rorden C, Appenzeller S, Coan AC, Cendes F, Li LM. Gray matter atrophy associated with duration of temporal lobe epilepsy. NeuroImage 2006;32:1070-1079.

162. Bernhardt BC, Rozen DA, Worsley KJ, Evans AC, Bernasconi N, Bernasconi A. Thalamo-cortical network pathology in idiopathic generalized epilepsy: insights from MRI-based morphometric correlation analysis. Neuroimage 2009;46:373-381.

163. Blumenfeld H. From molecules to networks: cortical/subcortical interactions in the pathophysiology of idiopathic generalized epilepsy. Epilepsia 2003;44 Suppl 2:7-15.

164. Casillas-Espinosa PM, Powell KL, O'Brien TJ. Regulators of synaptic transmission: roles in the pathogenesis and treatment of epilepsy. Epilepsia 2012;53 Suppl 9:41-58.

165. Tau GZ, Peterson BS. Normal development of brain circuits. Neuropsychopharmacology : official publication of the American College of Neuropsychopharmacology 2010;35:147-168.

166. Raznahan A, Lerch JP, Lee N, et al. Patterns of Coordinated Anatomical Change in Human Cortical Development: A Longitudinal Neuroimaging Study of Maturational Coupling. Neuron 2011;72:873-884.

167. Duan K-B, Keerthi SS. Which Is the Best Multiclass SVM Method? An Empirical Study. In: Oza N, Polikar R, Kittler J, Roli F, eds. Multiple Classifier Systems: Springer Berlin Heidelberg, 2005: 278-285.

168. Lawson JA, Cook MJ, Vogrin S, et al. Clinical, EEG, and quantitative MRI differences in pediatric frontal and temporal lobe epilepsy. Neurology 2002;58:723-729.

169. Marin O, Rubenstein JL. Cell migration in the forebrain. Annual review of neuroscience 2003;26:441-483.

170. Nadarajah B, Parnavelas JG. Modes of neuronal migration in the developing cerebral cortex. Nature reviews Neuroscience 2002;3:423-432.

171. Duncan JS, Koepp MJ. PET: central benzodiazepine neuroreceptor mapping in localization-related epilepsies. Advances in Neurology 2000;83:131-136.

172. Bernhardt BC, Hong SJ, Bernasconi A, Bernasconi N. Magnetic Resonance Imaging Pattern Learning in Temporal Lobe Epilepsy: Classification and Prognostics. Annals of neurology 2015;77:436-446.

173. Tassi L, Garbelli R, Colombo N, et al. Electroclinical, MRI and surgical outcomes in 100 epileptic patients with type II FCD. Epileptic disorders : international epilepsy journal with videotape 2012;14:257-266.

174. Lawson JA, Birchansky S, Pacheco E, et al. Distinct clinicopathologic subtypes of cortical dysplasia of Taylor. Neurology 2005;64:55-61.

175. Gross RE, Mahmoudi B, Riley JP. Less is more: novel less-invasive surgical techniques for mesial temporal lobe epilepsy that minimize cognitive impairment. Curr Opin Neurol 2015;28:182-191.

176. Wong M. Mechanisms of epileptogenesis in tuberous sclerosis complex and related malformations of cortical development with abnormal glioneuronal proliferation. Epilepsia 2008;49:8-21.

177. Engel J, Jr. A proposed diagnostic scheme for people with epileptic seizures and with epilepsy: report of the ILAE Task Force on Classification and Terminology. Epilepsia 2001;42:796-803.

178. Kim H, Caldairou B, Hwang JW, et al. Accurate cortical tissue classification on MRI by modeling cortical folding patterns. Human brain mapping 2015;36:3563-3574.

179. Power JD, Barnes KA, Snyder AZ, Schlaggar BL, Petersen SE. Spurious but systematic correlations in functional connectivity MRI networks arise from subject motion. NeuroImage 2012;59:2142-2154.

180. Greve DN, Fischl B. Accurate and robust brain image alignment using boundary-based registration. NeuroImage 2009;48:63-72.

181. Polimeni JR, Fischl B, Greve DN, Wald LL. Laminar analysis of 7 T BOLD using an imposed spatial activation pattern in human V1. NeuroImage 2010;52:1334-1346.

182. Engelhardt E, Inder TE, Alexopoulos D, et al. Regional impairments of cortical folding in premature infants. Annals of neurology 2015;77:154-162.

183. Im K, Lee JM, Lyttelton O, Kim SH, Evans AC, Kim SI. Brain size and cortical structure in the adult human brain. Cereb Cortex 2008;18:2181-2191.

184. Hong SJ, Kim H, Schrader D, Bernasconi N, Bernhardt BC, Bernasconi A. Automated detection of cortical dysplasia type II in MRI-negative epilepsy. Neurology 2014;83:48-55.

185. Shafee R, Buckner RL, Fischl B. Gray matter myelination of 1555 human brains using partial volume corrected MRI images. NeuroImage 2015;105:473-485.

186. Beaulieu C. The basis of anisotropic water diffusion in the nervous system - a technical review. NMR in biomedicine 2002;15:435-455.

187. Zhang ZQ, Lu GM, Zhong YA, et al. FMRI Study of Mesial Temporal Lobe Epilepsy Using Amplitude of Low-Frequency Fluctuation Analysis. Human brain mapping 2010;31:1851-1861.

188. Zang Y, Jiang T, Lu Y, He Y, Tian L. Regional homogeneity approach to fMRI data analysis. NeuroImage 2004;22:394-400.

189. Dijkstra EW. A note on two problems in connexion with graphs. Numer Math 1959;1:269-271.

190. Studholme C, Cardenas V, Maudsley A, Weiner M. An intensity consistent filtering approach to the analysis of deformation tensor derived maps of brain shape. NeuroImage 2003;19:1638-1649.

191. Alexander AL, Lee JE, Lazar M, Field AS. Diffusion tensor imaging of the brain. Neurotherapeutics : the journal of the American Society for Experimental NeuroTherapeutics 2007;4:316-329.

192. Adams JG, Melhem ER. Clinical usefulness of T2-weighted fluid-attenuated inversion recovery MR imaging of the CNS. Am J Roentgenol 1999;172:529-536.

193. Tutz G. Regression for Categorical Data: Cambridge University Press, 2011.

194. Benjamini Y, Hochberg Y. Controlling the false discovery rate: a practical and powerful approach to multiple testing. Journal of the Royal Statistical Society Series B (Methodological) 1995:289-300.

195. Duda RO, Hart PE, Stork DG. Pattern classification: Wiley, 2001.

196. Rossini L, Medici V, Tassi L, et al. Layer-specific gene expression in epileptogenic type II focal cortical dysplasia: normal-looking neurons reveal the presence of a hidden laminar organization. Acta neuropathologica communications 2014;2:45.

197. Zucca I, Milesi G, Medici V, et al. Type II FCD: ex vivo 7 Tesla MRI abnormalities and histopathological comparisons. Annals of neurology 2015.

198. Fauser S, Haussler U, Donkels C, et al. Disorganization of neocortical lamination in focal cortical dysplasia is brain-region dependent: evidence from layer-specific marker expression. Acta neuropathologica communications 2013;1:47.

199. Zeng H, Pizarro R, Nair VA, La C, Prabhakaran V. Alterations in regional homogeneity of resting-state brain activity in mesial temporal lobe epilepsy. Epilepsia 2013;54:658-666.

200. Buccoliero AM, Barba C, Giordano F, et al. Expression of glutamine synthetase in balloon cells: a basis of their antiepileptic role? Clinical neuropathology 2015;34:83-88.

201. Boonyapisit K, Najm I, Klem G, et al. Epileptogenicity of focal malformations due to abnormal cortical development: Direct electrocorticographic histopathologic correlations. Epilepsia 2003;44:69-76.

202. Svolos P, Tsolaki E, Kapsalaki E, et al. Investigating brain tumor differentiation with diffusion and perfusion metrics at 3T MRI using pattern recognition techniques. Magnetic resonance imaging 2013;31:1567-1577.

203. Nakashima M, Saitsu H, Takei N, et al. Somatic Mutations in the MTOR gene cause focal cortical dysplasia type IIb. Annals of neurology 2015;78:375-386.

204. Sahin M, Sur M. Genes, circuits, and precision therapies for autism and related neurodevelopmental disorders. Science 2015;350.

205. Casanova MF, El-Baz AS, Kamat SS, et al. Focal cortical dysplasias in autism spectrum disorders. Acta neuropathologica communications 2013;1:67.

206. Pardoe HR, Mandelstam SA, Hiess RK, et al. Quantitative assessment of corpus callosum morphology in periventricular nodular heterotopia. Epilepsy research 2015;109:40-47.

207. Wagner J, Weber B, Urbach H, Elger CE, Huppertz HJ. Morphometric MRI analysis improves detection of focal cortical dysplasia type II. Brain : a journal of neurology 2011;134:2844-2854.

208. Hong S, Bernhardt B, Schrader D, Bernasconi N, and Bernasconi A. Whole-brain MRI phenotyping in dysplasia-related frontal lobe epilepsy. Neurology 2016.

209. Sisodiya SM. Wiring, dysmorphogenesis and epilepsy: a hypothesis. Seizure : the journal of the British Epilepsy Association 1995;4:169-185.

210. Goldman-Rakic PS. Morphological consequences of prenatal injury to the primate brain. Progress in brain research 1980;53:3-19.

211. Mechelli A, Friston KJ, Frackowiak RS, Price CJ. Structural covariance in the human cortex. The Journal of neuroscience : the official journal of the Society for Neuroscience 2005;25:8303-8310.

212. Miller JA, Ding SL, Sunkin SM, et al. Transcriptional landscape of the prenatal human brain. Nature 2014;508:199-206.

213. Honey CJ, Kotter R, Breakspear M, Sporns O. Network structure of cerebral cortex shapes functional connectivity on multiple time scales. Proceedings of the National Academy of Sciences of the United States of America 2007;104:10240-10245.

214. Bassett DS, Bullmore E. Small-world brain networks. Neuroscientist 2006;12:512-523.

215. van den Heuvel MP, Sporns O. Rich-club organization of the human connectome. The Journal of neuroscience : the official journal of the Society for Neuroscience 2011;31:15775-15786.

216. Holmes CJ, Hoge R, Collins L, Woods R, Toga AW, Evans AC. Enhancement of MR images using registration for signal averaging. Journal of computer assisted tomography 1998;22:324-333.

217. Rubinov M, Sporns O. Complex network measures of brain connectivity: uses and interpretations. NeuroImage 2010;52:1059-1069.

218. van den Heuvel MP, Kahn RS, Goni J, Sporns O. High-cost, high-capacity backbone for global brain communication. Proceedings of the National Academy of Sciences of the United States of America 2012;109:11372-11377.

219. Ray S, Miller M, Karalunas S, et al. Structural and functional connectivity of the human brain in autism spectrum disorders and attention-deficit/hyperactivity disorder: A rich club-organization study. Human brain mapping 2014;35:6032-6048.

220. Watts DJ, Strogatz SH. Collective dynamics of 'small-world' networks. Nature 1998;393:440-442.

221. Latora V, Marchiori M. Efficient behavior of small-world networks. Physical review letters 2001;87:198701.

222. Sporns O, Zwi JD. The small world of the cerebral cortex. Neuroinformatics 2004;2:145-162.

223. Bernhardt BC, Chen Z, He Y, Evans AC, Bernasconi N. Graph-Theoretical Analysis Reveals Disrupted Small-World Organization of Cortical Thickness Correlation Networks in Temporal Lobe Epilepsy. Cerebral Cortex 2011;21:2147-2157.

224. Bernhardt BC, Bernasconi N, Hong S-J, Dery S, Bernasconi A. Subregional Mesiotemporal Network Topology Is Altered in Temporal Lobe Epilepsy. Cerebral Cortex 2015.

225. Courchesne E, Pierce K. Why the frontal cortex in autism might be talking only to itself: local over-connectivity but long-distance disconnection. Curr Opin Neurobiol 2005;15:225-230.

226. Stephan KE, Friston KJ, Frith CD. Dysconnection in schizophrenia: from abnormal synaptic plasticity to failures of self-monitoring. Schizophr Bull 2009;35:509-527.

227. Castellanos FX, Margulies DS, Kelly C, et al. Cingulate-precuneus interactions: A new locus of dysfunction in adult attention-deficit/hyperactivity disorder. Biol Psychiat 2008;63:332-337.

228. Bernhardt BC, Bonilha L, Gross DW. Network analysis for a network disorder: The emerging role of graph theory in the study of epilepsy. Epilepsy & behavior : E&B 2015;50:162-170.

229. Stam CJ. Modern network science of neurological disorders. Nat Rev Neurosci 2014;15:683-695.

230. Huang H, Xue R, Zhang J, et al. Anatomical characterization of human fetal brain development with diffusion tensor magnetic resonance imaging. The Journal of neuroscience : the official journal of the Society for Neuroscience 2009;29:4263-4273.

231. Takahashi E, Folkerth RD, Galaburda AM, Grant PE. Emerging cerebral connectivity in the human fetal brain: an MR tractography study. Cereb Cortex 2012;22:455-464.

232. Kirschner M, Gerhart J. Evolvability. Proceedings of the National Academy of Sciences of the United States of America 1998;95:8420-8427.

233. Bassett DS, Wymbs NF, Porter MA, Mucha PJ, Carlson JM, Grafton ST. Dynamic reconfiguration of human brain networks during learning. Proceedings of the National Academy of Sciences of the United States of America 2011;108:7641-7646.

234. Sporns O, Betzel RF. Modular Brain Networks. Annu Rev Psychol 2016;67:613-640.

235. Plitt M, Barnes KA, Wallace GL, Kenworthy L, Martin A. Resting-state functional connectivity predicts longitudinal change in autistic traits and adaptive functioning in autism. Proceedings of the National Academy of Sciences of the United States of America 2015;112:E6699-6706.

236. Casanova EL, Casanova MF. Genetics studies indicate that neural induction and early neuronal maturation are disturbed in autism. Frontiers in Cellular Neuroscience 2014;8.

237. Lewis DA, Levitt P. Schizophrenia as a disorder of neurodevelopment. Annual review of neuroscience 2002;25:409-432.